THEORY OF DIFFRACTION AND ELECTRON MICROSCOPY OF MEDIUM RANGE ORDER IN AMORPHOUS METALS

Tadashi HAMADA

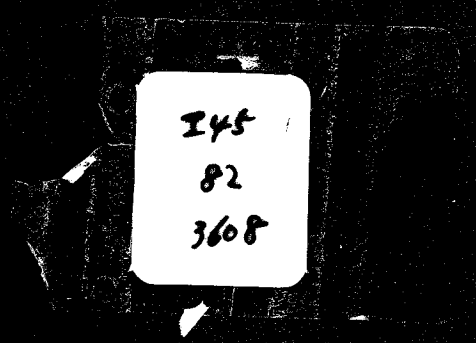

OSAKA UNIVERSITY
GRADUATE SCHOOL OF ENGINEERING SCIENCE
DEPARTMENT OF MATERIAL PHYSICS
TOYONAKA OSAKA

THEORY OF DIFFRACTION AND ELECTRON MICROSCOPY OF MEDIUM RANGE ORDER IN AMORPHOUS METALS

Tadashi HAMADA

Osaka Prefectural Industrial
Research Institute

January 1985

SYNOPSIS

Taking account of experimental evidences of the chemical short range order and the medium range order in the amorphous structures, the crystalline embryo model is proposed by employing the concept of quasi-crystalline clusters which could pre-exist in the liquid state, be enhanced during supercooling and be frozen as the static crystalline embryos by the rapid quenching. A simple model assembly of single element atoms containing the b.c.c. or f.c.c. embryos is first constructed by computer, and the calculated diffraction functions semiquantitatively explained the characteristic halo intensity distribution of the amorphous metals. As a more realistic structural model containing metalloid atoms, the composite type embryo models for amorphous Fe-B alloys are constructed by assuming the b.c.c. embryos and chemical clusters of Fe_3B type coexisting in it. The diffraction functions and the high resolution electron microscope images calculated from such embryo models well reproduce the experimental results, when the embryo size is taken to be as small as 10 A in diameter, and quantitative discussions on the truncation effect in the Fourier transformation for the diffraction functions and the effect of aberrations and defocusing on the high resolution image formation are successfully done. It is concluded that the medium range order clusters of this size most probably exist in the real amorphous metals. Comparing with other structural models, the consistency and the validity of the present theory and calculations are also concluded.

Contents

1. INTRODUCTION

1.1. General Introduction

The theory of x-ray diffraction and high resolution electron microscopy of the medium range order in amorphous metals and alloys will be described in this thesis. The origin of the medium range order will also be discussed in relation with thermodynamical and structural considerations.

Amorphous solids have always been found to be, at best, metastable with respect to some crystalline phase or phase mixture. The liquid of many metals and alloys can be made into a metastable amorphous solids if it can be cooled by sufficiently fast quenching such as in the vapour condensation, the electrodeposition, the chemical deposition and the rapid cooling from the melt. It is convenient to distinguish three categories of amorphous metals and alloys; amorphous elemental metals, metal-metal alloys and alloys of transition metals with non-metallic elements, i.e. metalloids. The thermal stability of these materials increases with the difference in chemical bonding nature between constituent atoms. The amorphous elemental metals are formed only as evaporated or sputtered thin films and generally crystallize at temperatures about one tenth of the melting temperature, T_m. By contrast, the amorphous metal-metalloid alloys, for example Pd-Si and Fe-B alloys, can be obtained as continuous strips by the quenching from the melt at the cooling rates of $10^{5\sim6}$ K/s and are stable to temperatures of the order of $0.4T_m$. In this thesis, the discussion will be mainly concentrated on the amorphous alloys of the metal-metalloid

systems. Since the first production of an amorphous Au-Si alloy by the rapid quenching from the melt,[1)] various amorphous metals and alloys have been found to exhibit technologically interesting properties, e.g. the high fracture strength, the excellent soft magnetic behaviour and the good corrosion resistance, and at the same time they have been offered to the investigators in the basic research field for the studies of the structure, the atomic transport, the electronic and magnetic properties and the thermodynamic characterization of disordered metallic systems. However, the fundamental problems on the atomic structure of the disordered systems still remain unsolved in spite of a large number of efforts made by many investigators during past a few decades. Especially, the basic understanding of the amorphous structure inherited from the liquid or other parent states seems to be one of the most important and fascinating subjects for the liquid and solid state physicists.

Recently, a number of techniques, like the x-ray and neutron diffraction, the Mössbauer spectroscopy, the high resolution electron microscopy and the computer model calculation, have been developed to considerable extents and applied to the basic study of the amorphous structure. The most direct characterization of the random atomic arrangements is given by the x-ray, neutron and electron scattering experiments. The coherently scattered intensity distribution, i.e. the interference function, of the amorphous metals and alloys exhibits the apparently characteristic diffuse one. The pair correlation function obtained from the Fourier transformation of the interference function yields only a statistically

averaged projection of the amorphous structure onto one dimension and does not always establish a unique description of the atomic configuration in real three dimensional coordinates. Nevertheless, it has been found that the pair correlation function of the amorphous structure does not only exhibit the oscillation of amplitude over larger radial distances, but also shows a sharp well defined first maximum and the peculiar second peak splitting, as compared with that of the liquid structure. This means that the amorphous metals and alloys may have a degree of order in the atomic arrangements higher than that in the molten state. In fact, many newer experimental results, including not only those by diffraction techniques but also those by other tehcniques as above mentioned, have strongly suggested that the chemical short range order or even farther range atomic order extending beyond the first neighbour distance exists in the actual amorphous structure.

On the other hand, the modelling experiment seems to be a powerful and available means since it can give us an intuitive picture on the nature of disorder of the amorphous metals and alloys. Since Bernal's first proposal of the concept of dense random packing (DRP) of atoms,[2] the idea of DRP has suffered various examinations and improvements and this sort of studies has been prevailing in the field of the study of the amorphous structure. However, the high degree of ordering in the actual amorphous structure is hardly expected from the DRP models. The existence of the chemical short range order in the amorphous alloys is widely accepted from the fact that the atomic arrangement of nearest neighbours in a restricted range of the metalloid atom composition is similar to that

found in one crystalline form of the material. In accordance with this, the chemical cluster model has been proposed, where the chemical clusters typical of the structure of crystal phases appearing during the devitrification of amorphous alloys are packed randomly to form a dense and three dimensional array. However, with respect to the medium range order, there remain a great deal of arguments and problems to be solved. One of the most important problems is about the origin of such atomic orderings including the chemical one and another is its effects on the x-ray diffraction and the electron images. It must be noted that experimentally the diffraction pattern is kept almost unchanged and shows the diffuse intensity distribution characteristic of the amorphous structure, even if the quenching rate is critically changed, by which the size and the amount of the chemical short range or medium range order are expected to largely depend on. Accordingly, the systematic and theoretical consideration on the chemical short range and medium range order is indispensable for the satisfactory description of the amorphous structure.

Taking such high degree of atomic orderings into consideration, Hamada and Fujita[3] have proposed the crystalline embryo model for the structure of amorphous metals and alloys. As will be presented and discussed in this thesis, the crystalline embryo model is based on the concept of quasi-crystalline clusters, which is expected to pre-exist in the liquid structure including the supercooled state and be quenched in the amorphous structure by the rapid cooling. This model is quite different from the microcrystalline model in the sense that the crystalline embryos exist

surrounded by the disordered region in the amorphous structure. In reality, the embryo model satisfactorily reproduces the diffraction data and the high resolution electron images from the medium range order in the disordered structure, which is considered to offer the bases necessary for the interpretations of the experimental results and yet to present the solutions for above mentioned problems. In the following sections of the chapter 1 are mentioned, in the first place, the experimental evidences of the structural orderings in the amorphous metals and alloys given by the neutron and x-ray diffraction, the Mössbauer spectroscopy, the HREM and the magnetic measurements etc. In the second, the various models for the amorphous structures are introduced. The origin of the structural orderings in the amorphous metals and alloys and the uselessness of the application of the micro-crystalline diffraction theory to them will be considered, and the model construction based on the concept of crystalline embryos will be described in the chapter 2, which will be then followed by the calculated results of the interference and pair correlation functions and the high resolution electron images in the chapter 3 and 4 respectively. Finally, in the chapter 5, the differences among various structural models so far proposed, the comparison of the embryo model with the experimental results and the probability of existence of the medium range order will be rigidly discussed. The consistency and validity of the present theory and calculation will be concluded and acknowledgements will be given in the last.

1.2 Experimental Evidences of Structural Ordering in Amorphous Metals and Alloys

There have been a great many of experimental studies on the structure of amorphous metals and alloys which were reviewed in literatures[4] and articles.[5,6] Amorphous metals and alloys are considered as solids with a frozen-in liquid structure and are macroscopically isotropic in the domain range greater than 20 A. In addition to this, the three dimensional atomic periodicity is almost lost beyond a few atomic distances, although the degree of order in the atomic arrangements is higher than that in the molten state. It is characterized by a limitted number of diffuse halos in the x-ray, neutron and electron diffraction and no sharp diffraction contrasts in the electron microscopy. Recently, a number of techniques, the x-ray and neutron diffraction, the Mössbauer spectroscopy, the NMR, the high resolution electron microscopy, etc., have been extensively developed and applied to the study of the amorphous structure. Some newer experimental results obtained by these techniques strongly suggest that the chemical short range order or even farther range atomic order extending beyond the first neighbour distance may exist in the actual amorphous structures. In this section, the evidences of such structural orderings in the amorphous metals and alloys are given for each experimental technique.

1.2.1 Neutron and x-ray diffraction

The neutron and x-ray diffraction methods have been frequently used to analyse the structure of amorphous materials. The radial

distribution function or the pair correlation function G(r) is obtained by the Fourier transformation of the coherently scattered intensity distribution or the interference function S(K). The G(r) function provides only a statistical average projection of the structure onto one dimension. So that, the three dimensional arrangements of atoms in the amorphous solids can not be uniquely determined from the G(r). It is worthy of note that the S(K) function and the G(r) function for any of the amorphous metals and alloys have quite similar appearances, although they are related with each other by Fourier transformation. In Fig.1 are illustrated the S(K) and G(r) functions of an amorphous iron film,[7] which was made by the vapour condensation method on the cold substrate kept at liquid helium temperature, and for comparison those of the liquid iron.[8] The oscillations in both functions have larger amplitudes and persistently remain in higher K or r values for the amorphous iron than for the liquid iron. Furthermore, two functions of the amorphous iron have a characteristic sharp fist peak and a broad second peak splitting into two subpeaks. These profiles vary with the composition, the preparation technique and the heat treatment as are described below.

Experimental information on the local coordination of metalloid atoms in the amorphous alloys is meagre. The x-ray and neutron scattering are generally dominated by the contributions from the heavier metallic elements. Since the concentration of the non-metallic element is about 20at%, the weighing factor w_{N-M} is typically three times smaller than the corresponding factor for M-M correlations, where M denotes metals and N non-metals. Moreover,

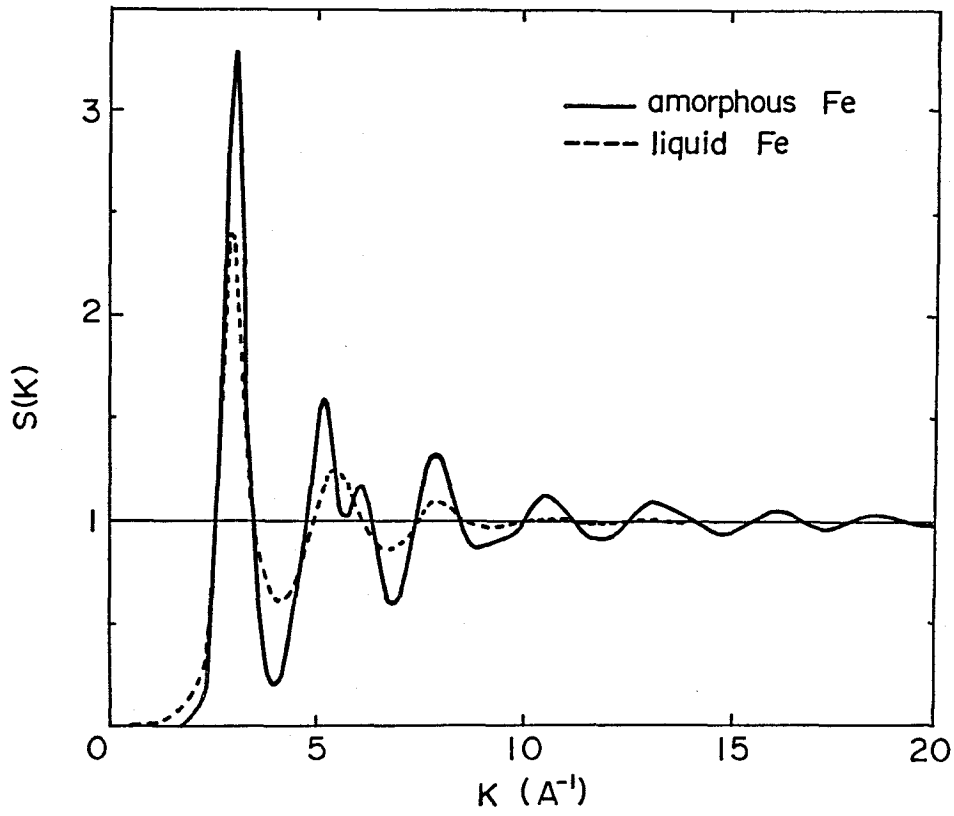

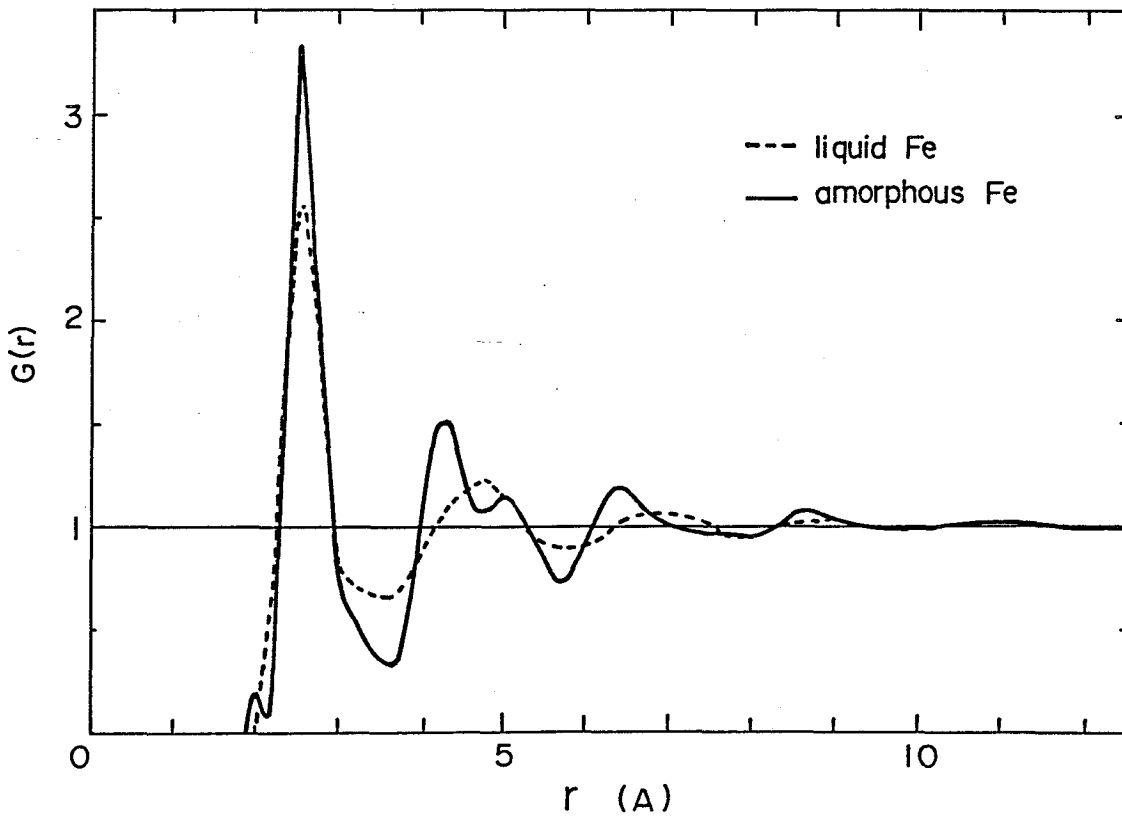

Fig. 1 The interference functions, S(K)'s, and the pair correlation functions, G(r)'s, of amorphous Fe given by Ichikawa and liquid Fe at 1560°C given by Waseda and Ohtani.

the radius ratio r_N/r_M (where r being the effective atomic radius) generally lies in the range 0.75∿0.85 so that the peak of the N-M pair correlation function is found at a distance of about $1.8r_M$ and, accordingly, difficult to be resolved from the M-M distance as a separate component. Especially in the x-ray measurements, the diffraction data in the reciprocal space are confined to the K values below about 17 A^{-1} and good resolution of the G(r) is not obtainable.

Dixmier and Duwez[9] reported a slight asymmetry in the first peak of the G(r) in the amorphous Pd-Ni-P alloys and attributed it to a contribution from metal-metalloid pairs. Suzuki et al.[10] showed that the resolution of the G(r) was progressively improved when the truncation was made at higher K_{max} values in the Fourier transformation of the S(K), which is shown in Fig.2. The scattering from several amorphous Pd-Si alloys was also measured by Fukunaga et al.[11] over a wide range of K values from 0.5 A^{-1} up to 30 A^{-1} by means of the time-of-flight neutron technique, and well resolved pair correlation functions showing a distinct separation between two first neighbour peaks at 2.42 A and 2.81 A, which are associated with Pd-Si and Pd-Pd distances respectively, were obtained. From the area under the peak at the smaller radial distance 2.42 A, the average number of nearest neighbour Pd atoms surrounding each silicon atom was estimated. They concluded that a Si atom is predominantly surrounded by six Pd atoms forming a trigonal prism which is very close to that found in the crystalline compound Pd_3Si. In the liquid alloy with the same concentration, the G(r) function shows a shallow hump instead of the distinct sub-

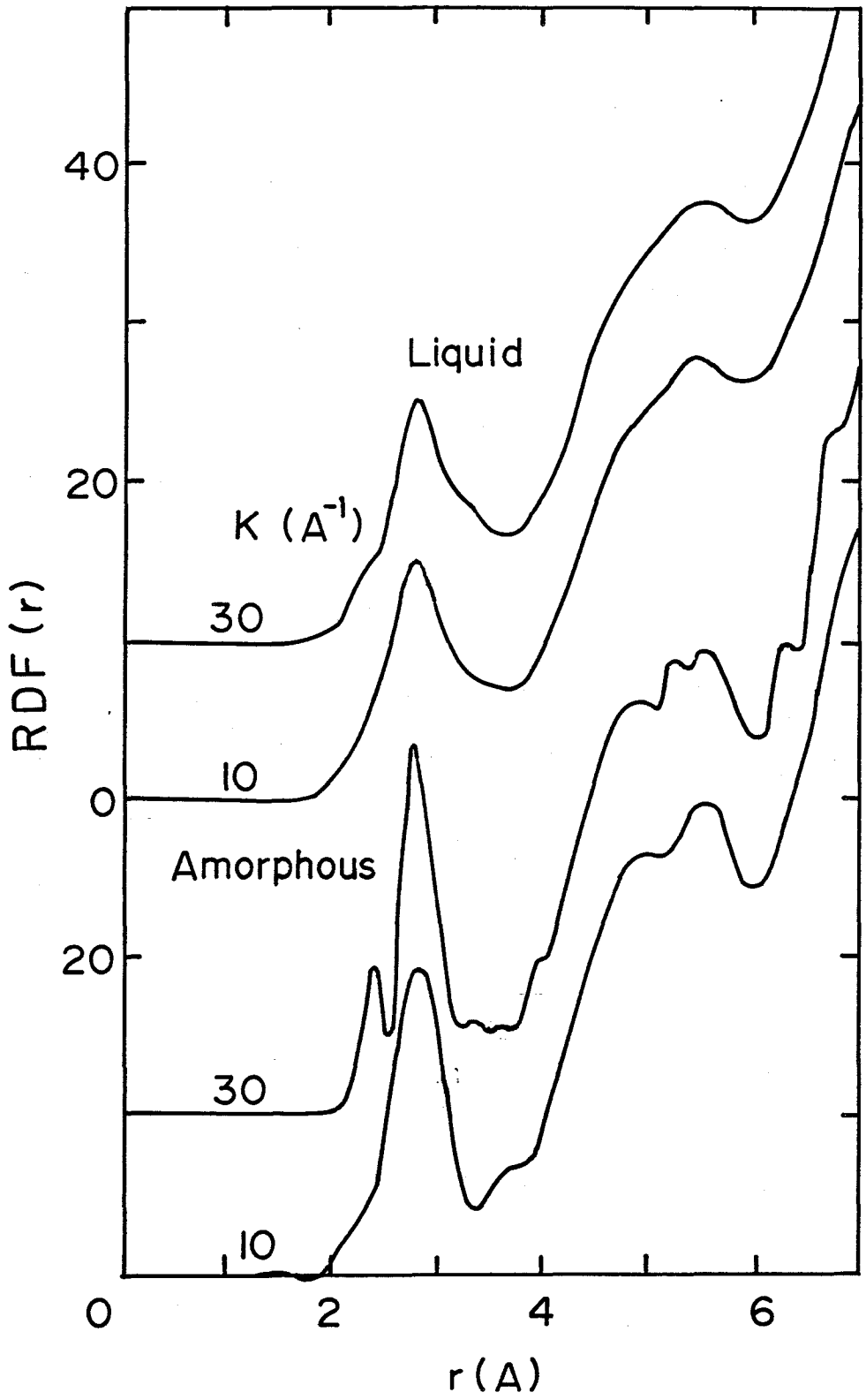

Fig. 2 The radial distribution functions, RDF(r)'s, of amorphous $Pd_{80}Si_{20}$ alloy and liquid $Pd_{80}Si_{20}$ alloy at 980°C given by Suzuki et al. K_{max} means the magnitude of maximum scattering vector where the Fourier transformation from S(K) to G(r) is truncated.

peak at 2.42 A, which might suggest the existence of the chemical short range order in the liquid structure. Noteworthy is that a small tail extends toward the lower radial distance, ∿2.2 A, most likely arising from Si-Si neighbouring, and that it is absent in the amorphous alloy. This fact suggests that the possibility of a random mixture of Pd and Si atoms in the amorphous structure is eliminated as found in the intermetallic crystalline structures, Pd_3Si and Pd_2Si.

The most reliable information on the local coordination of the non-metallic atom was obtained by Sadoc and Dixmier[12] by recording three independent sets of scattering data, using a combination of the x-ray and the polarized and unpolarized neutron diffraction from the amorphous $Co_{81}P_{19}$ alloy. These were analysed to give the three separate pair correlation functions, which clearly showed phosphorous and cobalt atoms occupying sites with different symmetry and geometry. They concluded that surroundings of P atoms are similar to those found in the crystalline Ni_3P (the structure of Co_3P has not been reported) and the nearest neighbour P-P correlations are absent. Lamperter et al.[16] obtained the total and partial structure factors of an $Fe_{80}B_{20}$ amorphous alloy by the x-ray diffraction and the neutron diffraction using the isotopic substitution method. The partial G(r) function for the Fe-B correlation showed a very sharp and high first maximum and that for the B-B correlation indicated the absence of the close contact of B atoms. They also concluded that the short range order in the amorphous $Fe_{80}B_{20}$ alloy is strongly governed by the chemical bonding between unlike atoms. The variation of the x-ray atomic scattering

factors with the wavelength in the region of an absorption band has also been used to obtain the partial pair correlation functions for the amorphous $Ni_{80}P_{20}$,[13] $Fe_{82.5}P_{17.5}$,[14] and $Fe_{75}B_{25}$[15] alloys. These experiments showed that the environment of metalloid atoms is very similar to the findings by Sadoc and Dixmier and Lamperter et al. However, the resolution of real-space data is poor as a result of termination ripples and broadening, since scattering data are restricted to small scattering angles ($K_{max} \simeq 7 \sim 10$ A^{-1}).

The influence of metalloid concentration on the structure was investigated for the amorphous (Pd, Ni)-P,[9] Ni-P,[17] Co-P,[18] Fe-P,[19] Pd-Ge,[20] Pd-Si[11] and Fe-B[11,21] alloys. Over the metalloid compositions ranging from 15 at% to 25 at%, the intensity and the position of each peak in the S(K) and G(r) functions undergo various changes. For instance, the height of the first peak in the G(r) function is gradually decreased with increasing the metalloid concentration. For the phosphorous atoms containing alloys, although the first subpeak at r_2 of the second peak in the G(r) is always more intense than the second one at the larger radial distance, r_2', the intensity ratio, Ir_2'/Ir_2, is decreased with increasing metalloid content as well as the corresponding intensity ratio in the S(K) function. From the seemingly similar x-ray diffraction measurements of the amorphous Fe-B alloys with various boron contents, Fukunaga et al.[11] and Waseda and Chen[21] obtained quite different conclusions on the appearance of the S(K) and G(r) functions. Two diffraction functions obtained by the former are shown in Fig.3 (a) and (b) respectively. The intensity of the high angle side shoulder on the second halo peak in the S(K) was shown

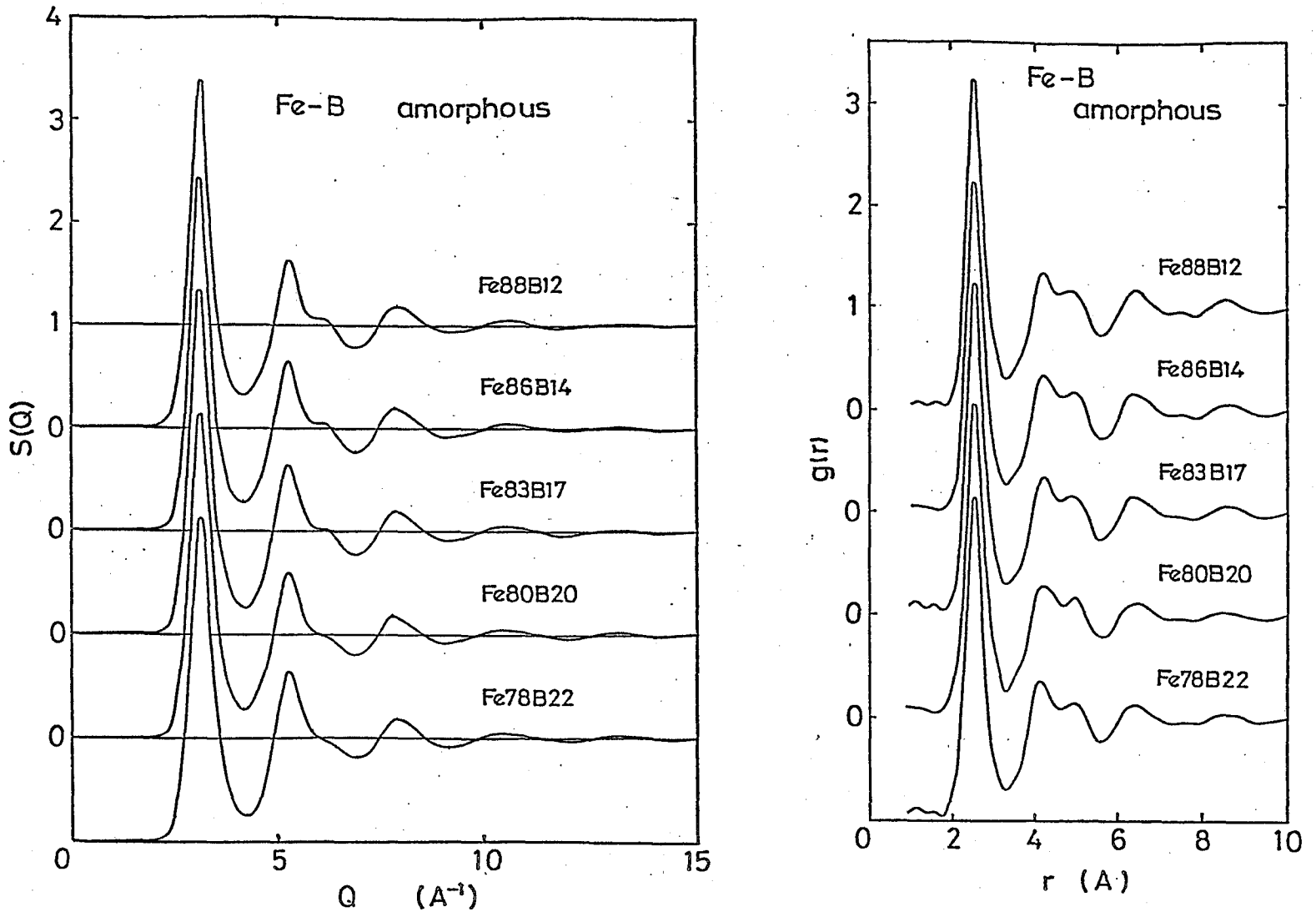

Fig. 3 The diffraction functions of amorphous Fe-B alloys given by Fukunaga et al.: (a) the S(K) functions, and (b) the G(r) functions.

to increase in the result by the latter, but in that by the former it decreased with increasing boron content, as given in (a) of the figure 3. These disagreements in the S(K) functions were also reflected in the G(r)'s. For most of the metal-metalloid amorphous alloys, the G(r) has the characteristic second peak splitting, of which the first subpeak at the smaller radial distance, r_2, is more intense than the second one at r_2' as mentioned above. But, Waseda and Chen found that the peak height ratio of the second peak doublet in the G(r) was reversed for the amorphous Fe-B alloys with the boron content below 20 at%. On the contrary, according to Fukunaga et al., the G(r) functions of amorphous Fe-B alloys in the composition range 12∿22 at%B showed the "normal" second peak splitting and the decrease of the intensity of the second peak shoulder at r_2' with increasing boron content, which are given in Fig.3 (b), as well as those of the Fe-P and other metal-metalloid amorphous alloys. Neutron diffraction experiments undertaken on an $Fe_{83}B_{17}$ amorphous alloy by Cowlam et al.[22] and on an $Fe_{80}B_{20}$ amorphous one by Lamperter et al.[16] indicated that the second peak splitting in the G(r) was "normal", thus confirming the observation by Fukunaga et al. Dini et al.[23] made a comparison in detail between those two experiments on the structure of Fe-B alloys which were in disagreement. They suggested that the discrepancy in the S(K) curves could arise through structural differences in the samples relating to their history of quenching. However, it was not clear what sort of changes were produced by the enhanced annealing, i.e. the slow down of cooling rate at the later stage of quenching, and thereby the structural relaxation in the twin-

rolled samples. It must be also noted that well resolved pair correlation functions of the several amorphous Pd-Si alloys, one of which is shown in Fig.2, displayed a second peak splitting into three subpeaks. This fact strongly suggests that not only the chemical short range order as mentioned before but also the atomic order extending beyond the first neighbour distance may exist in the actual amorphous structure.

1.2.2. Mössbauer spectroscopy

Mössbauer spectroscopy is a useful technique to study the small structural units in the amorphous structure, because it can detect the electronic structures of a small group of atoms or even a single atom through the near neighbour interactions. Tsuei et al.[24] were the first to measure the ^{57}Fe Mössbauer spectrum of Fe-P-C amorphous alloy. They obtained a broad ferromagnetic six line pattern and analysed it with the assumption of disordered near-neighbour configurations of iron atoms and an unpreferred spin orientation distribution.

Fujita et al.[25] showed that in the ferromagnetic Fe-P-C amorphous alloys containing 20 at% of metalloids the internal field distribution was quite the same as those in the high concentration alloys. In solid solution alloys, the magnetic moment and, thereby, the internal field of a magnetic atom change (usually decrease) in proportion to the number of near neighbour foreign atoms. By assuming that the short range order in the amorphous structure is almost the same as in the crystalline solid solution, the above reduction rule of the environmental effect was applied to the analy-

sis of the internal field distribution in the amorphous Fe-P-C and Fe-B alloys with the metalloid concentration between 15 and 20 at% by Oshima and Fujita.[26] They concluded that in these amorphous alloys, the atomic order corresponding to the crystalline polyhedrons with the b.c.c.-like near-neighbour configuration is well developed in the as quenched state. It was also concluded that, by taking the reasonable calculated values of the internal field reduction by foreign atom neighbours into consideration, it is very difficult to detect the defective structures such as represented by Bernal's DRP polyhedrons.

Mössbauer spectroscopy has exhibited the development of another kind of ordering in the amorphous alloys in certain cases. The ferromagnetic Mössbauer pattern from the $Fe_{75}B_{25}$ alloy showed a deviation from the ordinary spectra such that the analysis according to the solid solution like short range order was not applicable. Vincze et al.[27] attributed this deviation to the chemical short range order structure, and concluded that the structures of the amorphous Fe-B alloys with various boron contents are based on a locally-distorted off-stoichiometric Fe_3B compound. Koshimura et al.[28] analysed the Mössbauer spectra of the amorphous $Fe_{83}B_{17}$ and $Fe_{82}P_{18}$ alloys and also concluded taht these alloys contain intermetallic compounds of Fe_3B and Fe_3P respectively. Oshima and Fujita,[26] however, concluded that the $Fe_{75}B_{25}$ amorphous alloy contains partly the Fe_3B chemical clusters and partly the solid solution type clusters, and the former disappears when the B concentration is reduced below 20 at%. It was also concluded that when the quenching rate is not fast enough, the Fe_3B chemical clusters sur-

vive in the amorphous alloys with boron less than 20 at%.

1.2.3 High resolution electron microscopy

In parallel with the investigations by diffraction theory and technique, the structure of amorphous materials has been studied over a decade by the high resolution electron microscopy (HREM), since it was expected to yield information of local atomic structure projected to two dimensions, which would be more direct and sometimes more detailed than the diffraction data such as the interference functions S(K) and the pair correlation function G(r), which are basically one dimensional in the case of the study of halo diffraction patterns. Especially, the high resolution electron microscopy was supposed to be powerful to provide the experimental evidences for the above mentioned structural order if it exists in the amorphous materials. In the very early stage of high resolution electron microscopy, the instrumental performance of electron microscopy for the lattice image observation was limited to the tilted beam setting and only the large scale spotty or fringy images were observed and interpreted in terms of the microcrystalline model.[29] A more careful work[30] showed, however, that the number and the orientations of the fringes depended on the angle of the tilt illumination, suggesting that they were mainly due to an instrumental effect. The fringy images of this kind do not occur in recent observations when the incident electron beam is aligned parallel to the instrument axis (optical axis) and the objective aperture is placed with the center coincident with the transmitted beam spot. Under this condition, however, some inves-

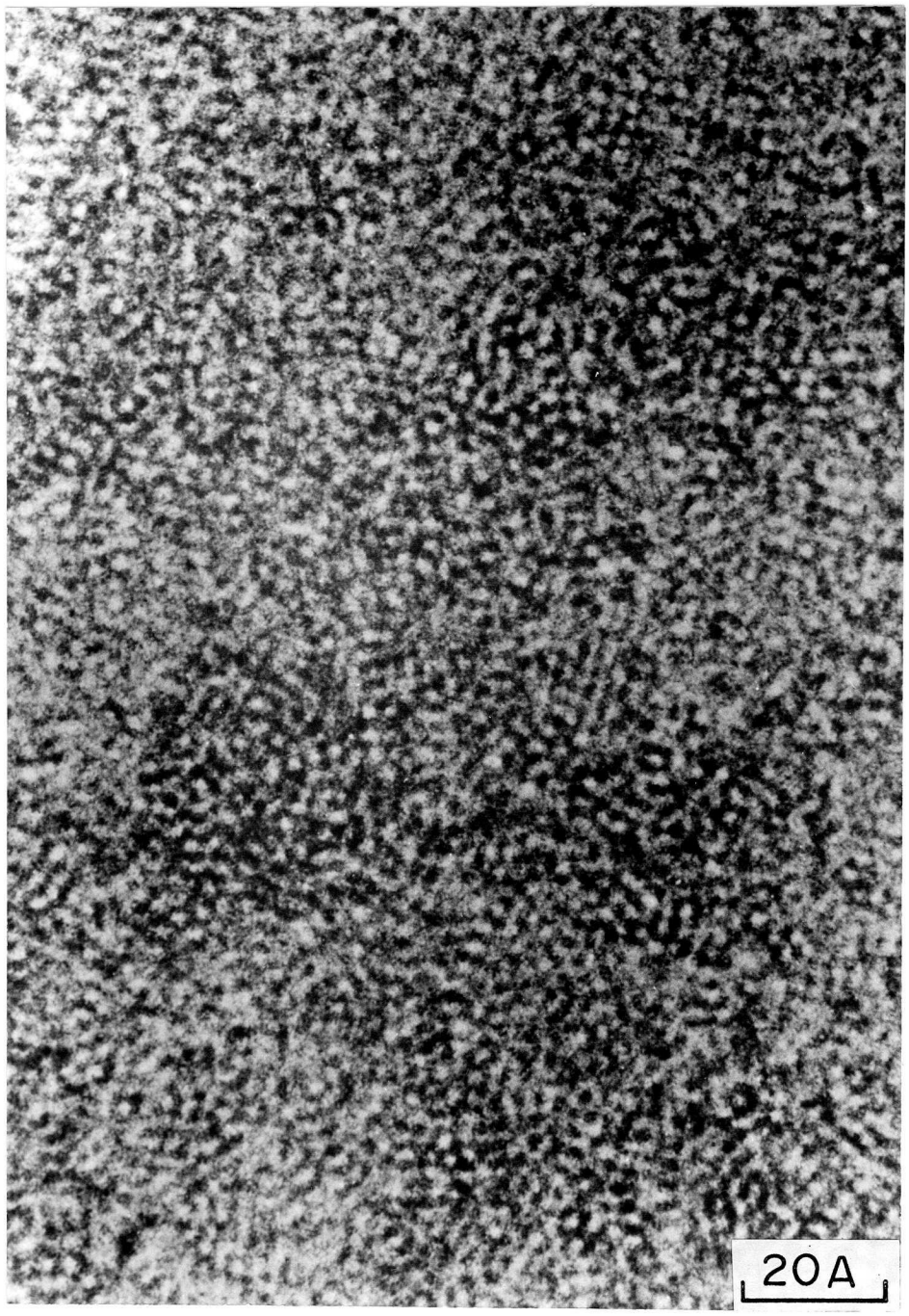

Fig. 4 The high resolution axial bright-field image from the as quenched thin specimen of amorphous Fe-B alloy. Courtesy by Ichinose and Ishida.

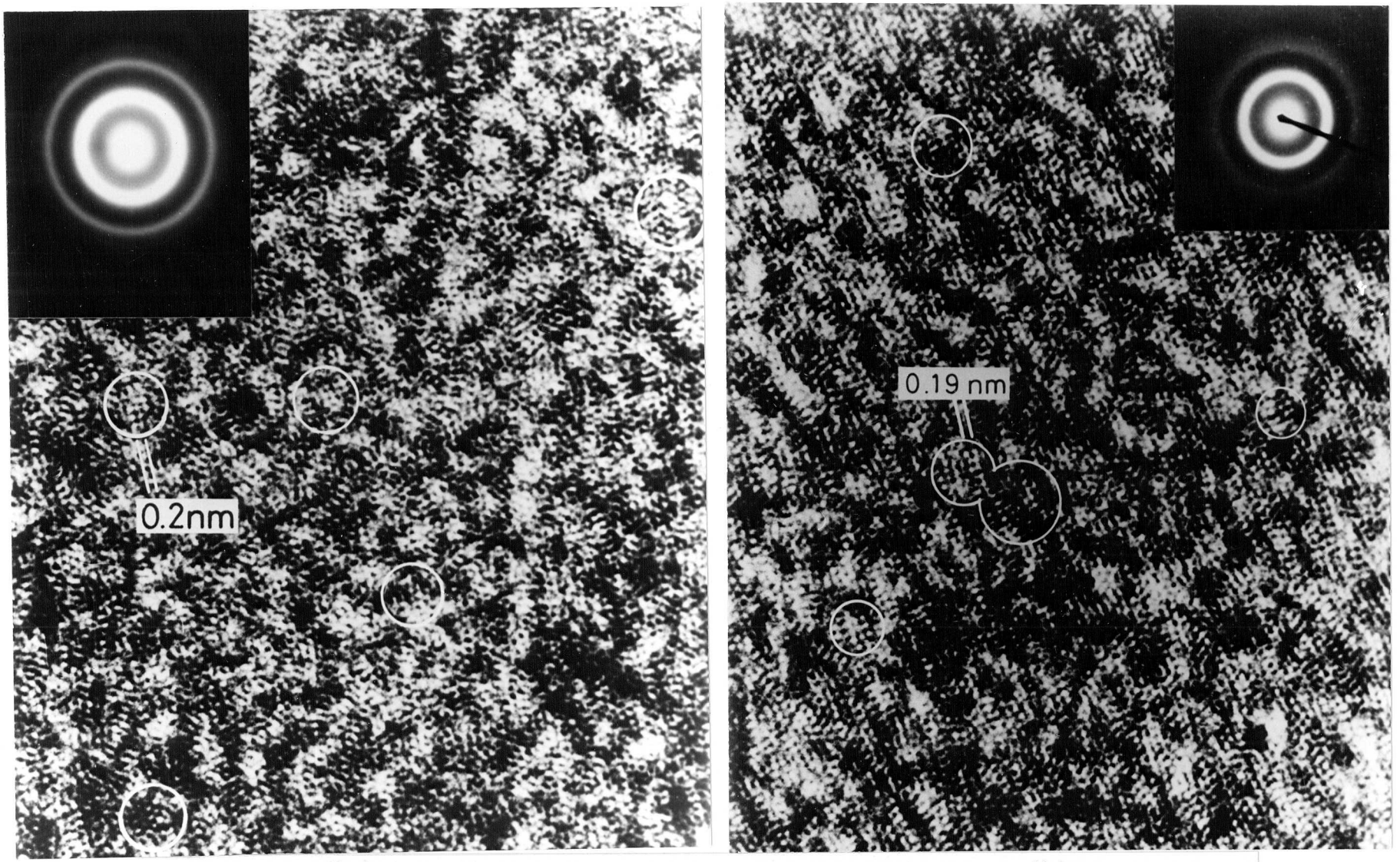

(a) (b)

Fig. 5 The high resolution axial bright-field images of as quenched thin films: (a) the amorphous $Fe_{84}B_{16}$ alloy with Δf=-1500 A, and (b) the amorphous $Pd_{77.5}Cu_6Si_{16.5}$ alloy with Δf=-1650 A. Encircled areas correspond to microcrystalline regions. The insets are halo electron diffraction patterns. Courtesy by Hirotsu and Akada.

tigators have observed lattice like fringes locally even in the as quenched amorphous metallic alloys. For instance, Ishida et al.[31] studied the structure of electolytically thinned films of the iron, cobalt and paradium based amorphous alloys through the bright-field HREM with the axial illumination and observed the lattice like images which varied largely with the alloy compositions, quenching method and quenching rate, even though the electron diffraction patterns were typical of amorphous structure. They concluded that the fringes arose from the microcrystalline regions of several ten angstroms in diameter. Ichinose and Ishida[32] carried out the observation of the high resolution axial bright-field images from the as quenched thin specimens of the amorphous iron based alloys, one of which is shown in Fig.4. Some lattice like image contrasts of about 10 A in diameter are seen in the micrograph. Hirotsu and Akada[33] did similar observations on the as quenched amorphous $Fe_{84}B_{16}$ and $Pd_{77.5}Cu_6Si_{16.5}$ alloys with the selected values of the defocus distance, which are shown in Fig.5 (a) and (b), respectively. The lattice and fringy images with an average size of 12 A are observed with a spacing of about 2 A and four or six-fold symmetry in (a) and with about 1.9 A spacing and four-fold symmetry in (b). They explained these images in terms of microcrystals with the beam incidences along <001> and <111> of the b.c.c. structure in (a) and with that along <100> of the f.c.c. one in (b).

1.2.4 Magnetic measurement and others

In the chemical clusters, which is expected to exist in the

amorphous alloys, metal atoms and non-metallic atoms have strong covalent bonding with each other. The chemical nature of the chemical compound cluster can be detected sometimes by measuring the physical and chemical properties of the amorphous alloys by using various techniques. Takahashi and Koshimura[34] measured the magnetization of the magnetic amorphous Fe-B, Co-B, Ni-B and Fe-P-C alloys against the temperature and from peculiar change of the magnetization curves they concluded that the chemical compound clusters large enough to exhibit their own magnetic behaviour already exist in the as quenched structure. Other results obtained from the magnetic measurements[35-37] seem to suggest that amorphous Fe-B alloys ranging from 12 at%B to 25 at%B have a concentration dependence of the structure.

Durand et al.[38] carried out the ^{59}Co NMR and bulk magnetic measurements with the aim to understand the various contributions to the Co hyperfine field in the liquid quenched amorphous Gd-Co alloys. From the complex structure appearing in the Co NMR spectra with varying the Co content, they concluded that the composition dependent crystalline compounds exist in the as quenched amorphous alloys.

Extended x-ray absorption fine structure (EXAFS) does not suffer from the limitation imposed by low scattering factors for the non-metallic atoms inherent in the x-ray scattering and offers the most sensitive technique for probing the local coordination around the metalloid atom. EXAFS measurements using the K-shell absorption of the Ge atoms in the amorphous Pd-Ge alloys was carried out by Hayes et al.[39] They showed that the average environment of

the Ge atoms consists of a spherical shell of nearest-neighbour Pd atoms with no nearest-neighbour Ge-Ge interactions.

1.3 Various Structural Models

The concept of dense random packing (DRP) proposed first by Bernal[2] has been widely accepted as a useful one to describe the structure of amorphous metals and alloys as regards the atomic disordering. Especially, in recent years, computer simulations have succeeded in reconstructing the "ideal" amorphous structure. The characteristics of computer-generated DRP models, such as the coordination number, density, interference function and pair correlation function, were found to be in tolerable agreement with the results of diffraction experiments. Critical reviews of the structural models have been given by Finney,[40] Waseda,[41] and Chaudhari and Turnbull.[42]

As mentioned in the last section, many recent experimental evidences strongly suggest that the atomic order and chemical short range order develop beyond the first neighbour distance in the actual amorphous structure, which is hardly expected from the DRP models. Taking account of the existence of such atomic ordering in the amorphous structure, Hamada and Fujita[3] have proposed the crystalline embryo model, which will be described and rigidly discussed in this thesis. For the amorphous alloys, the concentration of which is close to the stoichiometry, the chemical cluster model has been proposed. In this section, various structural models including not only above mentioned models but also the microcrystalline model and the dislocation model are introduced and discussed.

1.3.1 Dense random packing model

Since Bernal's first proposal of the concept of dense random

packing of atoms, which was in order to construct a static model of liquid structure, the idea of DRP has suffered various examinations and improvements. The Bernal's model was a favourable one as a model for the amorphous structure rather than for the liquid structure, because it could not reproduce satisfactorily the pair correlation function G(r) of liquid metals but could give the splitting of the second peak in the G(r) of amorphous metals and alloys. This model structure is represented by arrangements of rigid spheres which are dense in the sense that they contain no internal holes large enough to accommodate another sphere and are random in the sense that there are only weak correlations between positions of spheres separated by two or more sphere diameters and that they apparently contain no recognizable regions of crystal like order.

The dense random packing of single size hard spheres was established either by packing together as densely as possible a large number of steel balls or by computer algorithms. In the former case, the experiments by Finney[43] and Scott and Kilgour[44] consisted of squeezing and kneading rubber bladders filled with ball bearings, taking precautions to prevent nucleation of periodic arrays at the container surface. On the other hand, in the latter case, Bennett[45] and Adams and Matheson[46] began with three spheres in the form of an equilateral triangle as an initial cluster. The "global" criterion for adding spheres to this initial cluster consisted of enumerating all possible sites for which an added sphere would be in hard contact with three spheres already in the cluster but would not overlap with any of them. The site nearest the cen-

tre of the cluster was selected from this list and a sphere was added there. The list of possible sites was then updated, adding those created by the last sphere and removing those blocked by it. The dense random packings were generated by adding individual spheres following these criteria. The computer-generated DRP was similar to those obtained with steel balls as regards the coordination number and the splitting of the second peak in the calculated G(r). However, in the G(r)'s of these DRP models, the intensity ratio of the two components of the split second peak was reversed and the relative peak positions, r_2/r_1 and r_2'/r_1 were larger than those in the G(r)'s of amorphous metals. Sadoc et al.[47] and Ichikawa[48] employed a modified Bennett's algorithm and succeeded in reproducing the "normal" second peak splitting in the G(r) and relative peak position r_2/r_1. In their model assemblies, the packing fraction was much lower than that of $\sim$0.63 in the before and close to that of the liquid metals. The DRP models were improved and developed by the energy minimization of atoms using some assumed interatomic potential functions. Baker et al.,[49] von Heimendahl,[50] Connell,[51] Yamamoto et al.,[52] and Maeda and Takeuchi[53] showed that by using the interatomic potentials, like the Morse-type or the Lennard-Jones 6-12 potential, the relaxed DRP models of one chemical species gave the G(r)'s similar to those obtained from the diffraction experiments. In the medelling experiment by Maeda and Takeuchi, the initial atomic coordinates was made according to the computer-generated random ones. Heimendahl showed that the position r_2 of the first component of the split second peak in the G(r) was sensitive to the softness of the poten-

tial, and employed a Morse-type interatomic potential, of which the repulsive part is relatively soft compared with that of the Lennard-Jones 6-12 potential, in the construction of model structure. On the other hand, using molecular dynamics technique, the low temperature properties and the structure of amorphous state have been studied by Hiwatari et al.[54] Rahman et al.,[55] Kristensen,[56] Woodcock et al.,[57] and Tanemura et al.[58]

The types of local configurations in the DRP model structures, which are probably responsible for the split second maximum, have been investigated. Bernal[59] reported that his model structure is built up using only five different types of polyhedra or "canonical holes". Two of these polyhedra, the tetrahedron and the half octahedron, occur in crystalline close packings and one of the remaining three types, the trigonal prism capped with three half octahedra, are the basic unit of the chemical compound clusters, such as Fe_3B and Pd_3Si, which is described in the last section. Finney[43] also performed the polyhedron analysis for the Bernal model structure and studied the type of Voronoi polyhedra needed to build up the dense random packing of hard spheres. These polyhedra provide a means for defining the average number of the geometrical neighbours. Baker et al.[49] investigated local atomic arrangements in their model in terms of the Voronoi polyhedra and found an increase of the 13 atom icosahedral arrangement with the relaxation process. Whittaker[60] re-examined the cavity analysis for the Bernal model of hard spheres in detail and observed the trigonal prisms more frequently than the tetragonal dodecahedra. Yamamoto and Doyama[61] studied the geometrical connections of cav-

ities in addition to the polyhedron and cavity analysis, and estimated the dislocation density in their DRP model structure.

Cargill[62] pointed out that the G(r)'s of many amorphous metal-metalloid alloys, particularly electrodeposited Ni-P alloys, were very similar to those obtained by Finney and others for the DRP of single sized spheres. For the amorphous alloys, Polk[63] suggested that the non-metallic element would fill the larger holes inherent in the random packing, i.e. polyhedral holes as mentioned above and that they could stabilize the amorphous structure. In this case, the packing fraction of the DRP model aggregate was favourably increased. However, it is now clear that Polk's original evaluation of the fraction of non-metallic atoms which can be accomodated in regular Bernal holes was overestimated. Whittaker[60] and Yamamoto and Doyama[61] also revealed that the distribution of polyhedral type differed from the Bernal's estimation and that the Bernal polyhedra were distorted and departed significantly from their idealized shapes, and they could accomodate only larger atoms.

The DRP model calculations of the amorphous structure were recently further extended to include the binary alloys of metal-metal and metal-metalloid systems. Sadoc et al.[47] constructed several DRP models consisting of two sizes of hard spheres with the constraint that the smaller spheres, representing metalloid atoms, were not allowed to occupy adjacent sites. Their computer generated binary alloys contained about 300 atoms. The sharpness and height of the first maximum in the S(K) functions were determined by the relatively small size of their model assemblies, but the S(K) functions clearly showed the characteristic shoulder on

the second peak, particularly for the smaller sphere content of 15 %. Boudreaux and Gregor[64] constructed models by packing hard spheres of two diameters, scaled to simulate Fe and P alloys. The building algorithm was a random packing of hard spheres similar to that used for monoatomic systems by Bennett with additional constraints which ensure chemical homogeneity and the absence of nearest-neighbour P-P correlations. The resulting DRP model failed to reproduce the observed density and coordination numbers, which were higher than those of the model. One of the more remarkable properties of the model is the orientational anisotropy of the G(r) function. They attempted the energy minimization of above mentioned DRP structures for the amorphous Fe-P alloys using the Lennard-Jones 6-12 potentials for Fe-Fe, Fe-P and P-P pairs. The properties of the relaxed DRP model structure, such as the coordination number, the density, the pair correlation function and the interference function, were found to be in tolerable agreement with the experimental results with a negligibly small orientational anisotropy in the G(r) function. Boudreaux[65] and Fujiwara et al.[66] also constructed models for the amorphous Fe-B alloys by packing spheres of two different sizes. The ratio of the diameter of atoms to that of iron atoms was taken to be 0.52, which is smaller than the corresponding ratio of 0.72 in the DRP models for the amorphous Fe-P alloys by Boudreaux and Gregor and Fujiwara and Ishii.[67] The building algorithm consisted of a random packing procedure and a relaxation using assumed interatomic potentials with a constraint which ensures the absence of nearest neighbour B-B correlations. The calculated G(r) functions for three compositions: 15, 20 and

25 at%B obtained by Boudreaux showed a "reversed" second peak splitting. In the calculation by Fujiwara et al., the G(r) function for an $Fe_{85}B_{15}$ amorphous alloy was found to have a "reversed" second peak splitting as well as the results by Boudreaux. Furthermore, they derived approximations to the partial G(r) functions for the amorphous $Fe_{83}B_{17}$ alloy from the combination of x-ray and neutron data by Cowlam et al.[22] In their work, the partial G(r) function for the Fe-Fe pair showed a "reversed" second peak splitting as was anticipated, since the total G(r) function obtained by x-rays had a similar feature. However, the results of diffraction experiments, especially those by Fukunaga et al., could not be satisfactorily reproduced by the above DRP models. The experimental results on the structure of the amorphous Fe-B alloys are already described in detail in the subsection 1.2.1.

A computer-relaxed DRP model was described by Suzuki[68] in which a model was refined by the simple expedient of moving each atom to the centre of the polyhedron formed by its neighbours. Even in this case, the calculated G(r) function fitted to the experimental curves deduced from the neutron scattering measurements of the amorphous $Pd_{80}Si_{20}$ alloy. These computer modelling experiments suggest that any energy minimization algorithm may produce the amorphous like structures despite the relatively large uncertainty in the choice of force constants. It should be emphasized that energy minimization procedures used for the construction of the DRP model structure do not maintain the topology of the original structure. Boudreaux[65] suggested that the improved representation of the amorphous structure achieved by the relaxation of

DRP models was essentially due to the changes in local coordination with an increase in the proportion of some relatively well-defined molecular units. The DRP models of the amorphous Pd-Si, Fe-P and Fe-B alloys were examined in relation to the short range order of their atomic structure by Boudreaux and Frost.[69] The types and numbers of near-neighbour atoms were calculated in detail, from which it was argued that a specific coordination was preferred and satisfied by a local unit structure around each metalloid atom. Furthermore, the local geometry was examined by computer graphic methods and it was discovered that the two local geometries dominated the surroundings of metalloid species: the octahedron and the trigonal prism.

In order to explain the high resolution electron micrographs of the amorphous metals and alloys, Graczyk and Chaudhari[70] calculated the interference image contrast of the dense random packing of hard spheres by using the kinematical theory of diffraction. With the tilted beam configuration, they showed a snake-type regularity extending over at least 10 A × 10 A of the image. The contrast of this type was not seen in the untilted symmetrical beam configuration, but, instead, a vague fringy contrast was obtained when the spherical aberration constant and the defocus value were properly chosen in the calculation. They concluded that this is a phase contrast rising from the structural anisotropy in the DRP model structure.

1.3.2 Chemical cluster model

The similarity between experimental scattering data for amor-

phous alloys and for the corresponding crystalline phases as described in the section 1.2.1 supports the view that non-metallic atoms may exist in the ordered environment rather than in the larger holes inherent in the random packings of metal atoms. Especially, the nine-fold coordination of metalloid atoms suggests that the atomic arrangement in this ordered region is similar to that observed in the corresponding crystalline phases. The crystalline borides, phosphides, carbides, silicides, etc. of transition metals, which readily form the amorphous alloys of transition metals with non-metallic elements, have lattices containing a common structural unit consisting of a non-metal surrounded by six metal atoms arranged in a distorted trigonal prism with three further neighbours at somewhat larger distances. Furthermore, this structure persists over wide range of compositions and radius ratios, which indicates that this type of packing is stabilized by the chemical interactions.

In an earlier calculation to reproduce the correlation function for metal-metal pair of the amorphous Fe-Pd-P and Ni-Pd-P alloys for the radial distance less than 6 A, i.e. in the region of their first three maxima, Maitrepierre[71] used the unit cell of Pd_3P as the basic structure, and took the broadening factors for individual peaks and the critical correlation distance as adjustable parameters. This approach emphasizes the short range order in the amorphous alloys. Gaskell[72] constructed a model for the amorphous $Pd_{80}Si_{20}$ alloy based on the random packing of trigonal prismatic units. The arrangement of trigonal prisms resembles that observed in the cementite, Fe_3C, structure and is also the typical

structure of crystal phase formed by the devitrification of the amorphous metal-metalloid alloys. The model structure was relaxed using a Lennard-Jones 6-12 potential, with some additional constraints included to preserve trigonal prismatic coordination. The computed G(r) were, then, convoluted with Gaussian broadening functions which simulate the effects of thermal vibrations and transformation of reciprocal-space data, S(K), over a limited spectral range. The calculated G(r) and S(K) were found to give a good representation of the experimental neutron scattering data measured to high K value, 30 A^{-1}. However, the fine structure on the second peak in the G(r) as described before was not fully reproduced.

Taking account of the similarity of partial pair correlation functions between amorphous $Fe_{75}P_{25}$ alloy and the crystalline Fe_3P, Kobayashi et al.[73] constructed a computer model according to the computer-generated random coordinates and the relaxation. In the procedure of the energy minimization of model structure, a non-spherically symmetric interatomic potential for Fe-P pairs, which was assumed to stabilize trigonal prismatic units similar to that constituting Fe_3P crystal, was employed. The obtained partial G(r)'s agreed with the experimental x-ray scattering data, which suffered considerable truncation effects in the Fourier transformation of the S(K) functions. Aur et al.[74] obtained the G(r)'s for the amorphous $Fe_{75}B_{25}$ and $Ni_{50}Fe_{25}B_{25}$ alloys using those of Fe_3B and Ni_3B crystal in a similar way by Maitrepierre. The calculated G(r) functions, each peak of which was broadened by a Gaussian function, exhibited a strong similarity to the experimentally ob-

tained ones by them.

1.3.3 Microcrystalline model

In the earlier stage of modelling experiments, models for the amorphous structure were classified as those in which most of the atoms are arranged in very small well defined crystals, the long range structural periodicity being absent because of randomness in orientations of these microcrystals, and the DRP models mentioned before.

The microcrystalline model was appealing because the most prominent peaks in the interference functions for many of the amorphous metal-metalloid alloys occurred close to the Bragg peaks in diffraction patterns of corresponding crystalline phases. The diffraction theory for the structure consisting of smallest crystalline aggregates was examined at first by Germer and White.[75] Peaks in crystalline scattering patterns can be broadened by small crystal sizes, by inhomogeneous strains, and in some cases by high densities of stacking faults. The calculation of scattering from n identical and randomly oriented small crystals has been based on the Debye equation

$$I(K) = n \sum_{i}^{N} \sum_{j}^{N} f_i f_j^{*} \sin(Kr_{ij})/Kr_{ij} , \qquad (1)$$

where N is the number of atoms in one microcrystal, K the magnitude of the scattering vector, r_{ij} the distance between atoms i and j, f the atomic scattering factor, and the summation is over all atoms in one microcrystal. The interference among scattered

amplitudes from different microcrystals is neglected, i.e. they are assumed to scatter independently. The calculated scattered intensity function I(K) and the interference function S(K)(=I(K)/Nnf^2) show broadened peaks because of the small crystal size. Effects of thermal and static displacements of atoms from their equilibrium positions may incorporated in this type of the calculation by multiplying the intensity distribution of the model by a Debye-Waller damping factor $\exp(-\langle u^2\rangle K^2)$ and adding a monotonically increasing background term $1-\exp(-\langle u^2\rangle K^2)$. Dixmier et al.[76] and Cargill[17] carried out such microcrystalline model calculations by assuming f.c.c. or h.c.p. microcrystals for the structure of the electrodeposited Ni-P amorphous alloy and could not obtain the agreement with the experimental S(K) function. However, the S(K) functions calculated in this way were useful in establishing the microcrystalline nature of some evaporated films. Wagner et al.[77] showed a similarity between the calculated S(K) for 125 atom f.c.c. microcrystals and experimentally obtained S(K) for the $Ag_{48}Cu_{52}$ film of 1 μm thickness deposited on a silica substrate cooled to liquid nitrogen temperature. In this case, the comparisons with the experiments indicated that for crystal sizes large enough to yield the sharpness in the first peak of the experimental S(K), the subsequent peaks in the model S(K) were too sharp and too intense.

The validity of the Debye equation method for calculating the microcrystalline model I(K)'s and S(K)'s might be questioned because possible interference effects among scattered amplitudes from different microcrystals are neglected. The numerical calcu-

lations by Betts and Bienenstock[78] indicated that the intercrystal interference terms were significantly smaller than the intracrystal terms in all but the small-angle region, under the assumption of no correlations between orientations of neighbouring microcrystals. In this respect, Galeener and Rodoni[79] did the calculations including orientational correlations and showed that microcrystals separated from one another by small-angle grain boundaries produced the scattering patterns similar to those of larger and independently scattering microcrystals. Cargill[17] also examined the effects of the strain distribution on the S(K) function of the microcrystalline model by taking the Gaussian strain distribution to the breadth at half-maximum of a resolved Bragg peak into consideration. Cargill also investigated the effects of stacking faults on the S(K) function. However these approaches for testing hypothetical microcrystalline structural model did not improve the qualitative agreement with the experimental data. It is unclear which combinations of size, strain and crystal structure are physically resonable.

Potential problems with microcrystalline structural models for amorphous metal-metalloid alloys also arise because measurements indicate that these alloys have densities within two percent of corresponding crystalline phases. Large-angle grain boundaries are expected to decrease the density of polycrystalline solids because of the finite core sizes of atoms and the restrictions placed on atoms in boundary regions by structural order of the crystalline grains. Approximate calculations to improve the density deficit associated with large-angle grain boundaries are inconsistent with

crystal sizes deduced from the application of the Scherrer particle size broadening equation to scattering patterns of these amorphous alloys.

Some calculations to reproduce high resolution electron images of amorphous Si and SiO_2 were carried out by using the microcrystalline models. Howie et al.[80] calculated the dark-field and offset bright-field electron micrographs of the microcrystalline model and of the random-network model for the amorphous SiO_2 based on the kinematical theory of diffraction. The experimental observation of bright spots of larger than 10 A in diameter in dark-field and of lattice fringes in interference micrographs were well explained by the microcrystalline model but not by the random-network model. Cochran[81] carried out a similar calculation for the random-network model of the amorphous Si, and found that the random-network model accounted qualitatively for many of what were observed in electron micrographs except those obtained by Howie et al. using the offset bright-field condition, which appeared to require the presence of small crystallites. Krivanek and Howie[82] computed the kinematical electron microscope images from the Polk continuous random-network model and a polycrystalline cluster model under the condition of the tilt illumination. Dark-field images of both models showed qualitatively similar speckle patterns. Fringes appeared in bright-field images from the polycrystalline model when the thickness was smaller than 40 A, but they disappeared in thicker samples because of the overlap effect and were totally not found in the Polk-model images. When the thickness exceed 50 A, their calculation did not predict any noticeable difference in the image from different mod-

els nor did it explain the observation of fringes from such specimens.

1.3.4 Dislocation model

There have been considerable discussions on the melting phenomena associated with the spontaneous generation of dislocations. The dislocation model of liquid state by Cotterill et al.[83] gives a liquid like pair correlation function when the dislocation density reaches a certain high value of about 3×10^{14} cm^{-2}, in which dislocations are separated about three atomic distances from each other. In this case, the second maximum split in the G(r) of the f.c.c. structure is reproduced as the dislocation density is increased.

Suzuki[84] proposed the dislocation model on the process of formation of amorphous metals. He attributed the rapid increase of the viscosity of supercooled liquids and the stability of the amorphous metals to the interaction between solute atoms and dislocations as well as the dissociation of dislocations into partials accompanied by stacking faults, multiple twins, etc. On the other hand, Ninomiya [85] calculated the S(K) function by assuming that the structure was composed of randomly orientated microcrystals which contain a dislocation in each crystal. Interference among scattering amplitudes from the domains separated from each other by the dislocation was found to make the first peak of the diffraction pattern sharp and intense and to change the shape of the second peak. In this respect, he showed that when a 60° dislocation or screw dislocation is introduced, an octahedron inherent in the

close-packed crystalline structure is transformed into a tetragonal dodecahedron or trigonal prism, which are observed in Bernal's dense random packing structure. Koizumi and Ninomiya[86] also constructed the dislocation model of the amorphous structure, in which many screw dislocations were introduced in a f.c.c. lattice in order to produce local disordered structure and destroy its long range order. The final atomic positions were obtained by the relaxation of the dislocated structure using the Morse type interatomic potential. For the dislocation density of 1.1×10^{15} cm^{-2} or 4.3×10^{14} cm^{-2}, the calculated G(r) function was found to be in good agreement with the experiments. From the geometrical analysis, they showed the global connectivity of particular types of non-crystalline polyhedra inherent in the DRP model structure. However, it seems to be very difficult to identify a dislocation in such dislocated and relaxed model structure, since dislocations are separated by only a few atomic distances.

1.3.5 Crystalline embryo model

Many recent experimental results as mentioned in the section 1.2 suggest that in the amorphous structure atomic ordering is developed to a considerable extent possibly far beyond the first neighbour atomic distance. As was first pointed by Frenkel,[87] the liquid structure may have a local order which could be regarded as the quasi-crystalline structure. Accordingly, the short range and further range order found in the amorphous structure is considered as a growing and frozen inheritance from supercooling liquid, while disorder or randomness is a reducing and frozen property inherited

from the same parent.

In order to describe the well developed ordering in the amorphous structure, Fujita[88] has proposed a thermodynamical theory and calculation on the quasi-crystalline liquid and its solidification of pure matals and stoichiometric binary alloys. In his theory, it is assumed in the first place that the Gibbs' free energy of the hypothetical perfectly disordered liquid state can be lowered by the development of quasi-crystalline ordering. In a quasi-crystalline cluster consisting of i atoms, enthalpy and entropy will be reduced by ε and ϕ per atom respectively and, in addition, the entropy of mixing of clusters and unclustered atoms will appear. The free energy changes will be, then, as a rough approximation,

$$\Delta G = -ni(\varepsilon - T\phi) - k_B T \ln \frac{(N-ni+n)!}{(N-ni)!n!}, \qquad (2)$$

where N is the total number of atoms, n that of clusters, and k_B the Boltzmann constant. More precise expression given by the same author[89] with an improvement of the configurational entropy term, corresponding to the last one in the above equation, is

$$\Delta G = -C[\varepsilon(i) - T\phi(i)] + RT[\frac{C}{i}\ln\frac{C}{i\xi} + (1-C)\ln(1-C) + C(1-\frac{1}{i})], \qquad (3)$$

where C is the total fraction of the clustered atoms, ξ the number of shape diversity of a cluster and R the gas constant. $\varepsilon(i)$ and $\phi(i)$, depending on the size i, are expressed by per mol. From the free energy minimum condition concerning the variable, n, i.e. $\partial\Delta G/\partial n = 0$, at a fixed cluster size, the relation between T and C

(=ni/N) are obtained depending on the cluster size, i, by using the assumed values of ε and ϕ for copper, for instance. The changes of the average cluster size, i, with temperature is also evaluated from the free energy minimum condition, $(\partial\Delta G/\partial i)_n = 0$. In Fig.6 is shown a C-i-T diagram calculated from the above simultaneous energy minimum conditions, where full lines correspond to the equilibrium concentration of quasi-crystalline clusters at fixed cluster sizes. Clusters smaller than i = 8 would be insignificant as the quasi-crystalline state, while those larger than i = 100 would not appear significantly since they could exceed the critical size of nucleus for the crystallization from liquid or solidification. In this respect, the quasi-crystalline clusters in supercooled liquid may be called as the "crystalline embryos". This word has been generally employed to represent the ordered cluster in the amorphous structure in the present author's later papers and in the present article. It can be seen from the figure that the smaller the quasi-crystalline clusters the higher their concentration at high temperatures. For instance, the clusters with i = 8 are predominant and no large clusters appreciably appear at the melting point, T_m. When the liquid is supercooled, larger clusters gradually appear and increase as the temperature is lowered, and ultimately the larger ones exceed the smaller ones in number near the critical temperature, Tq. The optimum cluster size must vary with temperature as shown in the figure by a broken line on the curved surface made by the above full lines and also given as a projected curve, i*, on the i-T plane. The same behaviour is expected for the chemical clusters. By the rapid quenching from

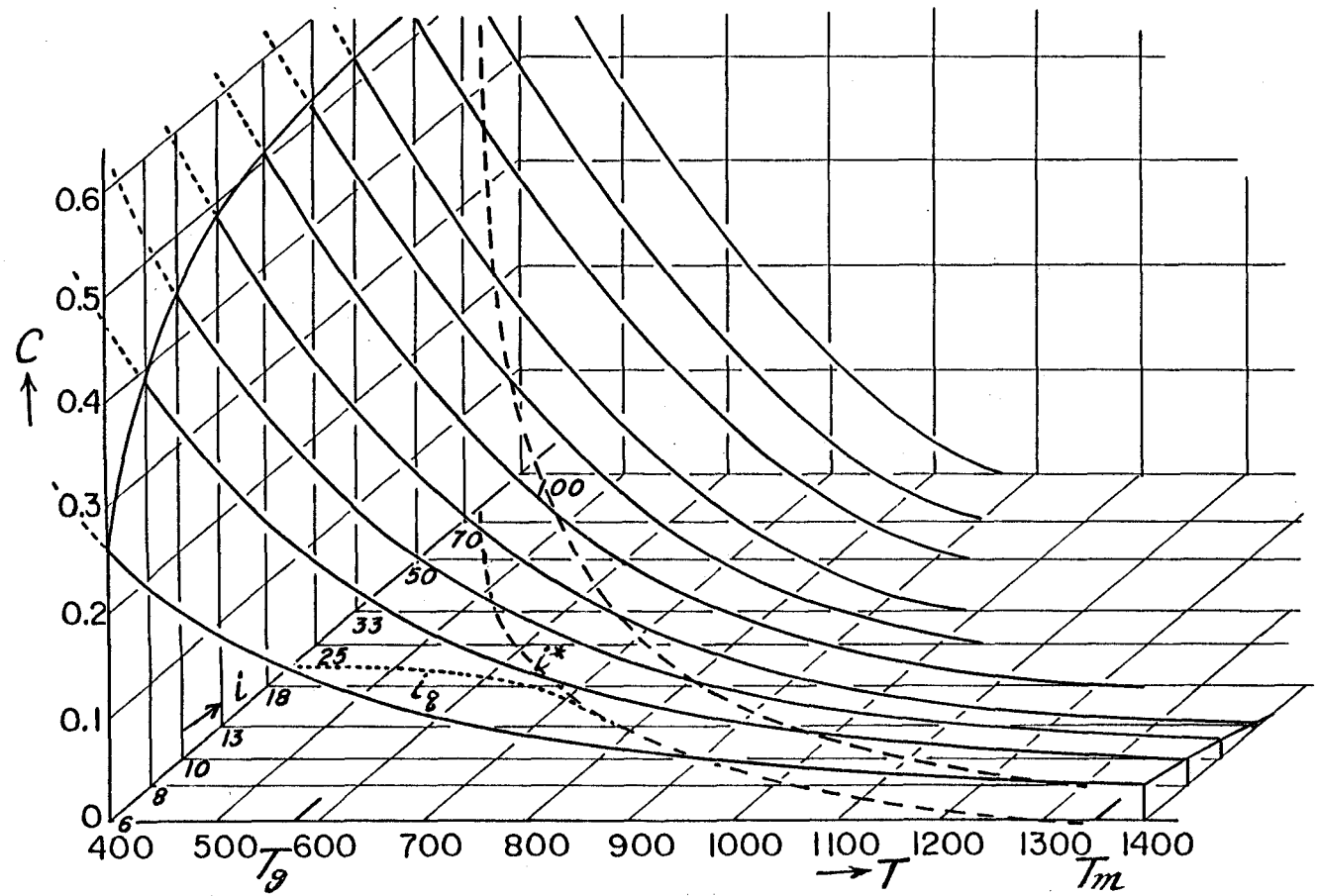

Fig. 6 The concentration and average size of quasi-crystalline clusters in the liquid calculated by Fujita. Dashed lines show the quasi-equilibrium state, and dotted lines shows a non-equilibrium state obtained by rapid quenching.

the melt, the quasi-crystalline and/or chemical compound clusters will grow up in the number and size during the short time of supercooling before the glass temperature, Tg, is reached. On the other hand, at around Tg atomic jumps necessary for the growth of the clusters will be largely suppressed and, at the same time, all atomic movements will be frozen, resulting in the formation of the amorphous structure with a considerably high degree of order. In this case, the average cluster size will be unable to grow fast enough to follow the equilibrium size, i*, but become smaller as an i_q curve in the figure shows. The larger the clusters, the longer will be the time needed to grow. Therefore, large quasi-crystalline aggregates such as i = 100 would not be expected but a great number of the intermediate size clusters from i = 10 to i = 40 would appear, giving rise to the medium range order in the amorphous structure.

Taking such high degree of atomic orderings into consideration, Hamada and Fujita[3] have proposed the crystalline embryo model for the structure of amorphous metals and alloys and, as a more realistic structural model, constructed an assembly of atoms consisting of the crystalline embryos and the disordered boundary region coexisting and continuously and smoothly connected each other. The before mentioned fact that Mössbauer spectra of Fe-P-C and Fe-B amorphous alloys were successfully analysed by assuming the b.c.c.-like near neighbour configurations suggests that the basic structure of the embryos in these alloys would be of the b.c.c. crystal form. This seems to be in good agreement with experimental fact that, in the very early stage of crystallization of the iron-based amorphous alloys containing iron exceeding the chemical compound

compositions, the smallest crystallites first observed by any experimental technique are the b.c.c. α-iron particles. The crystalline embryo model satisfactorily reproduces the diffraction functions and the high resolution electron images from the medium range order in the disordered structure, which will be described and discussed in this thesis.

2. CRYSTALLINE EMBRYO MODEL

There exist much evidences of high degree of ordering in the amorphous state in various experimental results, as described in the section 1.2. In this section, first the origin of structural ordering in the amorphous alloys exemplified by those made by rapid quenching from the melt is considered. One might argue that the idea of the structure consisting of smallest crystalline aggregates would collapse when subjected to the examination by the diffraction theory, as mentioned in the microcrystalline model. However, it is shown in the second place that an important correction to the microcrystalline diffraction theory is necessary and according to that a completely different conclusion can be drawn. In the following parts of this chapter, the construction and the improvement of the crystalline embryo model, which contains both the crystalline embryos and disordered boundary regions coexisting and continuously connected each other, is described.

2.1 Basic Concept of Crystalline Embryo Model

2.1.1 Origin of crystalline embryos

The rapid quenching from the melt seems to be the most efficient method to produce the amorphous alloys. This method gives us an intuitive picture that the structural disorder in the amorphous structure is simply inherited from the molten state or the liquid structure. However, the degree of order in the former is undoubtedly higher than in the latter, as mentioned in the section 1.2. In this respect, Fujita[88,89] has proposed a statistical thermodynamical theory of the medium range order. Hamada and Fujita[3] have also proposed the crystalline embryo model for the structure of amorphous metals and alloys. To begin with, the process of the rapid quenching from the melt and the nature of the frozen-in disordered or ordered structure are carefully examined in this subsection.

Let us first consider anything like the average volume of the constituent atoms of the alloy to be produced as an amorphous material. Thermodynamically the most suitable quantity for that purpose is probably the free volume, V_f, which means the statistical average volume in which each atom can vibrate and move around. In Fig.7 is shown the free volume as a function of the temperature. When an alloy is in the crystalline state, the volume increases nearly linearly with the temperature increase, exhibiting a nearly constant thermal expansion. When it reaches the melting temperature, Tm, it suddenly becomes unstable and transforms to the liquid state, where a large volume expansion, V_h, appears in addition to the amount, V_c,

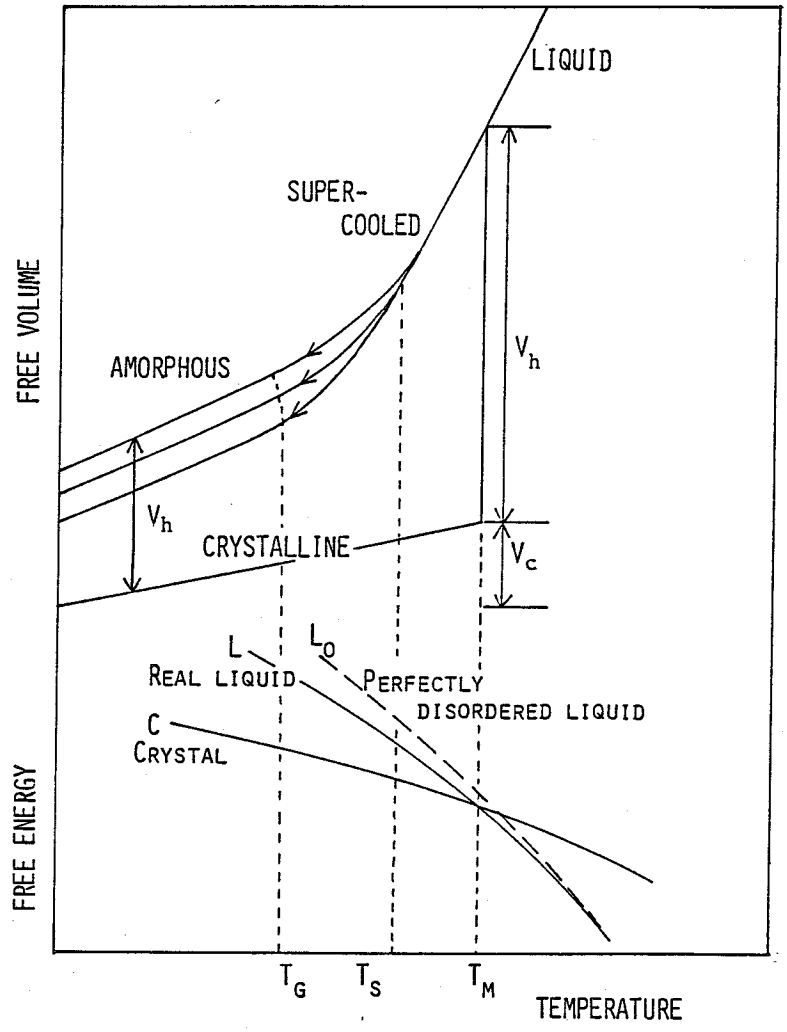

Fig. 7 The crystalline solid, liquid and amorphous state in the free volume and free energy vs temperature diagram.

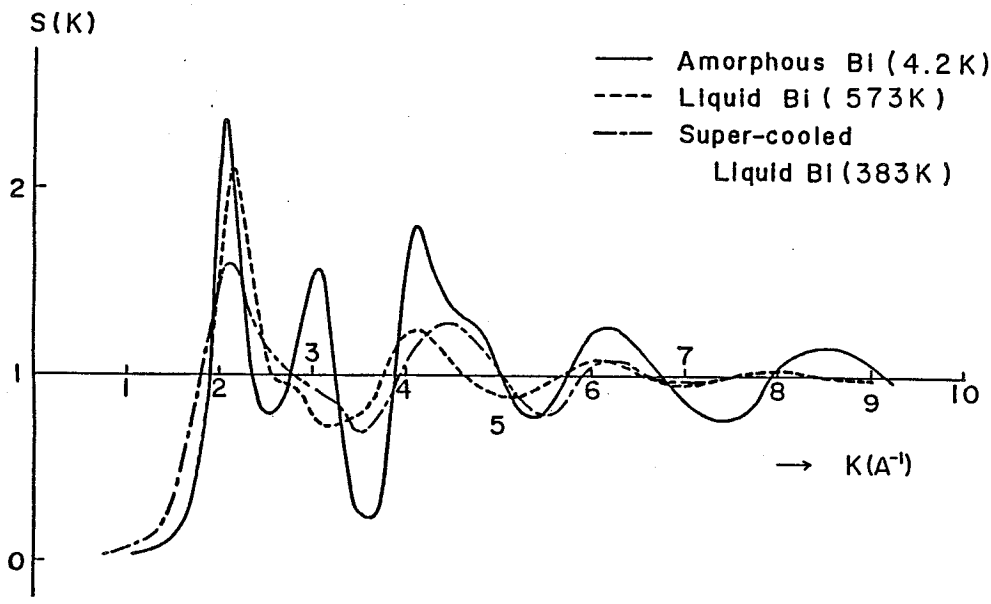

Fig. 8 The S(K) functions:——— amorphous Bi film at 4.2 K given by the present author and others,– – – – liquid Bi at 573 K given by Waseda et al., and —— — — supercooled liquid Bi at 383 K given by Takagi.

rising from the thermal expansion of the crystal lattice. This excess volume can be regarded as the expanded range of atomic vibration due to the relaxed potential formed in the average in the disordered liquid structure or as the total volume of holes formed in the liquid, although in the liquid state V_c and V_h are not always distinguishable from each other. Differing from the atomic vacancies in crystals, the atomic holes in liquid must be diffused, deformable and moving around almost continuously, exchanging their positions with atoms, that is, being commonly possessed by atoms and fully covered by the range of atomic vibration. The latter point of view is no other than that of the hole theory of liquid. The thermal expansion coefficient of liquid is larger than that of solid, because the ratio of increase of disorder with increasing temperature in liquid is much larger than in solid, or in other words, formation of vacancies in liquid is much easier than in solid. When liquid is cooled, it will be more or less supercooled below Tm, during which crystalline nuclei will be formed from some embryos mentioned before and grow to complete the crystallization. Sometimes it is possible to keep the supercooled state at a temperature, Ts, far below Tm before the crystal nucleation starts. Takagi[90] made the supercooled state of bismuth and took the electron diffraction halo patterns. In Fig.8 are shown the interference functions of this supercooled liquid Bi at 383 K, the liquid Bi at 573 K given by Waseda et al.[91] and the amorphous Bi film at 4.2 K given by Hamada et al.,[92] which was made by vacuum deposition on the cold substrate kept at liquid helium temperature. A small hump at $K \simeq 2.7$ A^{-1} in the S(K) function of liquid is enhanced and

becomes a distinct shoulder of the first halo peak in the supercooled state. This clearly shows that, as the temperature of liquid is lowered as in the supercooled state, ordering of a high degree will proceed in the structure in parallel with a large reduction of the free volume which is shown in Fig.7.

When the liquid is not slowly cooled but rapidly quenched far down to a low temperature with a cooling rate as high as $10^{5\sim6}$ K/s, the time for crystal nucleation will not be enough and a frozen state, in which the viscosity is so high that the atomic vibrations do not induce the atomic jumps, position exchanges and structural relaxations, will be achieved at a certain temperature, Tg, which may be called the glass point. Below Tg, the supercooled disordered state will be immobilized, and atomic vibrations will resemble those in the crystalline solid rather than in liquid. This means that the thermal expansion coefficient of such a frozen state must be not far from that of crystal irrespective of a considerably large free volume, as are shown in the figure. This frozen state is no other than the amorphous state. The excess free volume of the amorphous state is smaller than that of liquid, but is still far larger than that of crystal. In the liquid structure, the two kinds of free volume, V_c and V_h, are completely mingled and can not be differenciated, but in the amorphous state V_c is not quite different from that of crystal and almost all the volume V_h is already excluded from the range of atomic vibration, representing only static holes or interstices in the disordered structure. This should, therefore, be called the "dead free volume".

The above picture of the process of formation of amorphous

state by rapid quenching from the melt naturally leads us to the conclusion that ordering in the atomic arrangements may exist as small clusters already in the liquid structure. But, such quasi-crystalline clusters must be different from the real crystallites in the sense that the former are of sub-critical size and dynamical, appearing and disappearing with a relaxation time of the order of $10^{-6\sim-10}$ sec.[88] Frenkel[87] described such a fluctuating ordered state as in the above and called it the "cybotactic structure" following Stewart.[93] As the temperature of the liquid is lowered, their number, average size and lifetime will increase as shown in Fig.6 and the degree of disorder and, accordingly, the free volume will decrease, as are predicted in Fig.7. By the rapid quenching from the melt, the quasi-crystalline clusters will be frozen as the static crystalline embryos together with the disordered region and will ultimately compose the amorphous structure. The degree of order or disorder frozen in the amorphous structure will largely depends on the rate of cooling, and, therefore, many free volume vs temperature curves should probably be drawn as in the figure.

Nold et al.[94] did the x-ray diffraction experiments on two molten $Fe_{90}B_{10}$ and $Fe_{83}B_{17}$ alloys at about 50°C above their melting points and found that the second maximum of the interference functions S(K) had a small shoulder in both cases, which has been considered to be characteristic of only the amorphous metals. As mentioned in the sebsection 1.2.1, the G(r) function of the liquid $Pd_{80}Si_{20}$ alloy showed a shallow hump at the smaller K value beside the first maximum instead of a distinct subpeak in the amorphous state, the latter being attributed to the chemical order of crys-

talline Pd_3Si type. These facts including the case of the supercooled liquid Bi could be connected with the quasi-crystalline clusters existing in the liquid and supercooled liquid state.

Computer simulation of the process of supercooling by means of molecular dynamics technique was carried out by Hsu and Rahman[95] and Tanemura et al.,[58] and they concluded that in certain cases ordered clusters with b.c.c.-like and f.c.c.-like atomic arrangements appeared in the supercooled state and continued to grow in a short time to engulf the entire system. This looks to be in accordance with the above picture of the crystalline embryo formation.

2.1.2 Diffraction from a microcrystallite

In the microcrystalline model so far treated, an amorphous state is considered to be an assembly of extremely small crystallites, which have no correlation of orientations and interference between each other. By analysing the diffraction patterns of the amorphous iron and nickel films condensed on the cold substrate kept at the liquid helium temperature, Ichikawa[7] obtained the interference functions, S(K), and compared them with the calculated S(K) functions of various microcrystalline models. He assumed that the interference function was fully represented by that of a microcrystallite, as above mentioned, and no correlation with its surroundings existed. The main features of the experimental diffraction intensity curves were not reproduced by the calculation, even if a heavy structural disorder was introduced into the pair correlation function by the Gaussian broadening of each radial shell.

The S(K) function for an assembly of single element atoms is given by using Eq.(1) in the form,

$$S(K) = I(K)/Nf^2$$

$$= 1 + \frac{1}{N} \sum_{i \neq j} \frac{\sin(Kr_{ij})}{Kr_{ij}}, \qquad (4)$$

where N is the number of atoms in the assembly, K the magnitude of the scattering vector, r_{ij} the distance between atoms i and j, and the summation is over all atom pairs in the aggregate. Generally, as the size of the crystalline aggregate is decreased, the interference function gradually loses its sharpness and the interference peaks become broader. In Fig.9(a) is shown the S(K) function calculated using the Eq.(4) on a b.c.c. microcrystallite composed of 35 atoms. The lattice parameter is chosen as 2.8665 Å which corresponds to α-iron at 20°C. The S(K) function is considerably diffuse due to the reduced interference effect among the small number of atoms in the microcrystallite. The peak positions of the first and second maxima correspond to the (110) and (211) reflections from the ordinary large size crystals respectively, while the intensity maxima corresponding to the (200), (220) and (222) reflections are almost missing.

Once a (112) twin, which is familiar in fine particles of α-iron,[96] is introduced into this microcrystallite, the S(K) function becomes more diffuse owing to the break down of the normal crystalline periodicity at the twin interface. Nevertheless, as shown in Fig.9(b), more remarkable change is that the interference intensity rises up around $K = 6.2\ A^{-1}$, at which a high angle should-

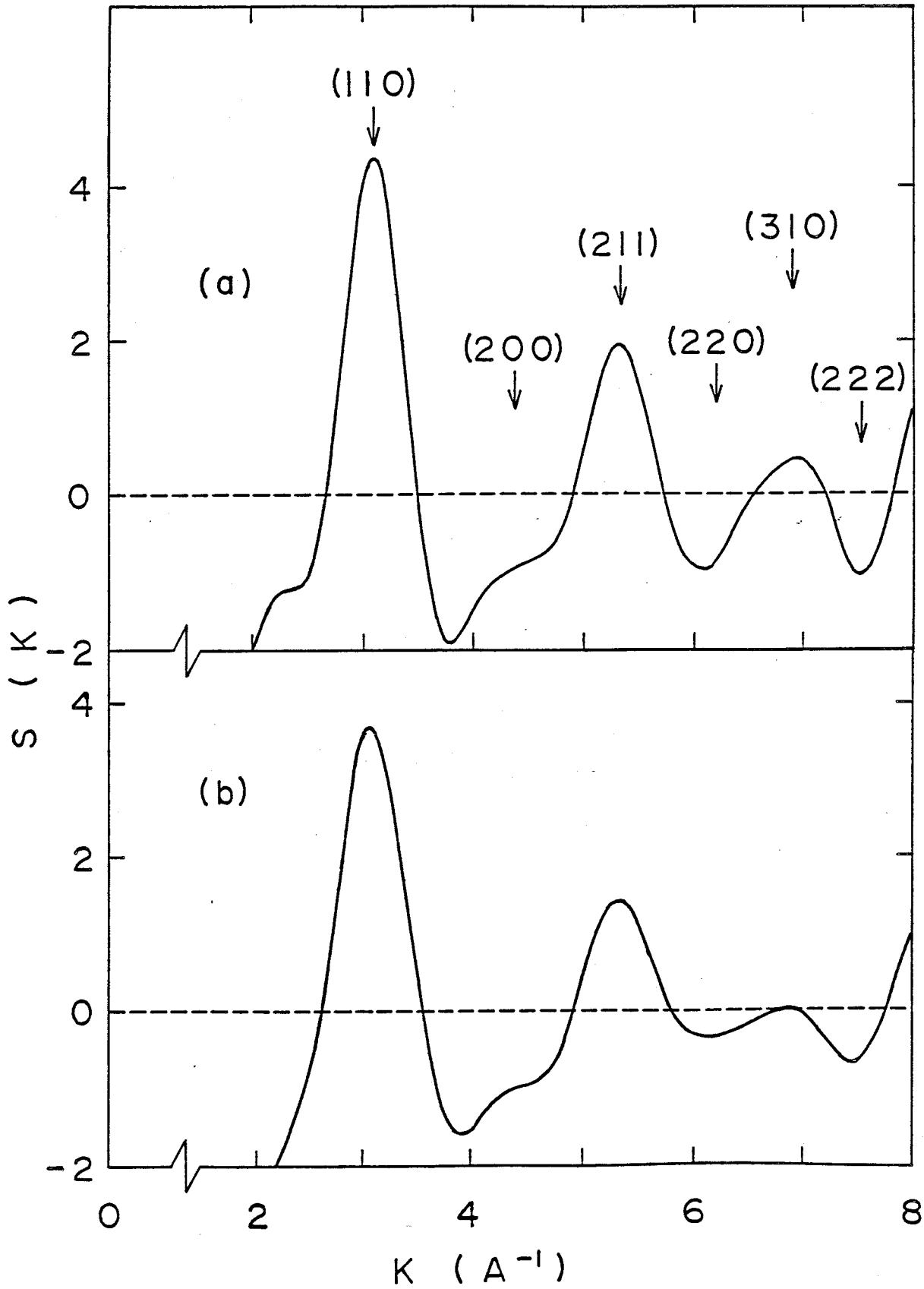

Fig. 9 The S(K) functions of a b.c.c. microcrystallite composed of 35 atoms: (a) with no defects, and (b) with a (112) twin. The lattice parameter is 2.8665 A corresponding to α-iron at 20°C. The arrows indicate the positions of reflections from the large size b.c.c. crystals.

er of the second halo peak is usually observed in the diffraction patterns of amorphous materials. Atoms in one side of the twin interface have a special relation in the configuration with those in the other side, which is different from the b.c.c. crystalline periodicity. This makes particular phase differences and inevitably changes the S(K) function around $K = 6.2\ A^{-1}$. In the application of the microcrystalline diffraction theory to the amorphous materials, improvement of the calculation similar to the above modification by twinning seems to be indispensable, since no isolated microcrystallites or crystalline embryos exist in the amorphous structure but they are always jointed together through the disordered boundary regions. Atoms in the boundary regions unavoidably break the crystalline periodicity which is kept within the embryos, and it will lead to essential changes in the G(r) function and the S(K) function of the microcrystalline model. Results of actual calculations will be shown later. It might be worth of pointing out that the smaller the size of embryos the larger the number of adhereing boundary atoms and consequently the microcrystalline diffraction theory, which does't take the boundary atoms into account, will become more useless.

2.2 Model Construction for Amorphous Iron and Nickel

In the last subsection, we have shown that the S(K) function of a b.c.c. microcrystallite is modified by introducing a twin boundary. This strongly suggests that as a realistic model an assembly of atoms consisting of the crystalline embryos and the boundary regions connecting them could be constructed to reproduce the characteristic diffraction intensity distribution of the amorphous metals. In this section, we will show how such embryos are packed together and the boudary layer atoms are arranged to form a rigid and compact amorphous structure.

The b.c.c. or f.c.c. crystalline embryo model is schematically represented in Fig.10. As the simplest case, the three-dimensional assemblies each composed of 397 or 677 atoms of single element, corresponding to iron or nickel respectively, are constructed by computer. The b.c.c. or f.c.c. structure is chosen for the crystalline embryos, which are represented by circled regions (A and B) in the figure. Surrounding each embryo is the disordered boundary regions, which are shaded in the same figure (C). As mentioned in the subsection 1.3.5, from the thermodynamical consideration and calculation of quasi-crystalline liquid and its solidification, Fujita[88,89] suggested that a great number of the intermediate size clusters from 10 to 40 in number of atoms may exist in the as quenched amorphous alloys. Therefore, embryos in the model structure would have the size of the same order as his prediction. In the calculation, the embryos have a nearly spherical shape, containing the same number of atoms of about 50, and have no correlation in orientations with each other. They are separated by one

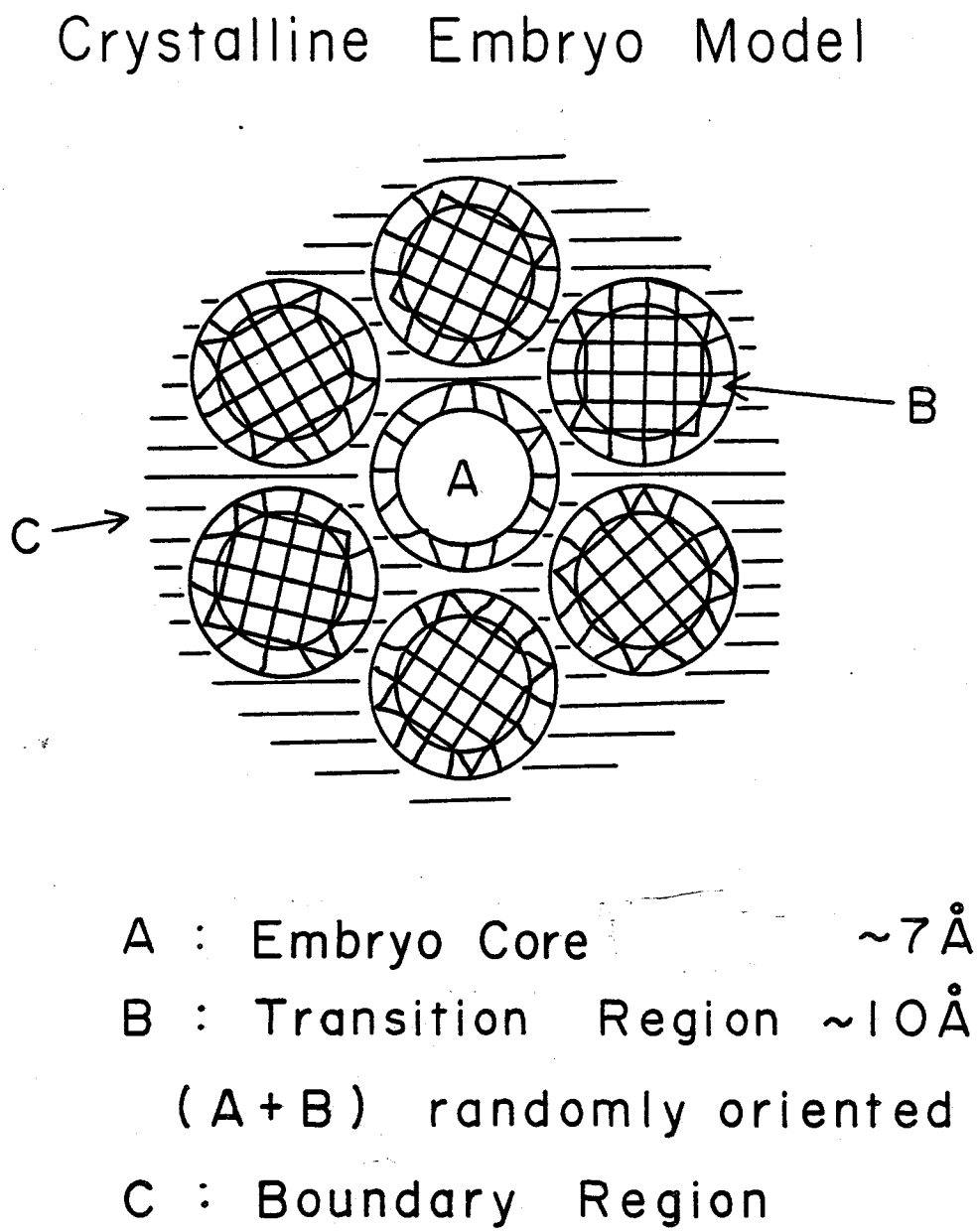

Fig. 10 Schematic view of the crystalline embryo model for amorphous Fe and Ni. A: the embryo cores with b.c.c. or f.c.c. structure. B: the transition regions of the embryos. C: the disordered boundary regions.

or two atomic distances, in which boundary atoms are packed closely. In the actual process of constructing the amorphous structure, atoms with a given diameter are at first distributed at random in the overall volume according to the computer-generated random coordinates provided that any two atoms do not interpenetrate each other, until the system has a certain packing fraction. Then, atoms of embryos are put into the system replacing the overlapped atoms already existed. The packing fraction in the calculated models is chosen from 0.66 to 0.70, which is a little lower than that of the b.c.c. or f.c.c. structure and yet higher than that of their liquid state. In order to connect neighbouring embryos as smooth and as tight as possible, atoms both in the boundary regions (C) and in the outer part of embryos (B) are relaxed by using an interatomic potential. For the b.c.c. embryo model Pak-Doyama potential of α-iron[97] is employed and for the f.c.c. embryo model is an interatomic potential presented by Huntington.[98] As a result of relaxation, the displacements from the initial positions of atoms close to the surface of each embryo, i.e. the transition regions, are sometimes of the order of the interatomic distance, but those of the atoms near the core of each embryo are lower than 0.1 A. The projections of positions of half of atoms belonging to a b.c.c. embryo core and its surrounding transition region after the relaxation onto (110), (111) and (112) planes are calculated and shown in Fig.11 (a), (b) and (c) respectively. The projected positions of atoms are represented by circles, triangles and quadrangles according to the differences in the atom positions along the direction of projection, in which shaded ones correspond to core

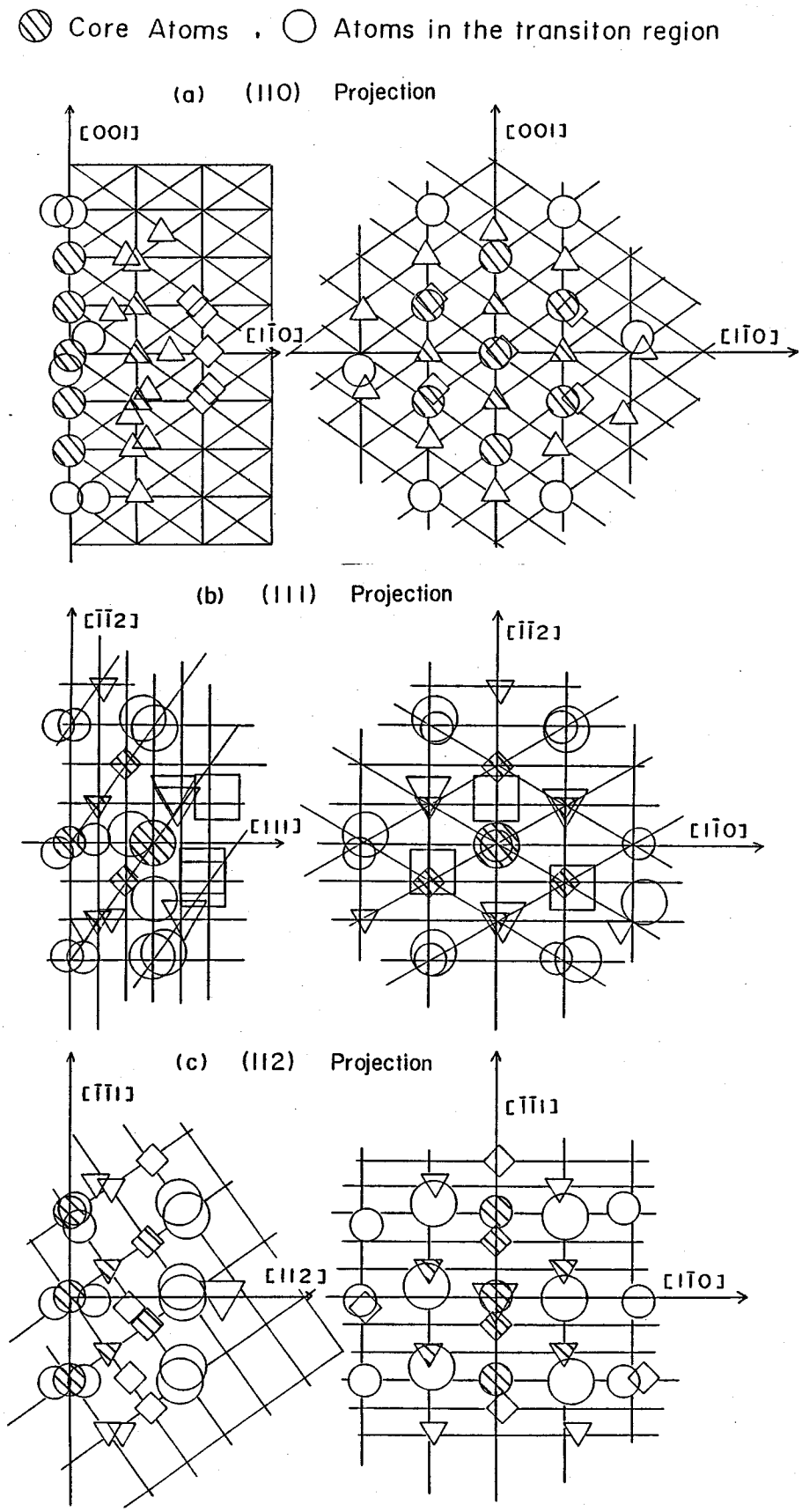

Fig. 11 The projected positions of half of atoms in a b.c.c. embryo core and its surrounding transition region after the relaxation: (a) on the (110) plane, (b) on the (111) plane, and (c) on the (112) plane. Smaller circles, triangles and quadrangles,and larger ones indicate the differences in atomic positions along the direction of projection, and shaded ones correspond to embryo core atoms.

atoms. It is found in these figures that many atoms in the transition region lie nearly on their original positions before the relaxation, confirming the above mentioned fact. So that, the number of atoms belonging to the embryos is reduced to about a half of that before the relaxation. The ratio between the number of atoms in the embryos and that in the disordered boundary region is about 1:3.7 for the b.c.c. crystalline embryo model and 1:4.5 for the f.c.c. crystalline embryo model.

In order to see the connection of atoms in a b.c.c. embryo and its surrounding disordered region, the distribution of potential energy of each atom and reduced hydrostatic pressure on it are calculated by using the same interatomic potential employed in the relaxation process and are shown in Fig.12 (a) and (b) respectively. The potential energy of the centre atom in the embryo core has almost the same value of large crystal. As the radial distance from the centre atom position is increased, the potential energy of each atom becomes greater with a large dispersion. On the other hand, the reduced hydrostatic pressure on the centre atom of the core is nearly 0 kbar and the pressure on each atom gradually becomes scattered with increasing the radial distance from the centre atom. Kiritani and Hamada[99] calculated the distribution of hydrostatic pressure on each atom in the DRP model structure by using the same potential, and showed that it ranges from -200 kbar to +200 kbar, which agrees with the pressure distribution in the disordered regions in the embryo model. These results indicate that atoms both in the embryo and the disordered boundary region are continuously and smoothly connected.

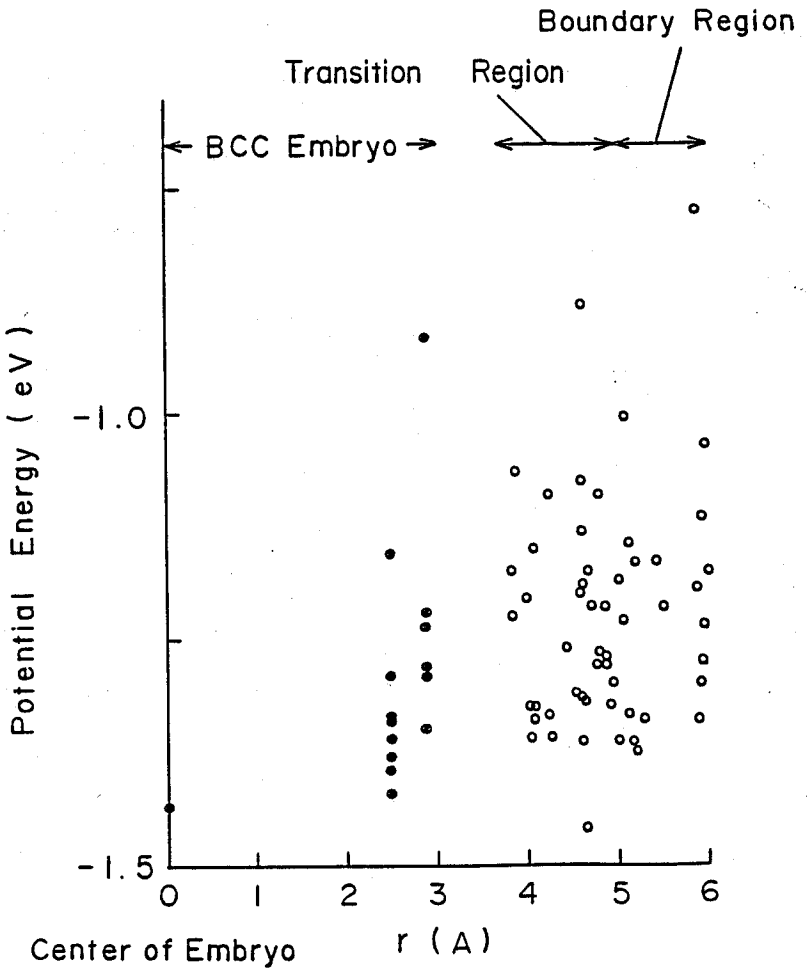

(a)

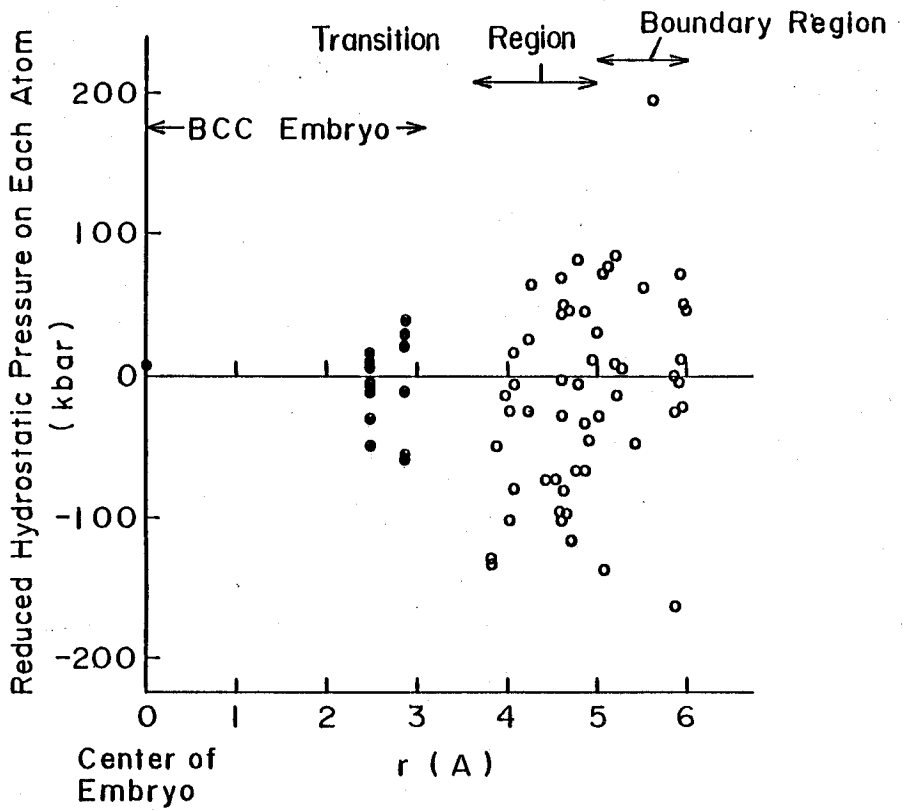

(b)

Fig. 12 Smooth and tight connection between atoms in a b.c.c. embryo and its surrounding disordered region: (a) the distribution of potential energy of each atom, and (b) the distribution of reduced hydrostatic pressure on it.

2.3 Model Construction for Amorphous Fe-B Alloys

Three crystalline embryo models are constructed by computer, simulating the structures of the amorphous $Fe_{100-x}B_x$ alloys (for x = 14, 20 and 25). The algorithm for the simulations is almost the same as that employed for modelling of one-component amorphous structure.

The before mentioned fact that the Mössbauer spectra of amorphous Fe-B alloys were successfully analysed by assuming the b.c.c.-like near neighbour configurations suggests that the basic structure of the embryos in these alloys would be of the b.c.c. cystal form.[26] It is also confirmed that the interference function calculated from the b.c.c. crystalline embryo model is in good agreement with so far obtained experimental ones for various amorphous metals and alloys, as described later. Therefore, in the present models, the b.c.c. structure is chosen for the crystalline embryos. For the case of the amorphous Fe-25at%B alloy, the chemical compound cluster of crystalline Fe_3B type is added in the model as a basic structural unit of the crystalline embryo in accordance with the experimental results.[16,26,27,28]

A schematic view of the crystalline embryo model is given in Fig.13. The embryos of the b.c.c. structure represented by circled regions (A and B) in the figure have a nearly spherical shape, initially containing the same number of atoms of about 60, and have no correlation in orientations with each other. The lattice parameter of the b.c.c. embryo is chosen as 2.8665 A which is the same value as that in the b.c.c. embryo model of single element case. The distance between the centres of neighbouring embryos is taken

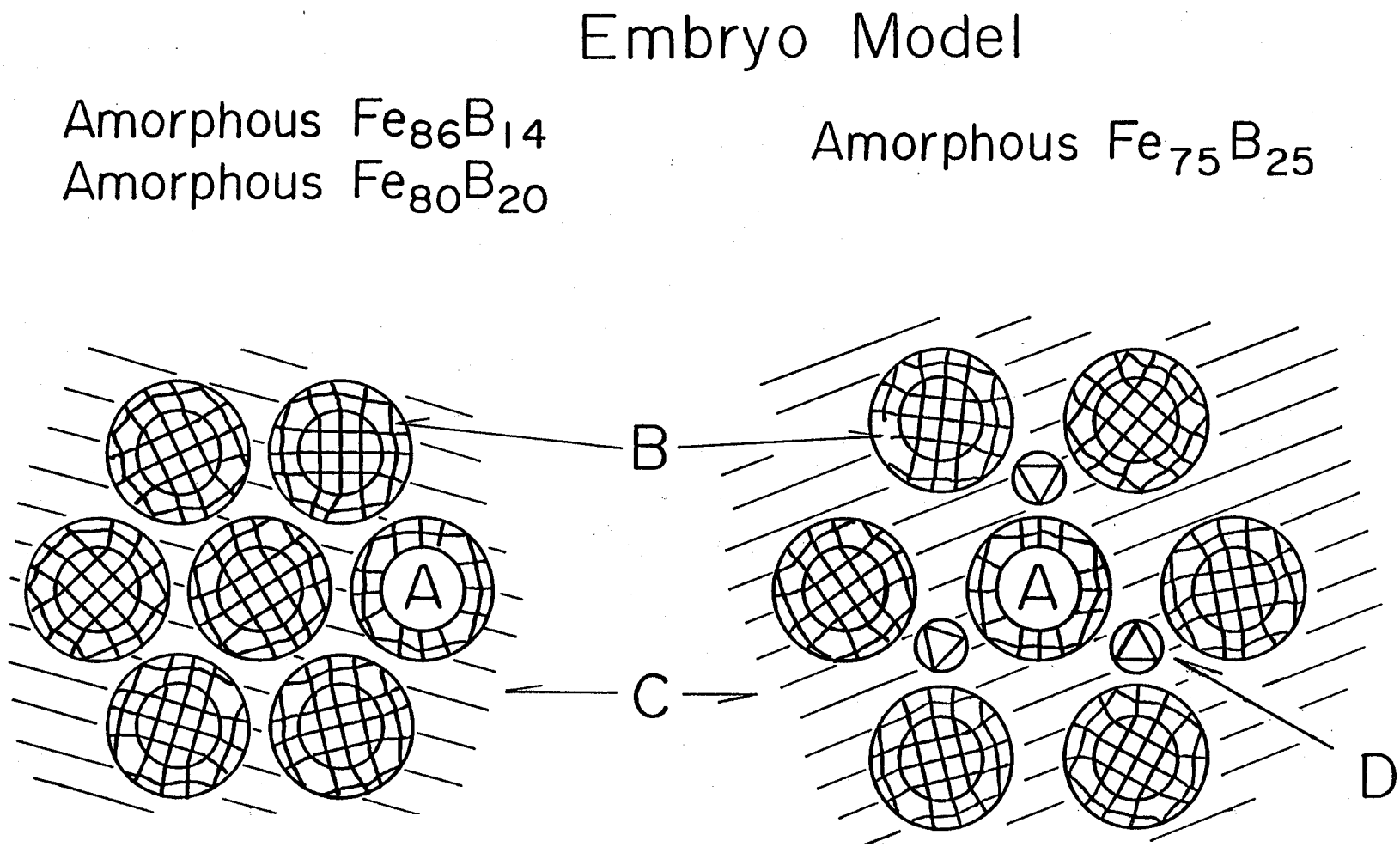

Fig. 13 Schematic view of the crystalline embryo models for amorphous $Fe_{100-x}B_x$ (x=14, 20 and 25) alloys. A: the embryo cores with b.c.c. structure. B: the transition regions of the crystalline embryos. C: the disordered boundary regions. D: the chemical compound clusters of crystalline Fe_3B type.

to be about 16 A. Surrounding each embryo is the disordered boundary regions, which are shaded (C) in the figure. Atoms are distributed densely and randomly according to the computer-generated random coordinates in this regions. For the amorphous $Fe_{75}B_{25}$ alloy, small clusters of trigonal prisms containing six Fe atoms in a nearest neighbour and three further Fe atoms at somewhat larger distances around a centre boron atom are distributed in the disordered boundary regions. These chemical embryos are represented by triangles (D) in the same figure. In the calculations, three-dimensional assemblies composed of about 800 hard spheres of the two different diameters are constructed by computer under the periodic boundary condition. The spheres of different sizes represent the atoms of different types, i.e. iron and boron. Experimental evidences in many other metal-metalloid amorphous alloys have eliminated the possibility of perfectly random distribution of metal and metalloid atoms and showed that metalloid atoms are not in contact. Lamperter et al.[16] also confirmed above mentioned fact in the amorphous $Fe_{80}B_{20}$ alloy. Other computer modelling experiments for amorphous Fe-B alloys also adopted this condition.[65,66] Therefore, in the present model, boron atoms are scattered so as not to contact with each other and embeded interstitially or substitutionally in the outer part of the b.c.c. type embryos (B in Fig.13) and disordered boundary regions. The density of each model is fitted to the experimental value measured by Fukunaga et al.[11]

In order to connect embryos with the disordered boundary regions as smooth as possible, iron and boron atoms both in the outer part of embryos (B in Fig.13) and in the disordered regions (C) are

relaxed by using three kinds of assumed interatomic potentials. In this case, atoms belonging to the inner part of embryos are kept unrelaxed. Otherwise, the embryo cores are not able to retain the b.c.c. structure, since an interatomic potential with a soft core repulsive term as given below is employed. When the harder repulsive term such as of the Lennard-Jones potential is used, the embryos are more persistent. Therefore, the unstable character of the embryo cores exhibited in this calculation is presumably not essential. In addition, it is not always clear whether the cohesive energy of the metal-metalloid amorphous alloy is adequately represented by a sum of pair-wise interatomic interactions, which does not take account of directional bonding characters of metal-metalloid and metal-metal pairs. Nevertheless, computer modelling experiments suggest that any energy minimization algorithm may produce a dense and isotropic arrangement of atoms, despite the relatively large diversity in the choice of force constants. In the case of the model construction for the amorphous iron, the Pak-Doyama potential[97] for α-iron, of which the repulsive part is relatively soft compared with that of the Lennard-Jones 6-12 power potential, is employed, leading to variability in the near-neighbour atomic distances which could remove to a considerable extent the difficulty in the dense packing of atoms. Therefore, a modified Morse-type pair potential, which is as soft as the Pak-Doyama potential and has been used by Heimendahl[50] and Fujiwara et al.,[67] is employed as follows.

$$\phi(r) = \varepsilon\{\exp(-2\alpha(r-r_0)) - 2\exp(-\alpha(r-r_0))\}\cdot T(z), \qquad (5)$$

$$\text{with} \quad T(z) = \begin{cases} 1 & z < 0 \\ -z^4 + 4z^3 - 4z^2 + 1 & 0 \leq z \leq 1 \\ 0 & z > 1 \end{cases} \tag{6}$$

where $Z=(r-r_0)/(r_c-r_0)$, $\alpha=1.69$ and $r_c/r_0=1.34$. The value of r_c/r_0 is rather arbitrary and adjusted to that of the Pak-Doyama potential used in the previous calculation. The truncation function T(z) satisfies the requirement that the potential and its first derivative continuously vanish at the truncation point r_c. Thus obtained truncated Morse-type potential $\phi(r)$ becomes quite similar to the Pak-Doyama potential by choosing appropriate values of the position r_0 and the depth of potential minimum ε. The parameters for the interatomic potentials used to describe the amorphous Fe-B alloys are determined as follows. The x-ray scattering is generally dominated by the contribution from the heavier metallic elements. It is considered that the first peak position in the pair correlation function corresponds to the position of the Fe-Fe interaction potential minimum. According to the results by Fukunaga et al.,[11] $r_{0_{Fe-Fe}}$ is set at 2.57 A for the model of the amorphous $Fe_{86}B_{14}$ alloy and for that of amorphous $Fe_{80}B_{20}$ and $Fe_{75}B_{25}$ alloys is at 2.58 A. Other two parameters, $r_{0_{Fe-B}}$ and $r_{0_{B-B}}$, are taken from the crystal structure data on the Fe_3B as 2.05 A and 3.14 A respectively. The latter indicates the absence of nearest-neighbour B-B correlations. Lamperter et al.[16] showed that the nearest-neighbour distance for the Fe-B pair in the amorphous $Fe_{80}B_{20}$ alloy is 2.14 A. We also calculated the interference and pair correlation function using this value and compared them with those in the case of the average Fe-B spacing of 2.05 A. The results of

the calculations employing the two different parameters will be compared later. The depth of the potential minimum for the Fe-Fe pair, ε_{Fe-Fe}, is 0.51 eV, which was derived from the cohesive energy of α-iron (Fujiwara et al.[66]). The interaction strengths for the Fe-B pair and the B-B pair are more complicated. Boudreaux[65] argued the effect of the choice of these parameters and conluded that the metal-metalloid interaction strength should be greater than that of the metal-metal interaction, which satisfies chemical requirements. In the present studies, several runs of computation have been tried to clarify the effect of these parameters on the pair correlation functions and ε_{Fe-B} and ε_{B-B} are finally determined to be 0.55 eV and 0.05 eV respectively. Thus obtained truncated Morse-type pair potentials are shown in Fig.14.

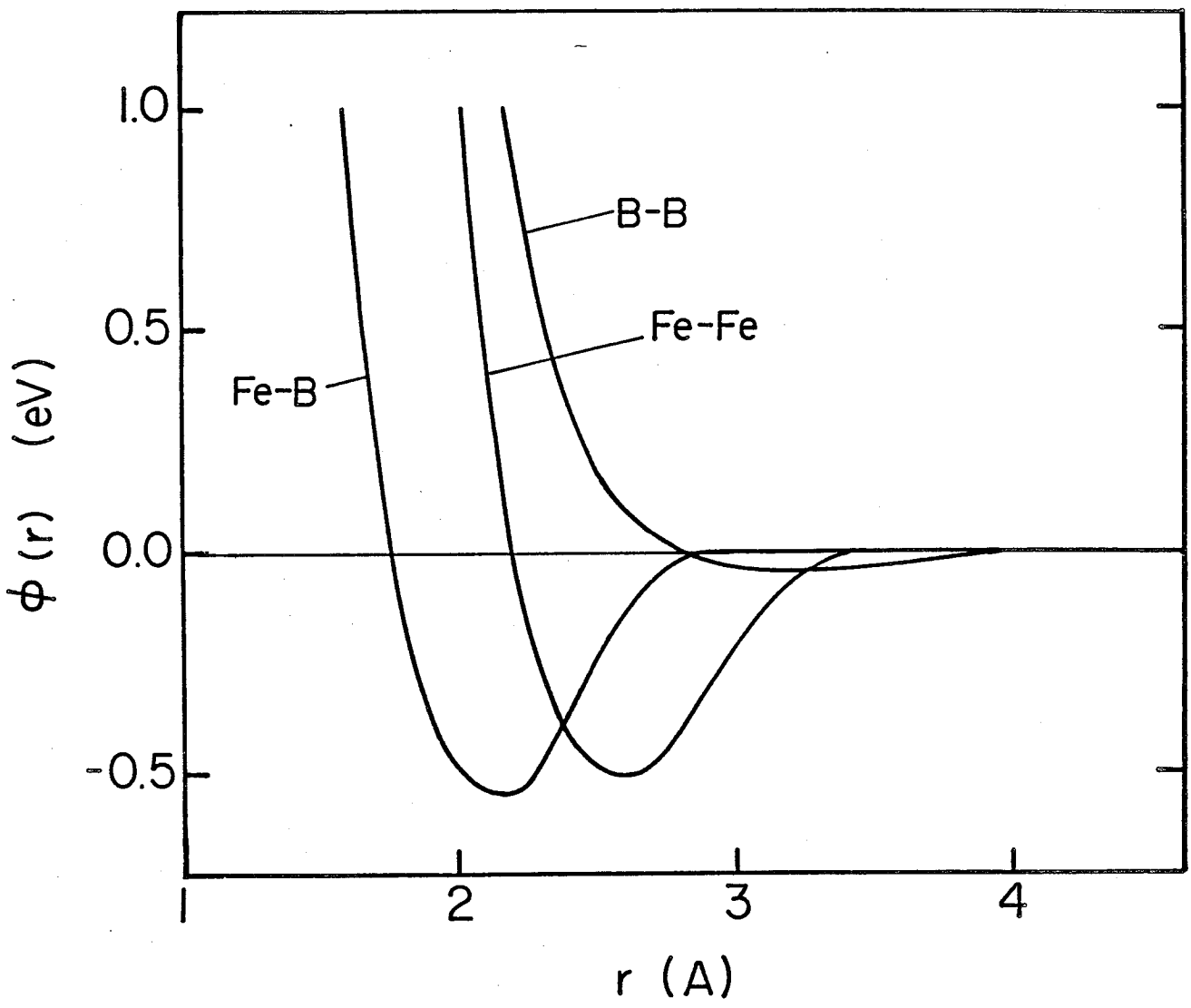

Fig. 14 Modified Morse-type interatomic potentials for Fe-Fe, Fe-B and B-B pairs employed in the model construction.

2.4 Model Structure for the Calculation of High Resolution Electron Images

The axial bright-field images are calculated for the crystalline embryo model of the amorphous $Fe_{86}B_{14}$ alloy, of which the schematic view is given in Fig.15. The embryo cores with the b.c.c. structure represented by circled regions (A) have no correlation in orientations with each other. Surrounding each embryo is the disordered regions (C), which is shaded in the figure. Atoms are distributed densely and randomly according to the computer-generated random coordinates in this regions. In order to connect embryo cores with the disordered regions as smooth as possible, iron and boron atoms both in the outer part of embryos (B) and in the disordered regions (C) are relaxed by using three kinds of the Morse-type interatomic potentials. Therefore, the atomic positions of the outer part of embryos more or less deviate from those of the b.c.c. structure. The mean distance between the centres of neighbouring embryos is about 16 A. The b.c.c. embryo cores (A) do not contain boron atoms and their lattice parameter is 2.8665 A corresponding to that of α-iron. The S(K) and the G(r) of the model structure well reproduce the diffraction experiment as described in the next chapter, when the number of iron atoms belonging to the embryo core is taken as 15. The cluster of this size contains the first and the second b.c.c. neighbour shell for the central iron atom. The model assembly used in the image contrast calculation is a sphere of 20 A in diameter in which a single b.c.c. embryo is placed in the centre. This embryo together with its outer part is expected to contribute to the lattice image when it is near the

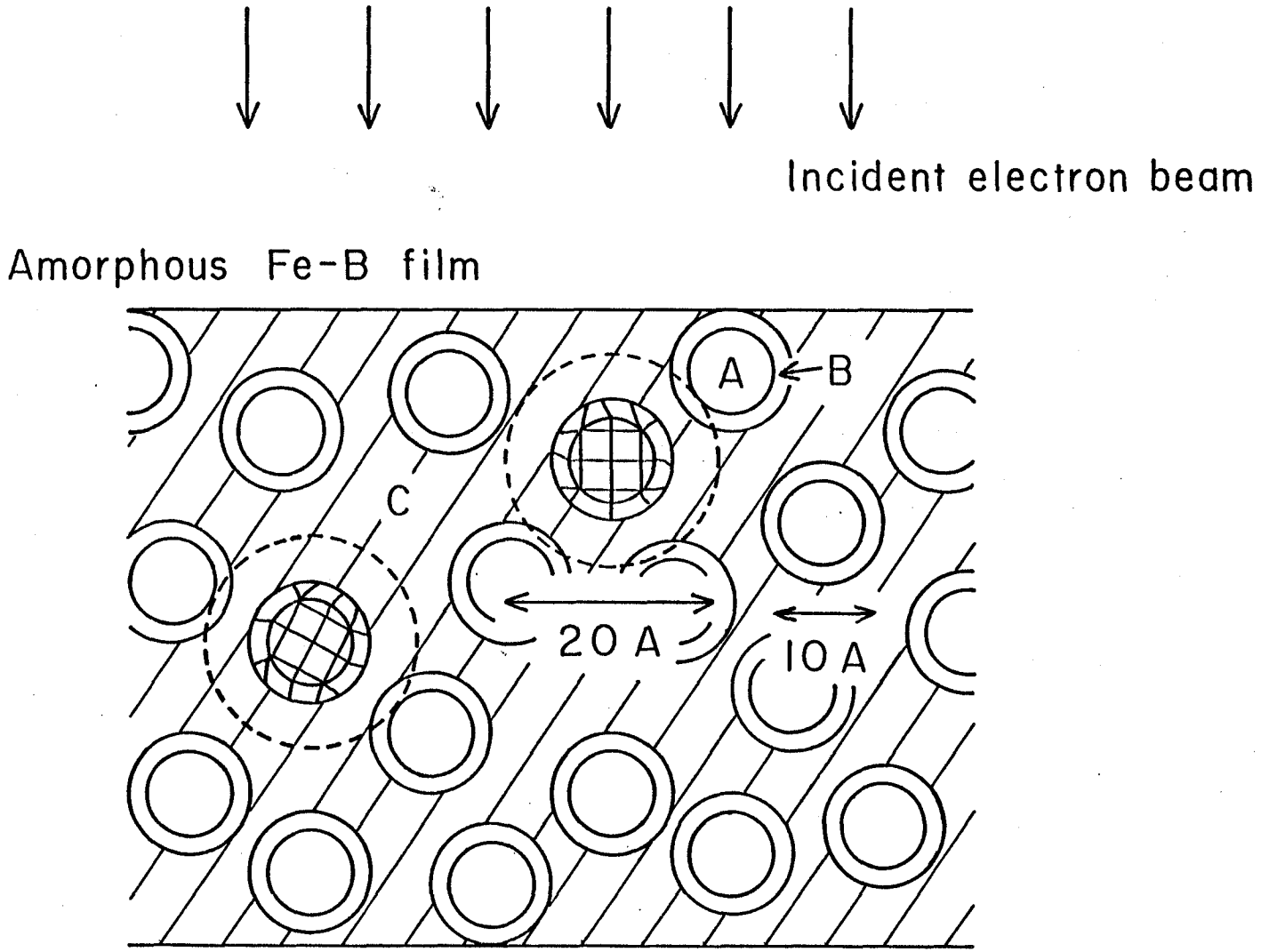

Fig. 15 Schematic view of the crystalline embryo model for the amorphous Fe-B alloy. The symbols, A, B and C, just correspond to those in Fig.10 and Fig.13. The model assembly used in the image contrast calculation is a sphere of 20 A in diameter, which is represented in the figure by broken lines.

Bragg position. Furthermore, in order to examine the overlap effects between two crystalline embryos and the change of the lattice image with the thickness increase of the specimen, the calculation is done on two different spherical assemblies stacked one over the other. Since the atomic scattering factor of boron atoms is relatively small as compared with that of iron atoms, the contribution of boron to the image formation is neglected. Accordingly, the calculations are carried on the scattering by about 330 iron atoms in a spherical aggregate and about 660 iron atoms in two spherical ones.

For the purpose of comparison with the embryo model, calculations are also made on the DRP model, in which iron and boron atoms are distributed at random in the overall volume according to the computer-generated random coordinates, provided that the probability of boron-boron neighbouring is excluded, until the system has the same composition and the density as the embryo model. Then, the atoms are relaxed by using the same interatomic potentials as in the embryo model. The DRP model thus obtained is quite similar to those employed by other investigators to explain the diffraction functions, S(K) and G(r), of amorphous alloys.

3. CALCULATION OF X-RAY DIFFRACTION FROM EMBRYO MODEL

In the last chapter, model assemblies of single element for the amorphous iron and nickel and, as a more realistic structural model, model aggregates for the amorphous Fe-B alloys are constructed by computer based on the concept of crystalline embryos. These model assemblies contain both the crystalline embryos and the disordered regions coexisting and continuously connected each other. In this chapter, the interference function and the pair correlation function of these embryo models are calculated and compared with the experiments.

In the single element case, the analysis of the crystalline embryo model gives that the embryos and their surrounding and attaching atoms which form the disordered boundary region can play essential roles to reproduce the characteristic diffraction functions of amorphous metals and alloys. However, without the metalloid atom, the packing structure of the disordered regions is not necessarily realistic and the crystalline periodicity in the embryo is stronger than that expected from the real structure, giving rise to disagreements in the peak profiles, ratios and positions in the diffraction functions with the experiments. On the other hand, in the x-ray diffraction measurements, the magnitude of the scattering vector, K, is inevitably limited at around 17 A^{-1} in the reciprocal space, which brings about a poor resolution of the G(r) function. Therefore, the effect of the truncation of the S(K) function on the G(r) function is examined. Then, by taking account of the effect of truncation and applying a new correction method, two diffraction functions are recalculated from the computer models for amorphous

Fe-B alloys based on the concept of the medium range order rising from crystalline embryos. Finally, it is concluded that two functions are in good agreement with the experiments, when the embryo size is taken to be as small as 10 A in diameter, which corresponds to some twenty atoms cluster including a part of the transition region.

3.1 Deduction of S(K) and G(r) Functions

After the construction of the amorphous structure based on the concept of crystalline embryos as mentioned before, the pair correlation function and its Fourier transform, i.e. the interference function, are calculated. Using the radial distribution function of atoms as a function of the radial distance r, RDF(r), the pair correlation function is written in the form,

$$G(r) = RDF(r)/4\pi r^2\rho_0, \tag{7}$$

where ρ_0 is the number density of atoms in the model structure.

The relation between the pair correlation function for a macroscopically isotropic material containing atoms of only one chemical species and the coherent x-ray scattering by such a material was derived by Zernike and Prins[100] and has been discussed subsequently by many authors. The coherently scattered intensity from N identical atoms in an irradiated volume can be expressed in the Fraunhofer approximation in terms of $\mathbf{K} = \mathbf{k}' - \mathbf{k}$ as

$$\begin{aligned} I(\mathbf{K}) &= \sum_j \sum_l f_j(K) f_l^*(K) \exp(-i\mathbf{K}\cdot(\mathbf{r}_l - \mathbf{r}_j)) \\ &= Nf(K)f^*(K) + \sum_j \sum_{l\neq j} f_j(K) f_l^*(K) \exp(-i\mathbf{K}\cdot(\mathbf{r}_l - \mathbf{r}_j)), \end{aligned} \tag{8}$$

where $\mathbf{k}$ and $\mathbf{k}'$ are the incident and scattered wave vectors, $\mathbf{K}$ the scattering vector, f(K) the x-ray atomic scattering factor for the atomic species being considered, $\mathbf{r}_j$ the position of the jth atom, and the summation is over all atom pairs in it. This $I(\mathbf{K})$ does not include the x-ray intensity incoherently scattered in Compton process and neglects the multiple scattering effects.

It is usually assumed that the amorphous structure is macroscopically homogeneous and isotropic, and described by the pair correlation function G(r) which depends only on $r = |\mathbf{r}_1 - \mathbf{r}_j|$. Omitting the zero angle scattering, which occurs at extremely small angle for an irradiated volume of macroscopic size, the equation (8) can be rewritten in the form by using the G(r),

$$I(K) = N|f(K)|^2(1 + 4\pi\rho_0\int_0^\infty r^2(G(r)-1)\frac{\sin(Kr)}{Kr}dr). \qquad (9)$$

The interference function S(K) is defined as

$$S(K) = \frac{I(K)}{N|f(K)|^2}$$

$$= 1 + 4\pi\rho_0\int_0^\infty r^2(G(r)-1)\frac{\sin(Kr)}{Kr}dr. \qquad (10)$$

This is essentially the same as Eq.(1) and employed as the basic formula for the computer calculation of the crystalline embryo model as well as other models.

In a binary alloy, the total pair correlation function G(r) and the total interference function S(K) are expressed using the partial pair correlation function $G_{ij}(r)$ and the partial interference function $S_{ij}(K)$ respectively as follows,

$$G(r) = w_{ii}G_{ii}(r) + w_{jj}G_{jj}(r) + 2w_{ij}G_{ij}(r) \qquad (11)$$

and

$$S(K) = w_{ii}S_{ii}(K) + w_{jj}S_{jj}(K) + 2w_{ij}S_{ij}(K) \qquad (12)$$

with

$$w_{ij} = x_i x_j f_i f_j / \left(\sum_k x_k f_k\right)^2, \tag{13}$$

where x_i and f_i are respectively the atomic fraction and the x-ray atomic scattering factor for an atom of type i. In the present simulation, the K dependence of the weighing factor w_{ij} is ignored but, instead, the averaged value of each w_{ij} over the range of K from 0 to 10 A^{-1} is used in Eqs. (11) and (12). For instance, in the calculation of the model of the amorphous $Fe_{75}B_{25}$ alloy, the weighing factor w_{FeFe} is given as 0.883 and the corresponding factor for the Fe-B correlation is taken as about eight times smaller than that.

3.2 S(K) and G(r) Functions of Embryo Model of Single Element

The pair correlation function for b.c.c. crystalline embryo model is shown in Fig.16(a). The lattice parameter of b.c.c. structure of the embryo is the same as the value used in Fig.9. In this model calculation, outer 36 atoms of each embryo containing 51 atoms are relaxed with the surronding boundary atoms by using the Pak-Doyama potential. Accordingly, each embryo core retaining the b.c.c. structure consists of only 15 iron atoms. The calculated G(r) function does not always fit the curves obtained from the diffraction data as regards the shape of the second peak. In this respect, as mentioned in the subsection 1.2.1, Waseda and Chen[21] showed that the G(r) functions of amorphous Fe-B alloys with boron content below 20 at% had the "reversed" second peak splitting in spite of the "normal" splitting in the second halo peak in the S(K) functions. On the other hand, the S(K) function derived from the G(r) function, which is shown in Fig.17(a), well agrees with so far obtained experimental curves of various amorphous metals and alloys, although relative positions and intensities of halo peaks are still slightly different from experimental ones. It is worthy of noting that the shoulder on the high angle side of the second halo peak in the S(K) function, which does not appear in the case of an isolated b.c.c. microcrystallite as in Fig.9(a), is clearly seen. In order to find the effect of local environments on the conformation of the S(K) function, embryo core atoms, the atoms in the transition regions and the disordered boundary atoms in the vicinity of the embryos are taken as the centres and the radial distribution around them is examined. In this case, the transition region is

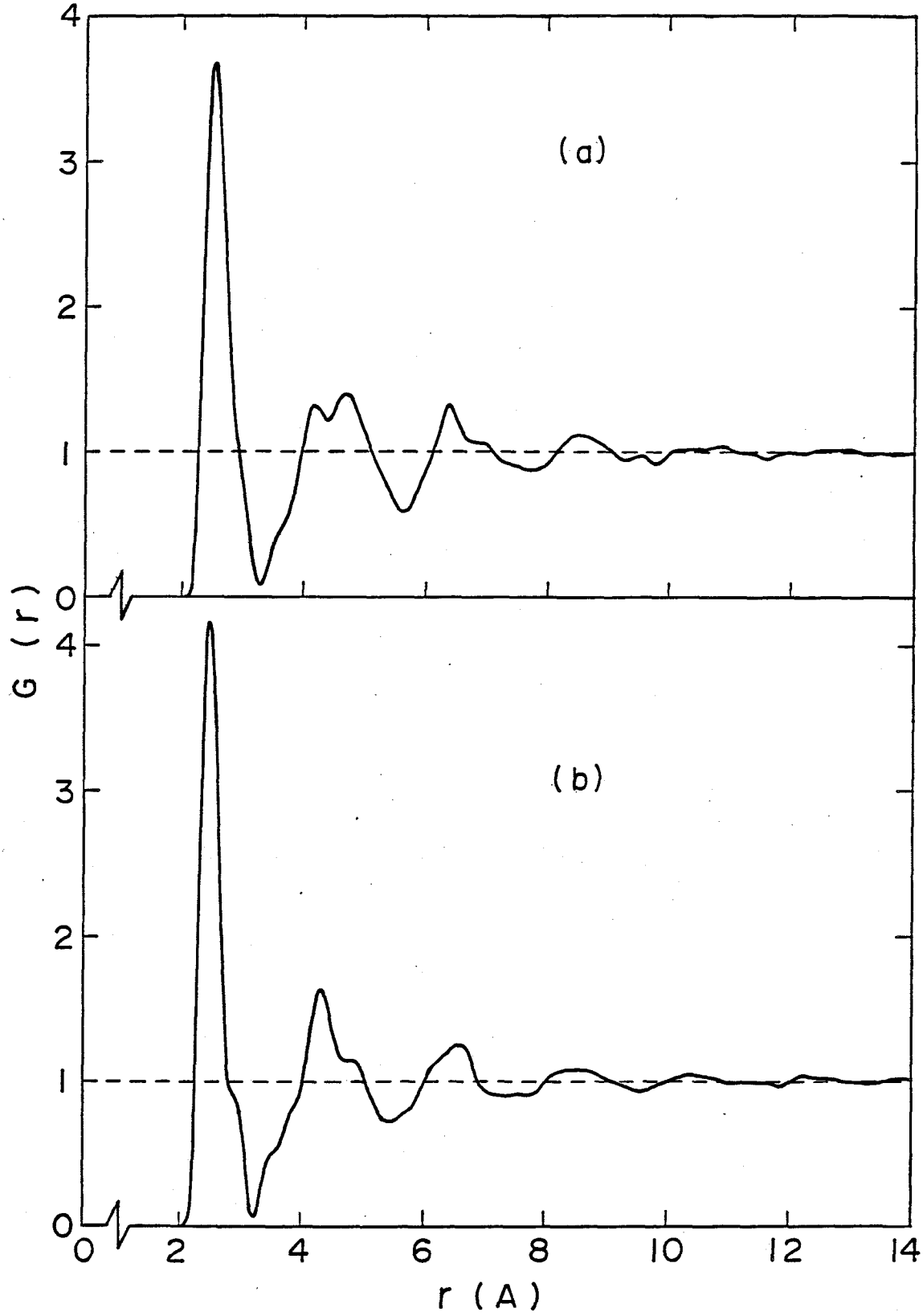

Fig. 16 The G(r) functions of the crystalline embryo model: (a) the b.c.c. embryo model, the lattice parameter of b.c.c. structure is the same as that used in Fig.9; (b) the f.c.c. embryo model, the lattice parameter of embryos is taken as 3.5241 A corresponding to that of nickel at 20°C.

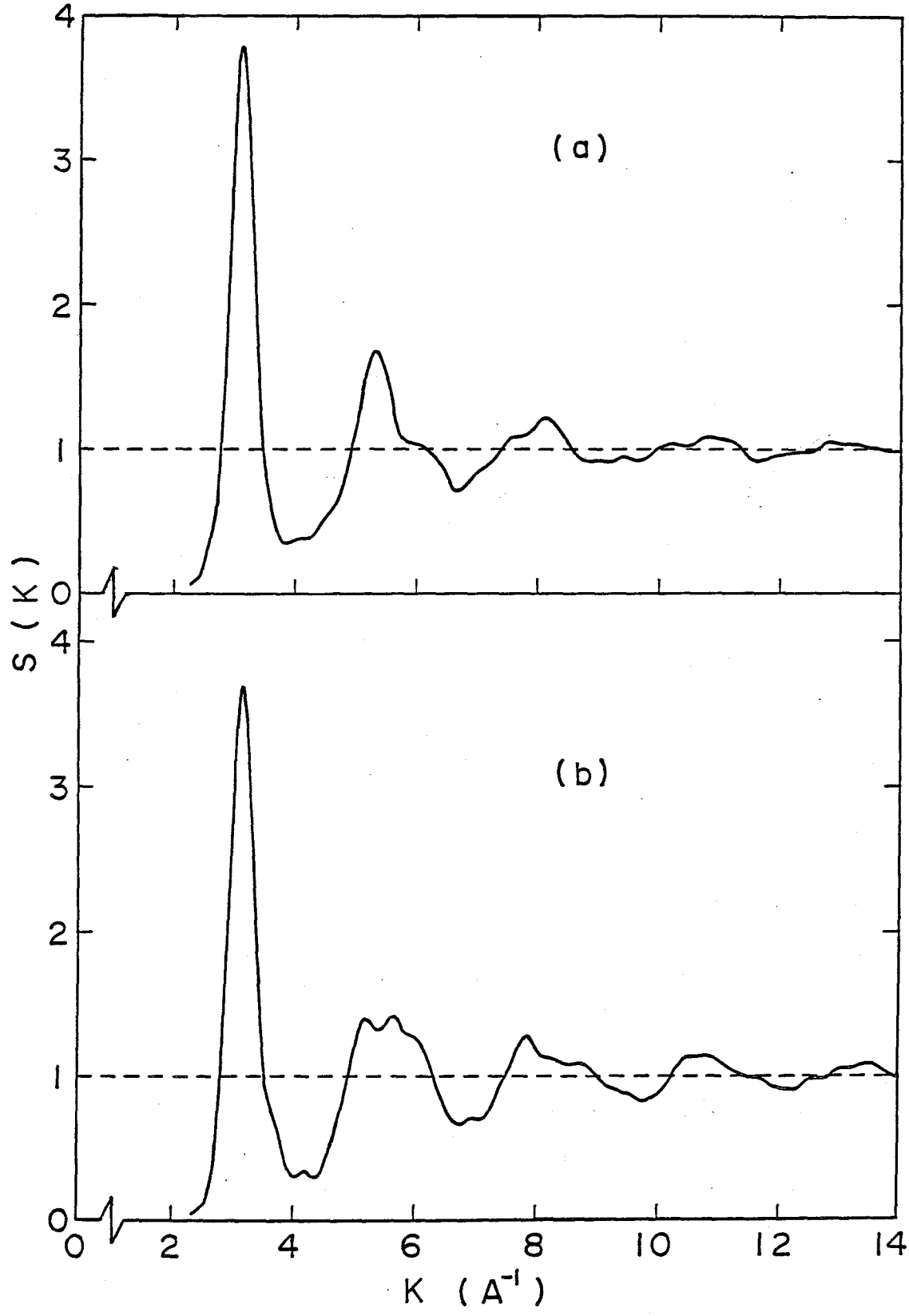

Fig. 17 The S(K) functions calculated from the G(r) functions in Fig.16: (a) the b.c.c. embryo model, and (b) the f.c.c. embryo model.

divided into two parts, i.e. inner and outer ones, the former being closer to the core than the latter, by taking account of the fact that the displacements from the initial positions of atoms after the relaxation is much less in the former than in the latter. The partial G(r) functions calculated from partial RDF's are, then, Fourier transformed to obtain the S(K) functions, which are shown in Fig.18(a), (b), (c) and (d) respectively. The partial S(K)'s given in (b), (c) and (d) of the figure exhibit the characteristic features of diffraction intensity distribution of amorphous metals, especially the splitting of the second halo peak. The profiles of the second halo peaks in the above S(K)'s give the better agreement with the experimental ones than that in Fig.17(a), and this suggests that the shoulder of the second halo peak arises from the interference between the atoms in the embryos and those in the disordered boundary regions. On the other hand, the first halo peak in Fig. 18(d) is lower than that in Fig.17(a), suggesting that a degree of atomic order higher than that existing in the simple dense random packing structure in the boundary regions is necessary to reproduce the experimentally obtained values of the peak height of the first halo peak. Actually, when the atoms in the embryo cores are extracted and subjected to the same procedure as in the above, the S(K) function given in Fig.18(a) shows the first halo peak sharp enough to be compared with the experimental data, but, instead, no splitting is observed in the second halo peak, as expected in the case of simple isolated microcrystalline model. The above result not only emphasizes that the microcrystalline diffraction theory, which does not take the boundary layer atoms into account, is

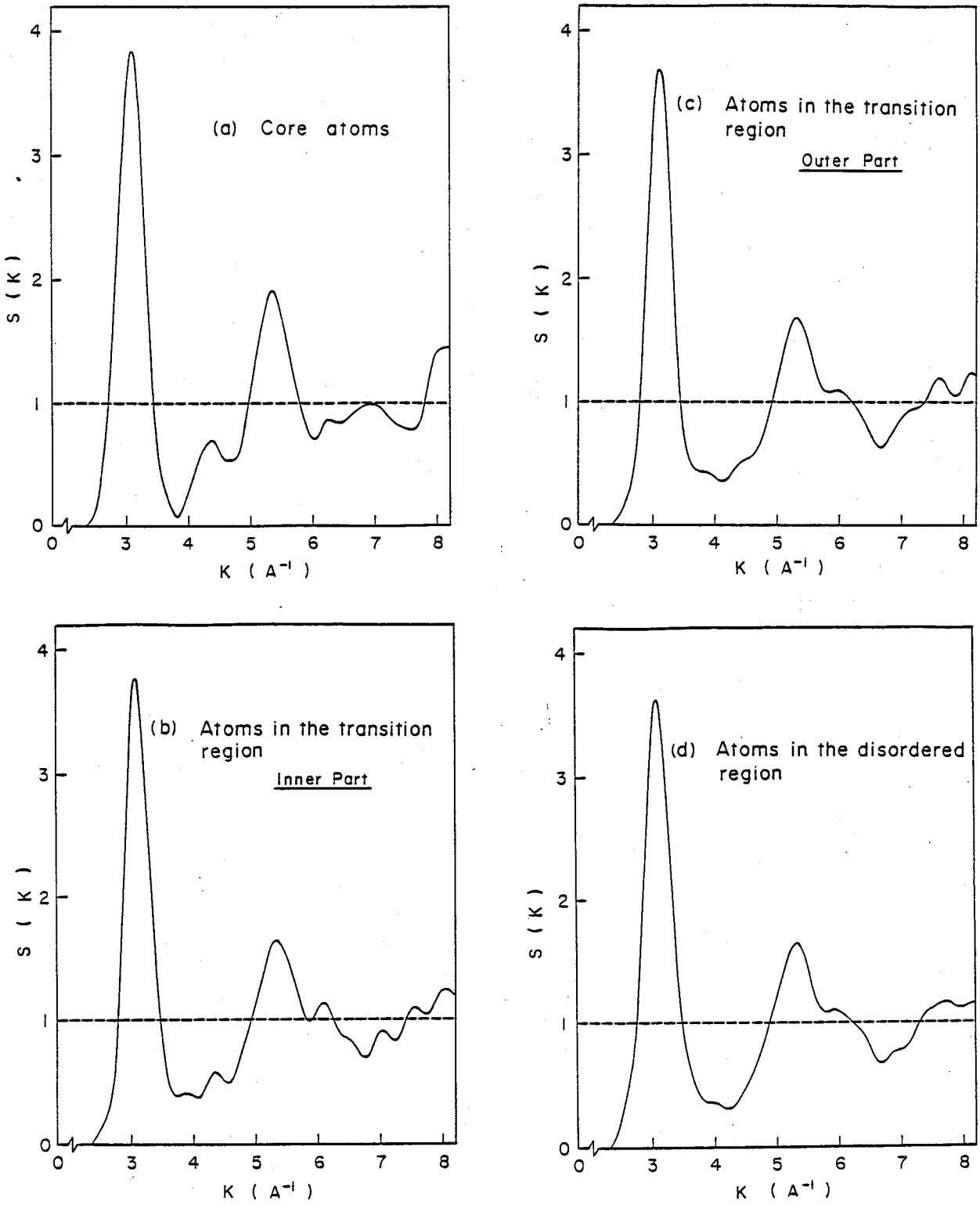

Fig. 18 The S(K) functions of the b.c.c. embryo model calculated from the partial G(r) functions, which takes into account of the radial distributions around atoms: (a) in the embryo cores, (b) in the inner parts of the transition regions, (c) in the outer parts of the transition regions, and (d) in the disordered regions.

not applicable to the amorphous materials, but also strongly suggests that the boundary layers, which intervene between and connect the neighbouring embryos, play important roles in the diffraction phenomena, especially affecting the second halo peak of the interference function.

In the dislocation model of amorphous structure by Koizumi and Ninomiya,[86] the height and the full width at half maximum of the first halo peak of the interference function agree with the experimental results. In the present model, there is no correlations in orientations between the embryos and neighbouring embryos are linked together through the atoms in the disordered boundary regions. Although the fundamental concept and assumptions of the embryo model structure are different from those of the dislocation model, the height and the full width at half maximum of the first halo peak in the former are nearly the same as those in the latter. This agreement between the two models probably arises from the lattice periodicity kept in the confined regions with a certain volume, which are no other than the lattice domains separated by dislocations in the dislocation model and yet are the core parts of the embryos in the present model.

The effect of the basic structure on the diffraction phenomena in the present model is readily seen in Fig.16(b), in which the G(r) function for the f.c.c. crystalline embryo model is shown. Each embryo contains 55 atoms and its outer 36 atoms are relaxed together with the boundary atoms. Each embryo core with the f.c.c. structure consists of 19 nickel atoms. The lattice parameter of f.c.c. structure of the embryos is taken as 3.5241 A corresponding

to nickel at 20°C. Other conditions for calculation are the same as the before mentioned b.c.c. case. Although the correlation function is in fairly good agreement with that calculated from the experimental data, the considerably high first peak suggests that the f.c.c. crystalline periodicity persistently remains in the model structure after the relaxation. The S(K) function shown in Fig.17(b) does not fit the experimental curves obtained by the x-ray diffraction specially as regards the shape of the second halo peak. In this respect, total G(r) functions with high real-space resolution of the amorphous Pd-Si alloys displayed definitely a second peak splitting into three subpeaks,[10,11] as mentioned the subsection 1.2.1.

Another important factor in the modelling of amorphous structure, which would strongly influence the diffraction phenomena, is introduction of metalloid atoms into the structure. Without the metalloid atoms, the packing structure of the boundary regions would not necessarily be realistic and the crystalline periodicity in the embryos would be stronger than that expected from the real structure, presumably giving rise to disagreements in the peak profiles, ratios, and positions in the correlation function with the experiments. Improvement of the modelling and calculation by taking account of the metalloid atoms are described and discussed in the following sections 3.3 and 3.4.

3.3 Consideration on the Correspondence between Diffraction Pattern and Structural Model

In the neutron diffraction, the nuclear scattering amplitude and the incoherent scattering contribution to the total intensity distribution are constant even for the scattering vector larger than 20 A^{-1}. Suzuki et al.[10] obtained the interference functions and the corresponding radial distribution functions and pair correlation functions for several amorphous Pd-Si alloys by means of the time-of-flight neutron technique. Scattering was measured over a wide range of K values up to 30 A^{-1}, and a well resolved pair correlation function showing a distinct separation between two first neighbour peaks, which are associated with Pd-Si and Pd-Pd distance respectively, was obtained. In the case of x-ray diffraction, the atomic scattering factor is remarkably reduced and the incoherent contribution to the scattered intensity, i.e. the Compton scattering, becomes greater, as the K value is increased. Accordingly, even when the most careful precautions are taken in the measurements, x-ray scattering data are restricted to relatively small scattering angles ($K_{max} = 15 \sim 17$ A^{-1}), so that the resolution in the real-space data is poor as a result of termination ripples and broadening. Using the interference function S(K) derived from the measured diffraction intensity distribution, the pair correlation function G(r) is given in the form,

$$G(r) = 1 + \frac{1}{2\pi^2 r \rho_0} \int_0^{K_{max}} K(S(K)-1)\sin(Kr)dK. \qquad (14)$$

where K_{max} is the truncation value of the scattering vector. When K_{max} is infinite, the Eq.(14) is exactly an inverse Fourier transform of Eq.(10). However, in the actual experimental analyses, the K_{max} truncation is unavoidable as mentioned before, and the obtained pair correlation function strongly depends upon its value as the following example shows. In Fig.19, the original pair correlations calculated from the crystalline embryo model of the amorphous $Fe_{86}B_{14}$ alloy using Eq.(7) are shown by small dots. Some characteristic peaks below 5 A corresponding to the b.c.c. structure of the embryos are seen, but over raidal distances greater than 15 A, the pair correlations become almost unity with negligibly small fluctuations, indicating the absence of appreciable spatial variations of the number density of atoms. Accordingly, the intensity distribution in reciprocal space calculated by using Eq. (10) over a range from r=0 to r=15 A may satisfactorily describes the interference function of the model structure, which will be shown later in this section. In order to clarify the effect of termination, the pair correlation functions obtained by truncating the Fourier transformation at two different values of K_{max} in Eq. (14) are shown in the same figure. In the case of $K_{max} = 30\ A^{-1}$, the original pair correlations are approximately followed, as dashed line shows. Especially an asymmetry appears in the first maximum with a shallow hump at about 2.87 A corresponding to the second nearest neighbour distance in the b.c.c. structure. Some small humps on the second peak also arise from the b.c.c. structure of the embryos, as readily identified from the original pair correlation data represented by the dots. When the truncation is done at

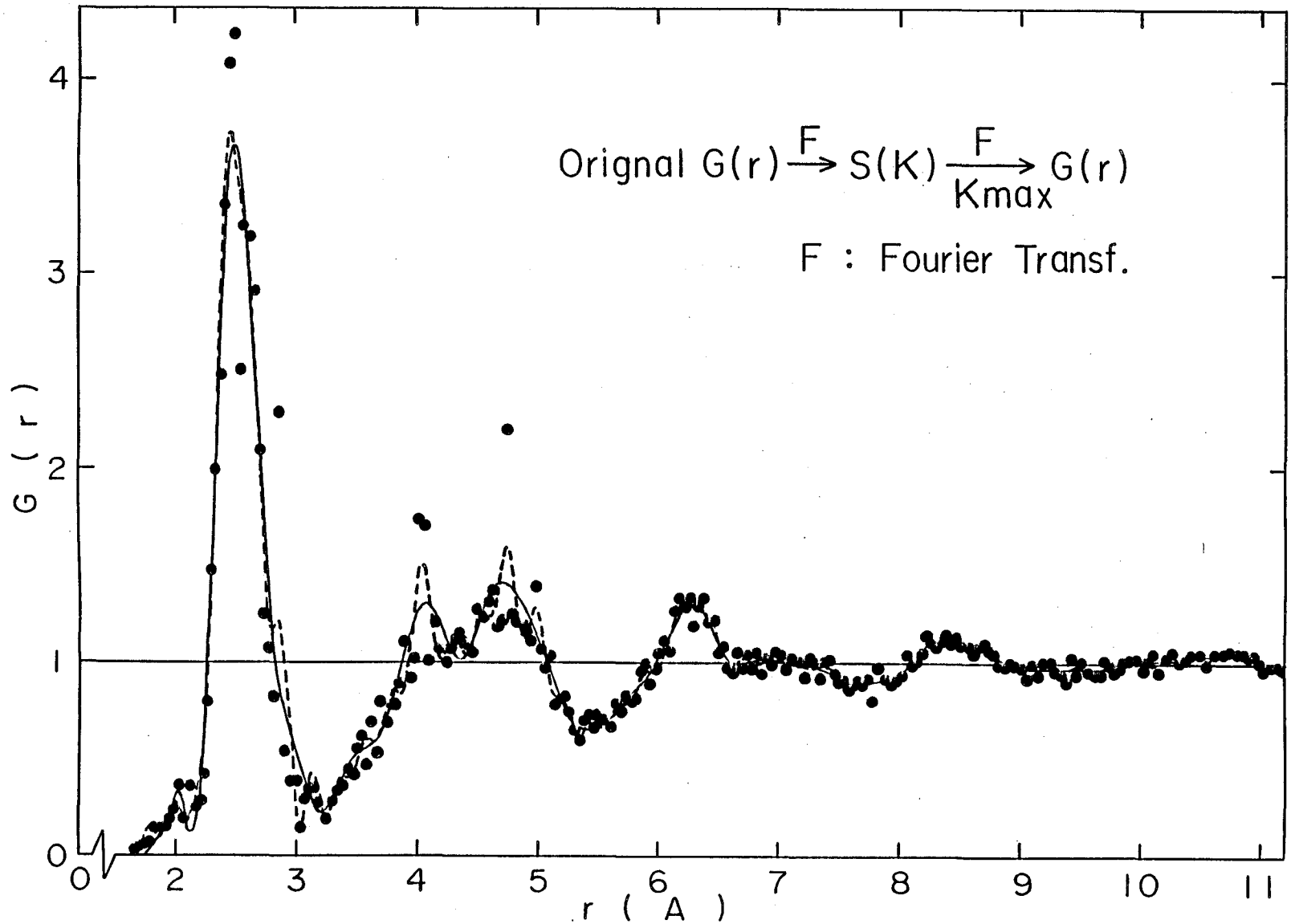

Fig. 19 The G(r) functions calculated for the amorphous $Fe_{86}B_{14}$ alloy. The small dots show the original G(r), and full and broken curves show the G(r)'s obtained by iteration through the S(K) function with the K_{max}=15 A^{-1} and 30 A^{-1} respectively.

$K_{max} = 15\ A^{-1}$, the fine structures in the line profile for $K_{max} = 30\ A^{-1}$ disappear with slight reductions of the first and the second peak height, although the basic features of the curve is preserved, as the full line in the figure shows. The single first peak in this case has a large tail extending toward $r \approx 3.2$ A, enveloping the above mentioned 2.87 A suppeak, and the second peak exhibits two components, of which the outer one at $r \approx 4.7$ A has a greater amplitude than the inner one at 4.1 A. These features are quite similar to those already found in the previous calculation for the b.c.c. embryo model of single element corresponding to the hypothetical amorphous structure of pure iron. Noteworthy are the shape of the second peak and a small hump at $r \approx 2.05$ A: The former presents the "reversed" peak splitting in accordance with the experimental result by Waseda and Chen,[21] and the latter arises from the Fe-B correlations. Suzuki et al.[10] confirmed that the resolution of the pair correlation function is progressively improved by increasing the K_{max} value in the Fourier transformation of the interference function experimentally obtained for the amorphous Pd-Si alloys. For example, when the truncation was made at $K_{max} = 25\ A^{-1}$, the radial distribution function had the second peak split into three suppeaks in contrast to two suppeaks for $K_{max} = 10\ A^{-1}$, which is shown in Fig.2. The above examples of the theoretical calculation for an amorphous Fe-B alloy and the experimental analysis for an amorphous Pd-Si alloy clearly indicate that the truncation in the Fourier transformation of interference function severely controls the quality and spatial resolution of the correlation function and, therefore, to compare a G(r) experimentally

obtained by the truncated Fourier transformation with a small K_{max}, shch as 15 A^{-1}, with a model G(r) is sometimes inadequate. This means that the plausibility of the model is not always guaranteed by the direct comparison between the experimentally obtained G(r) and the model G(r) which is not subjected to the truncation effect.

In order to make the more reasonable comparison with the experimental data, a new process of Fourier transformations, which takes account of the truncation effect, is applied to the structural model, as illustrated in Fig.20. The process of the left hand side in the diagram shows the normal experimental procedure to obtain the S(K) and G(r) from the diffraction intensity distribution, in which the truncated Fourier transformation, Eq.(14), is operated between S(K) and G(r). In the x-ray diffraction experiments for the amorphous Fe-B alloys, K_{max} is about 15 A^{-1}, as indicated on the left hand side in Fig.20. On the other hand, in the computer modelling experiment, the pair correlation function is derived from the radial distribution function by using Eq.(7). It should be noted that thus obtained pair correlation function does not correspond to the experimental one subjected to the truncation effect as discussed above. It is, therefore, necessary to derive the pair correlation function of the model through the process equivalent to that used in the analysis of the x-ray diffraction data, and the first comparison must be between the two interference functions thus obtained from the experiment and the model with the truncation at 15 A described before. In the second place, then, the truncation at $K_{max} = 15$ A^{-1} must be done in the inverse transformation, Eq.(14), to obtain the pair correlation

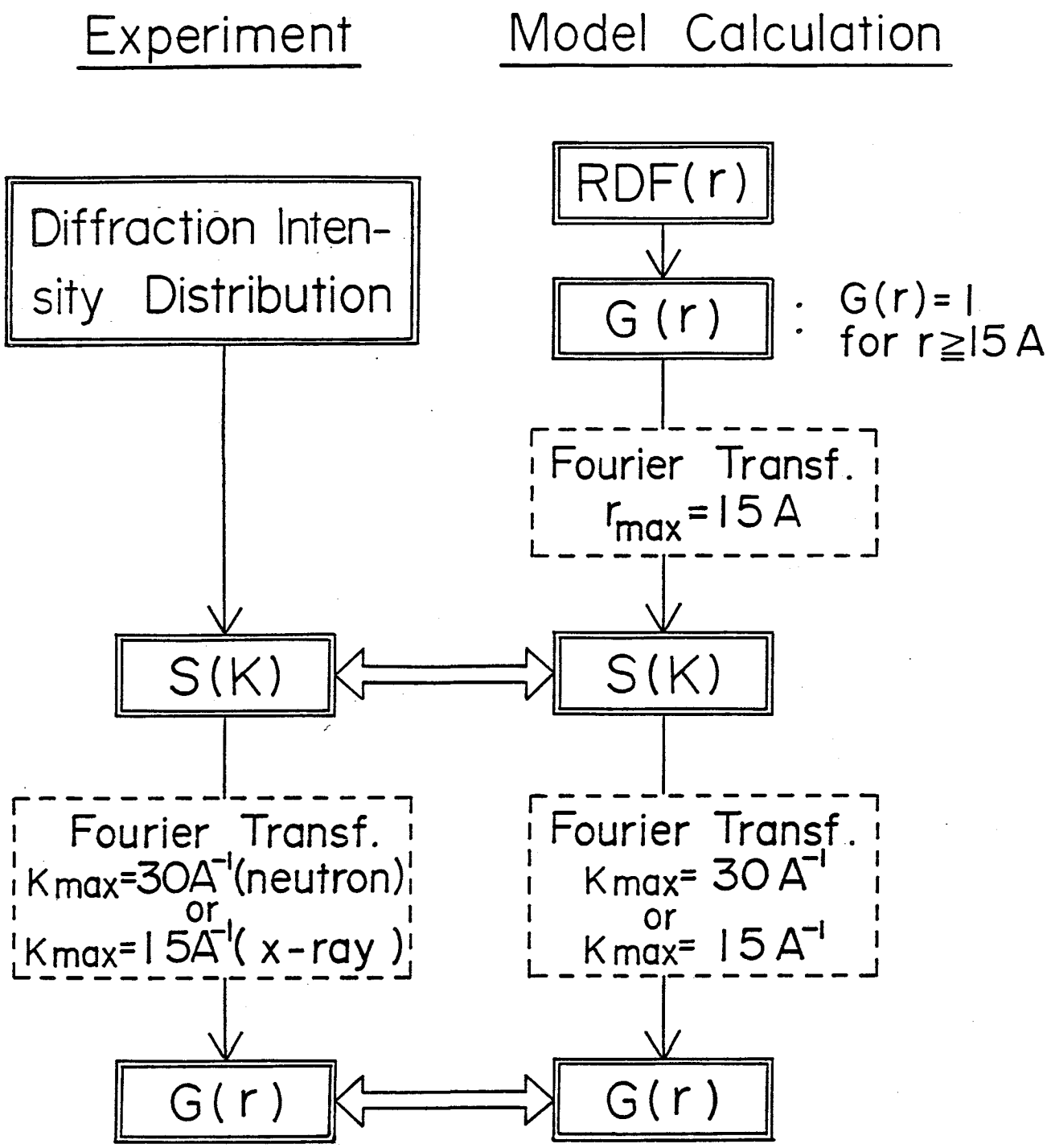

Fig. 20 The diagram of the process of Fourier transformations to obtain the correspondence of G(r) and S(K) between the experiment and the model calculation. On the left hand side is shown the ordinary experimental procedure and on the right hand side is the process of the model calculation.

which can be exactly compared with the experimental one, as illustrated on the right hand side in Fig.20. It is concluded that the above process of iteration of Fourier transformation is necessary for the meaningful comparison between the experimental results and the model calculation. Actually, this method is successfully applied to the crystalline embryo model as will be shown in the following section.

3.4 S(K) and G(r) Functions of Embryo Model for Amorphous Fe-B Alloys

Three kinds of model assemblies of atoms consisting of the b.c.c. type embryos and the disordered boundary regions connecting them are constructed to simulate the amorphous $Fe_{86}B_{14}$, $Fe_{80}B_{20}$ and $Fe_{75}B_{25}$ alloys. The lattice parameter of the embryos is taken to be the before mentioned value, 2.8665 A. The embryos are nearly spherical, containing 59 atoms, and in order to have the smooth and tight connections between the atoms in the structure, the boundary and the surface atoms of the embryos are relaxed by using the assumed interatomic potentials, as described in the section 2.3. In the course of the relaxation process, in which the atoms belonging to the embryo cores of various sizes are kept unrelaxed for the reason already mentioned in section 2.3, total interference functions as defined by Eq.(12) are examined, as given in Fig.21, to determine which embryo size is most probable for reproducing the experimentally obtained ones. It is worthy of noting that the shoulder on the high angle side of the second halo peak, which does not appear in the case of the isolated b.c.c. microcrystallites, is clearly seen, even when each embryo composed of 51 atoms retains the b.c.c. structure. This was satisfactorily discussed in a previous section, particularly with respect to the role of boundary layer atoms intervening between and connecting the neighbouring embryos. A small hump around $K = 7\ A^{-1}$ and a large one around $K = 8.25\ A^{-1}$ in the line profile correspond to (310) and (321) reflections from the ordinary b.c.c. crystals respectively, inevitably appearing on account of the large size of the embryos. Another

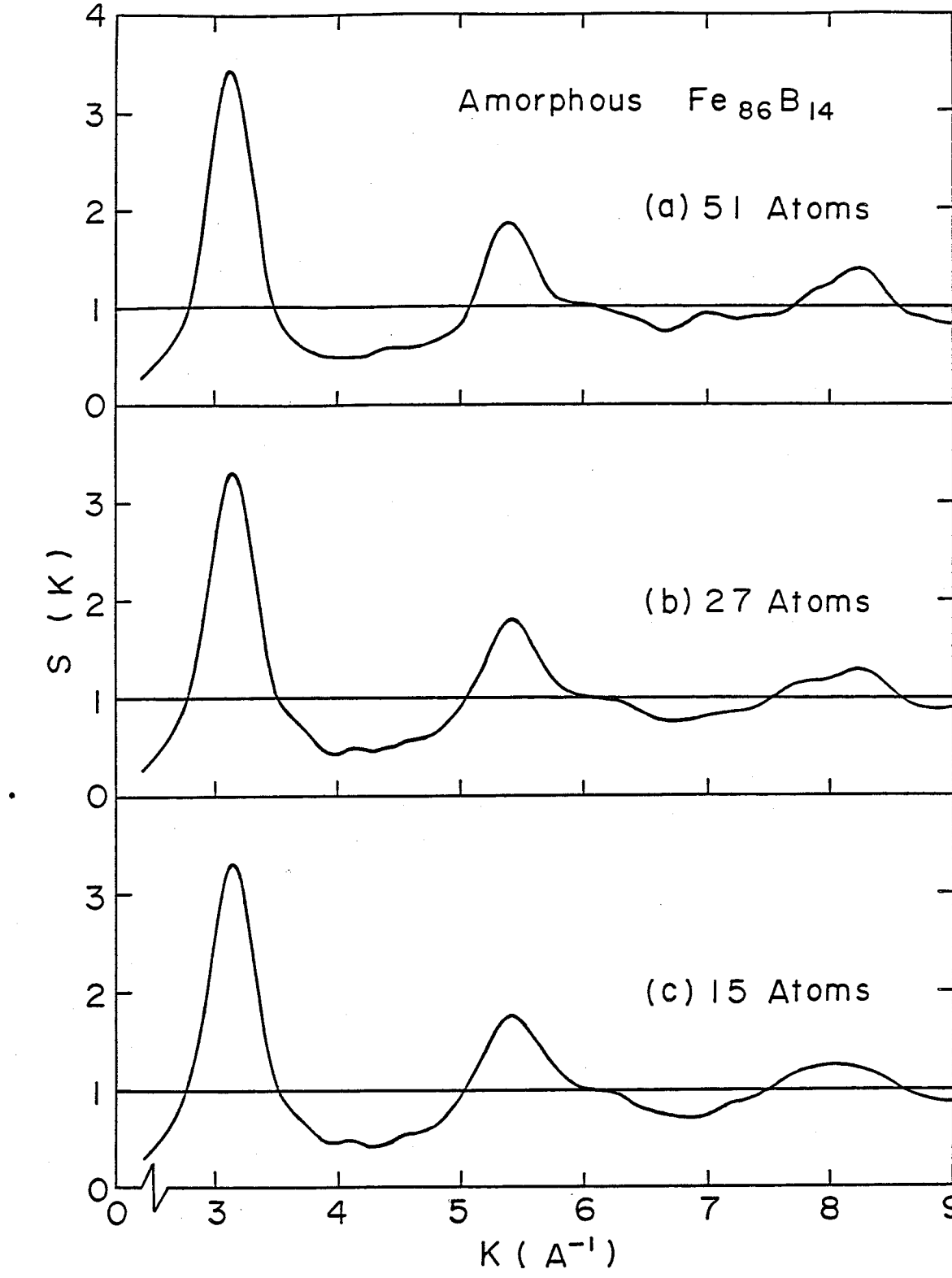

Fig. 21 The total S(K)'s for the amorphous $Fe_{86}B_{14}$ alloy with different core sizes of the b.c.c. embryos: (a) 51 atoms, (b) 27 atoms, and (c) 15 atoms.

tiny hump appearing at around $K = 7.9\ A^{-1}$ does not arise from any crystal plane reflection. As the size of the embryos is reduced through the relaxation process, the intensity of each halo peak is slightly decreased and the humps as described above become obscure owing to the lowering of the crystalline periodicity in the embryos. The hump at $K = 8.25\ A^{-1}$ persistently remains even in the case of the embryo composed of 27 atoms, but it diffuses into the third halo peak together with the smallest hump at $K = 7.9\ A^{-1}$ when the number of atoms in each embryo is decreased to 15, as shown in the bottom of Fig.21. Noteworthy is that, in this case, the total interference function agrees well with the experimental ones, especially those by Waseda and Chen.[21] A similar tendency can be seen in the total pair correlation function, as shown in Fig.22. When each embryo contains 51 atoms, the total pair correlation function shows the asymmetric first maximum with a tail extending beyond r $\approx$ 2.9 A and many other small humps. Some of them arise from the embryos of the b.c.c. structure as well as those in the total interference function of the same embryo size. For instance, the tail around 2.9 A corresponds to the second nearest neighbour distance of the b.c.c. structure, as described before. A small hump around 2.05 A observed in Fig.22 comes from the Fe-B correlations. Boudreaux[65] observed a small peak at a distance 1.5 times larger than the iron atom diameters between the first and second nearest neighbour shells in his models for the amorphous Fe-B alloys. He attributed this distance to the colinear arrangement of Fe-B-Fe in the amorphous structure. A small hump around 3.5 A in the total pair correlation functions in Fig.22 seems to accord with the pro-

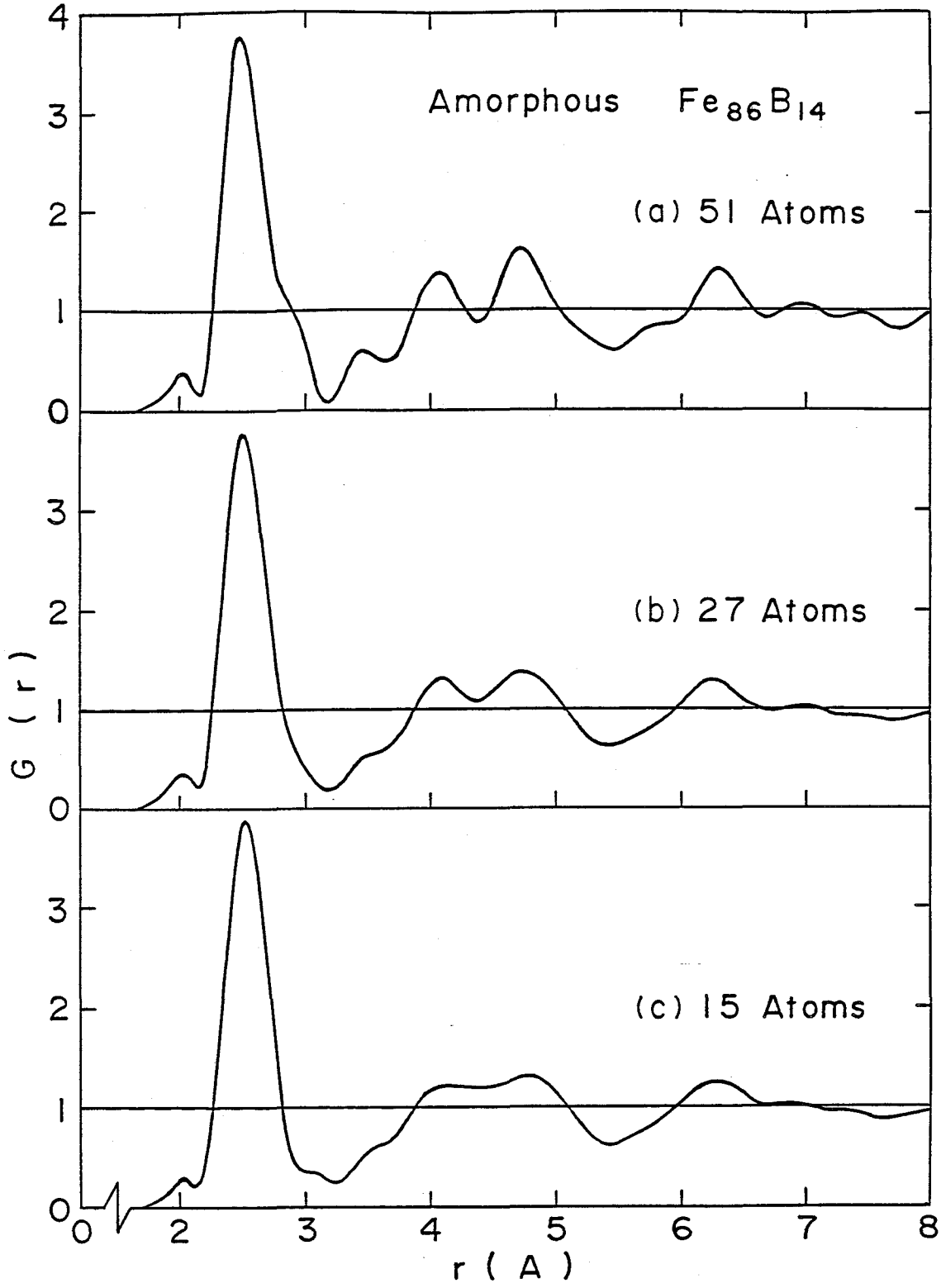

Fig. 22 The total G(r)'s corresponding respectively to the total S(K)'s, (a), (b) and (c) in Fig.21. The G(r)'s are obtained by the truncated Fourier transformation of the S(K)'s with K_{max}=15 A^{-1} in accordance with the x-ray diffraction experiments. The G(r) given in (b) is the same as that shown by the full line in Fig.19.

posal by Boudreaux. As the size of the embryos is lowered, the correlation function becomes more diffuse and the small humps in the profile become unclear. It can be readily known that the total pair correlation function represented by the full curve in Fig.19 is the same as that given in the middle of Fig.22. When the number of atoms in each embryo is reduced to 15, the total pair correlation function agrees well with that obtained from the diffraction data measured for the amorphous $Fe_{84}B_{16}$ alloy by Waseda and Chen especially as regards the shape of the second peak. In this case, about 40 outer atoms of each embryo having the b.c.c. structure are relaxed with surrounding boundary atoms by using assumed interatomic potentials. After the relaxation, the displacements from the initial positions of atoms in the transition regions are sometimes of the order of the interatomic distances. The ratio of the number of atoms in the embryo cores, that in the transition regions , and that in the disordered boundary regions is about 1:2:6. The atomic arrangement in the boundary regions is peculiar, and the effect of the embryos' structure on their surroundings will be discussed later in connection with the role of metalloid atoms.

In order to clarify the correlations of arrangement between like and unlike atoms in the model structure for the amorphous $Fe_{86}B_{14}$ alloy, total and partial pair correlation functions are calculated and shown in Fig.23. It can be seen from the figure that the partial pair correlation function for Fe-Fe pairs is chiefly responsible for determining the profile of the total one. A small hump at the forward edge of the first peak in the total pair correlation function corresponds to the contribution from Fe-B

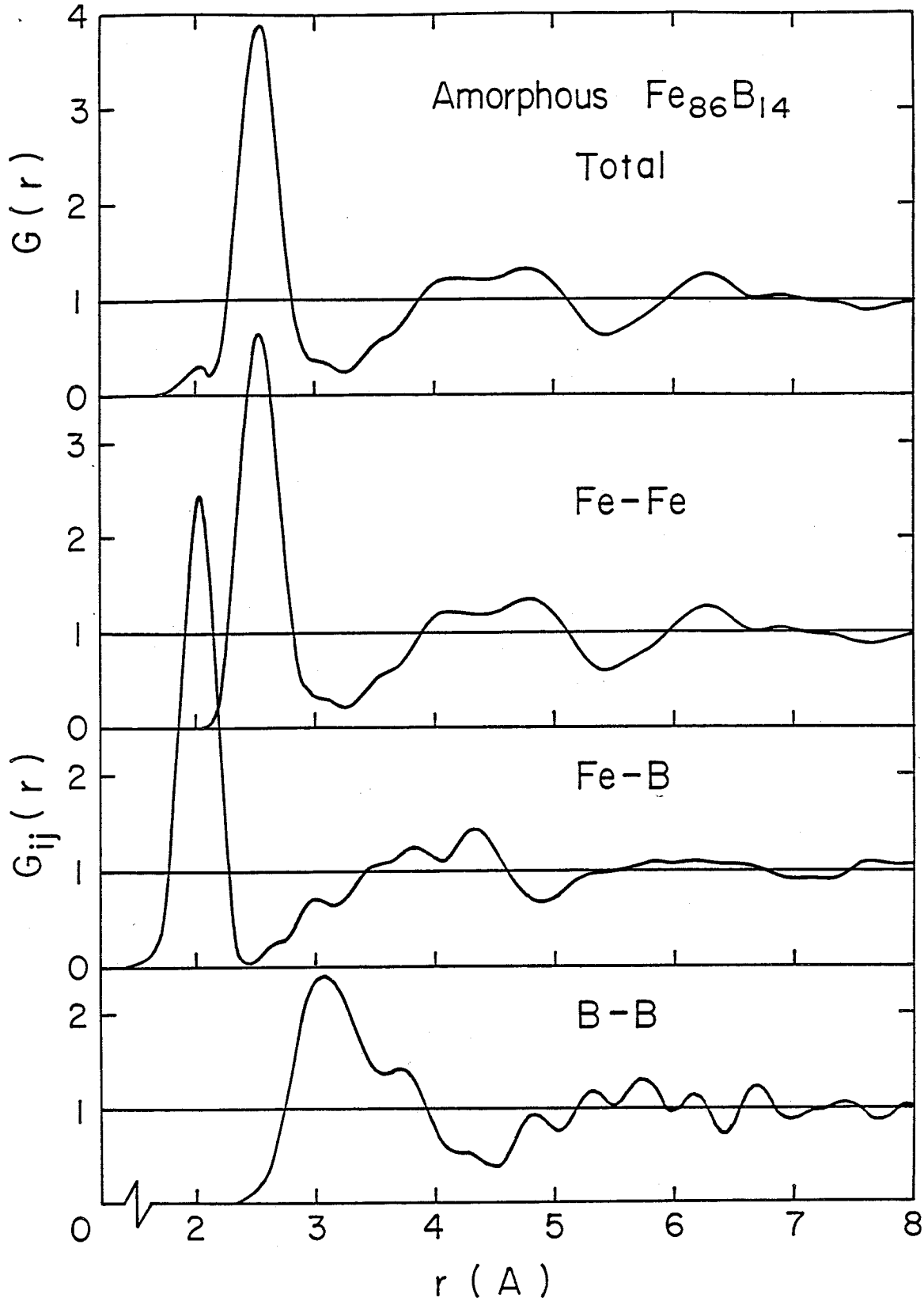

Fig. 23 The total and partial pair correlation functions, G(r) and $G_{ij}(r)$, for the amorphous $Fe_{86}B_{14}$ alloy. The total G(r) is the same as that given in (c) of Fig.22.

pairs. In the partial pair correlation function for B-B pairs, a broad maximum appears around 3.10 A. This B-B pair distance is much larger than the averaged diameter of the boron atom, about 1.5 A, in the present model structure, reflecting the fact that the boron atoms are put in the model structure separately not to have the close contact in parallel with the results of the experimental analysis on the P-P and Si-Si pair distances in other amorphous alloys. Since the weighing factor w_{BB} is below 0.001 in the case of the $Fe_{86}B_{14}$ alloy, the contribution of B-B pairs to the total pair correlation function is too small to be observed. In the previous calculation on the b.c.c. embryo model for amorphous iron, the peak height ratio of the second peak doublet in the pair correlation function is of the reversed type, which appears also in the partial correlation function for Fe-Fe pairs in Fig.23. Boudreaux[65] and Fujiwara et al.[66] constructed other models for the amorphous $Fe_{85}B_{15}$ alloy based on the concept of the relaxed DRP of spheres and concluded that the profiles of their reduced radial distribution functions gave the good reproduction of the characteristic features observed in the amorphous $Fe_{84}B_{16}$ alloy.[21] Their models as well as the embryo model gave the reversed subpeak height ratio of the second peak splitting in the pair correlation function. This agreement between the two and our model probably arises from the smallness of the size of boron atoms, which strongly influence the packing structure of iron atoms, as will be mentioned later. It must be noted that the pair correlation function of the embryo model for the amorphous $Fe_{86}B_{14}$ alloy shows the best agreement with that experimentally obtained, when the embryo size

is around 10 A in diameter corresponding to the 15 core atoms cluster. This fact clearly shows that the embryo model, which takes the medium range order into account, is fully applicable to describe the amorphous structure.

In order to see the effect of the boron concentration, the total pair correlation functions are calculated for the embryo models with the compositions, $Fe_{100-x}B_x$ (x=14, 20 and 25), as respectively shown in Fig.24. The number of core atoms belonging to each b.c.c. embryo is taken to be 15 for the three models. The ratio of the number of atoms in the cores, that in the transition regions and that in the disordered boundary regions is about 1:2:6 for the $Fe_{86}B_{14}$ and $Fe_{80}B_{20}$ alloy, and about 1:2:6.5:1.5 for the $Fe_{75}B_{25}$ alloy, where the last figures in the latter mean the number of atoms in the chemical embryos of the crystalline Fe_3B type. As the concentration of boron is increased, the intensity of a peak corresponding to the contribution from Fe-B pairs rises up at 2.05 A. The pair correlation functions for the amorphous $Fe_{80}B_{20}$ and $Fe_{75}B_{25}$ alloy have a "reversed" second peak splitting, which does not agree with so far obtained experimental results.[11,21] This disagreement was seen also in the relaxed DRP models with 20 and 25 at%B by Boudreaux.[65] An improvement of the calculation to have the "normal" second peak splitting for the high boron concentration case will be shown later in this section.

In Fig.25 are shown the total interference functions corresponding respectively to the correlation functions in Fig.24. They exhibit the characteristic features of diffraction intensity distribution of the amorphous Fe-B alloys, especially the smallness

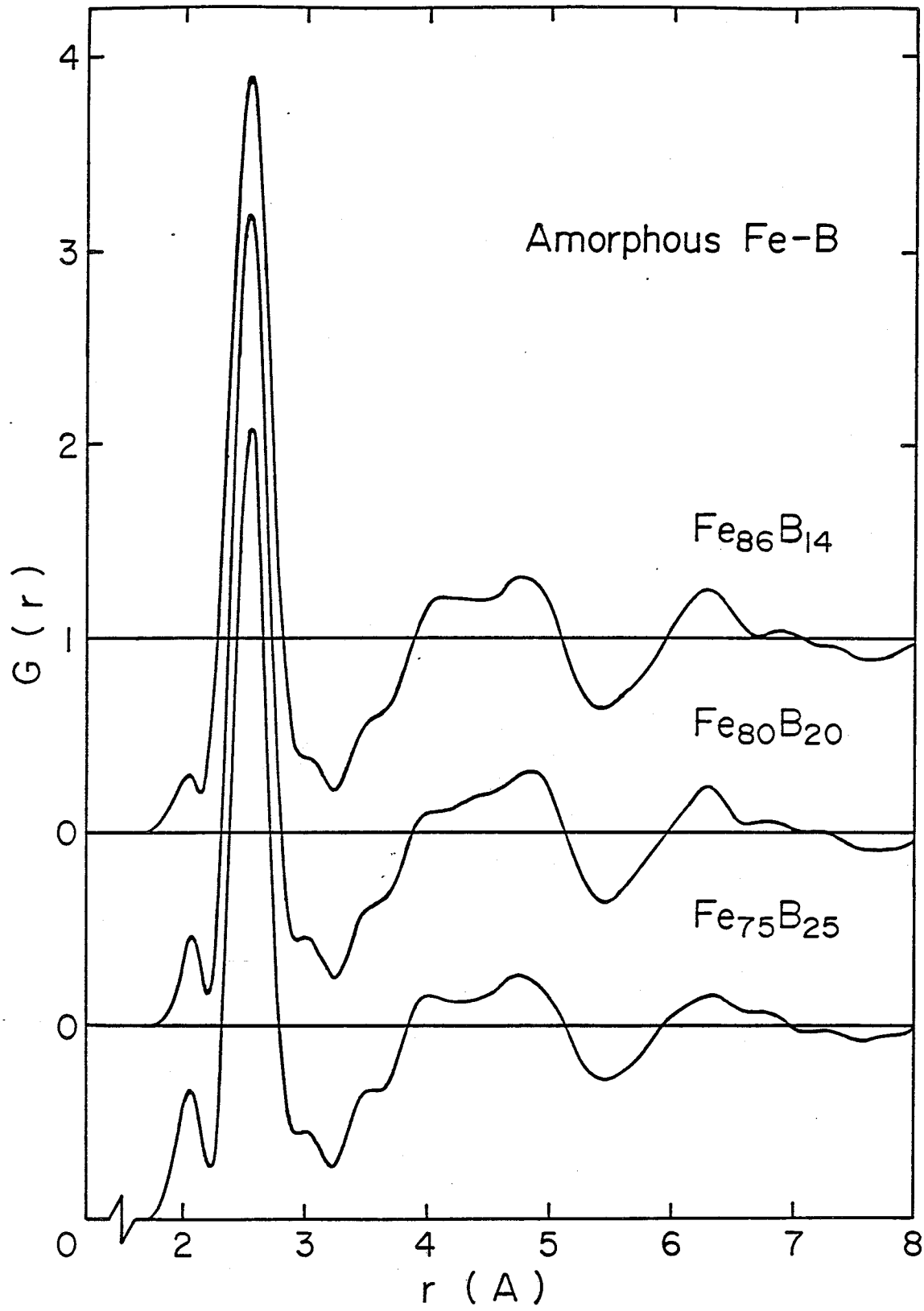

Fig. 24 The total G(r)'s for the amorphous $Fe_{100-x}B_x$ (x=14, 20 and 25) alloys. The embryo core is of 15 atoms and $r_{0_{Fe-B}}$ is 2.05 A.

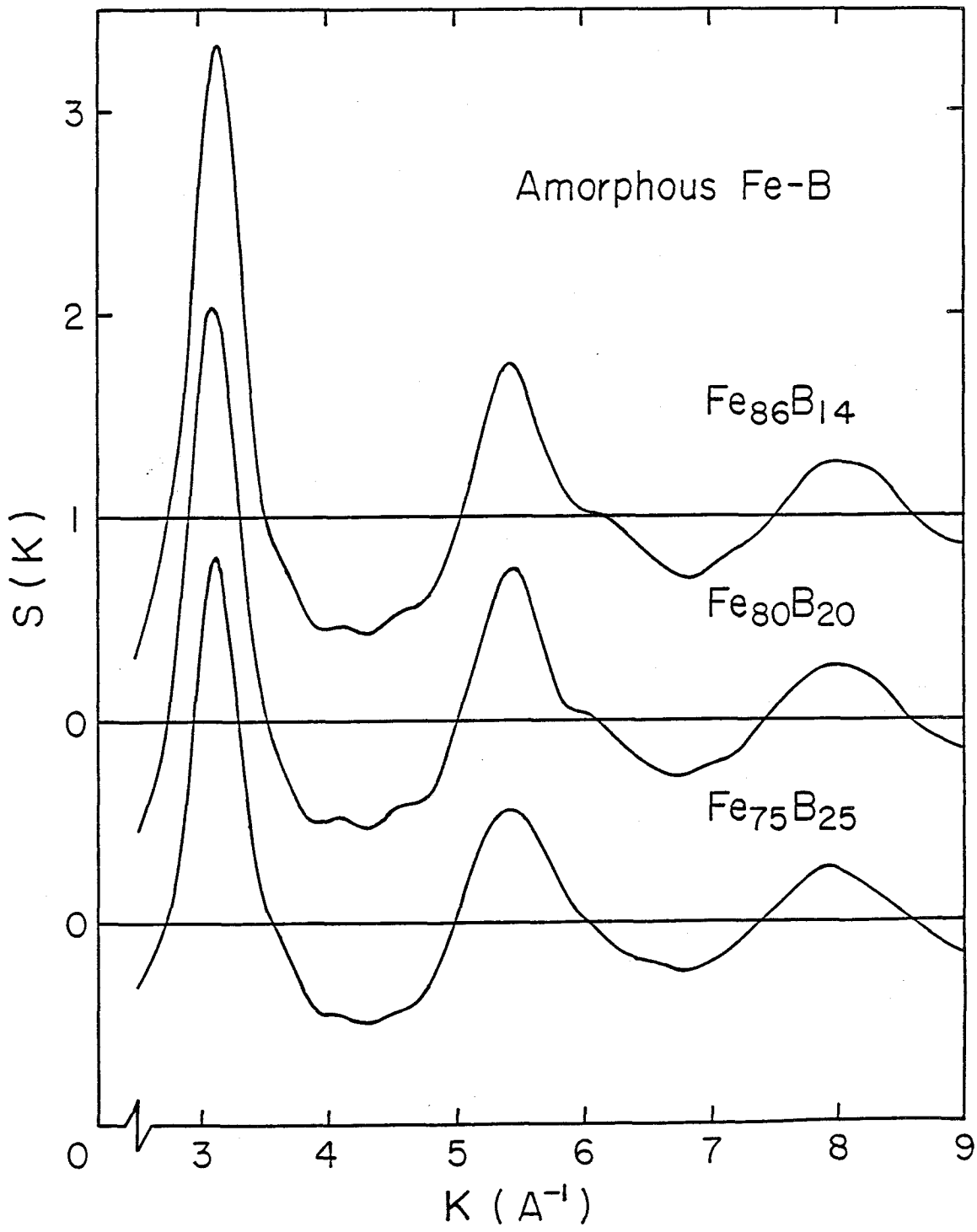

Fig. 25 The total S(K)'s corresponding respectively to the total G(r)'s in Fig. 24.

of the second peak shoulder. In the interference function for the amorphous $Fe_{86}B_{14}$ alloy, the peak profile, relative positions and intensities of halo peaks well agree with the experimental results.[21] However, disagreements with experiments, regarding the first peak intensity and the second peak shoulder, appear as the boron content is increased: The first peak heights of the amorphous $Fe_{80}B_{20}$ and $Fe_{75}B_{25}$ alloy are slightly lower than those observed by the experiments,[11,21] and, in the case of the $Fe_{75}B_{25}$ alloy, the second halo peak becomes broader and its shoulder is almost missing.

The crystalline embryo model so far treated are constructed by assuming the average Fe-B spacing to be 2.05 A. Recently, Lamperter et al.[16] obtained the total and partial structure factors of the amorphous $Fe_{80}B_{20}$ alloy by the x-ray and neutron diffraction using the isotopic substitution method and derived the partial reduced radial distribution functions. The partial correlation function for Fe-B pairs showed a very sharp and high first maximum at r=2.14 A, which reflected a well defined Fe-B distance. Therefore, the improvement of the model calculation by introducing this measured value into the average Fe-B spacing, r_{0Fe-B}, is necessary, and this leads to essential changes in the interference function and the pair correlation function as the following figures show.

In Fig.26 are shown the total pair correlation functions of the crystalline embryo models relaxed by setting the value of r_{0Fe-B} in Eq.(5) at 2.14 A. In the calculation, other parameters, r_{0Fe-Fe}, r_{0B-B}, ε and α, are not altered. Alloy concentrations,

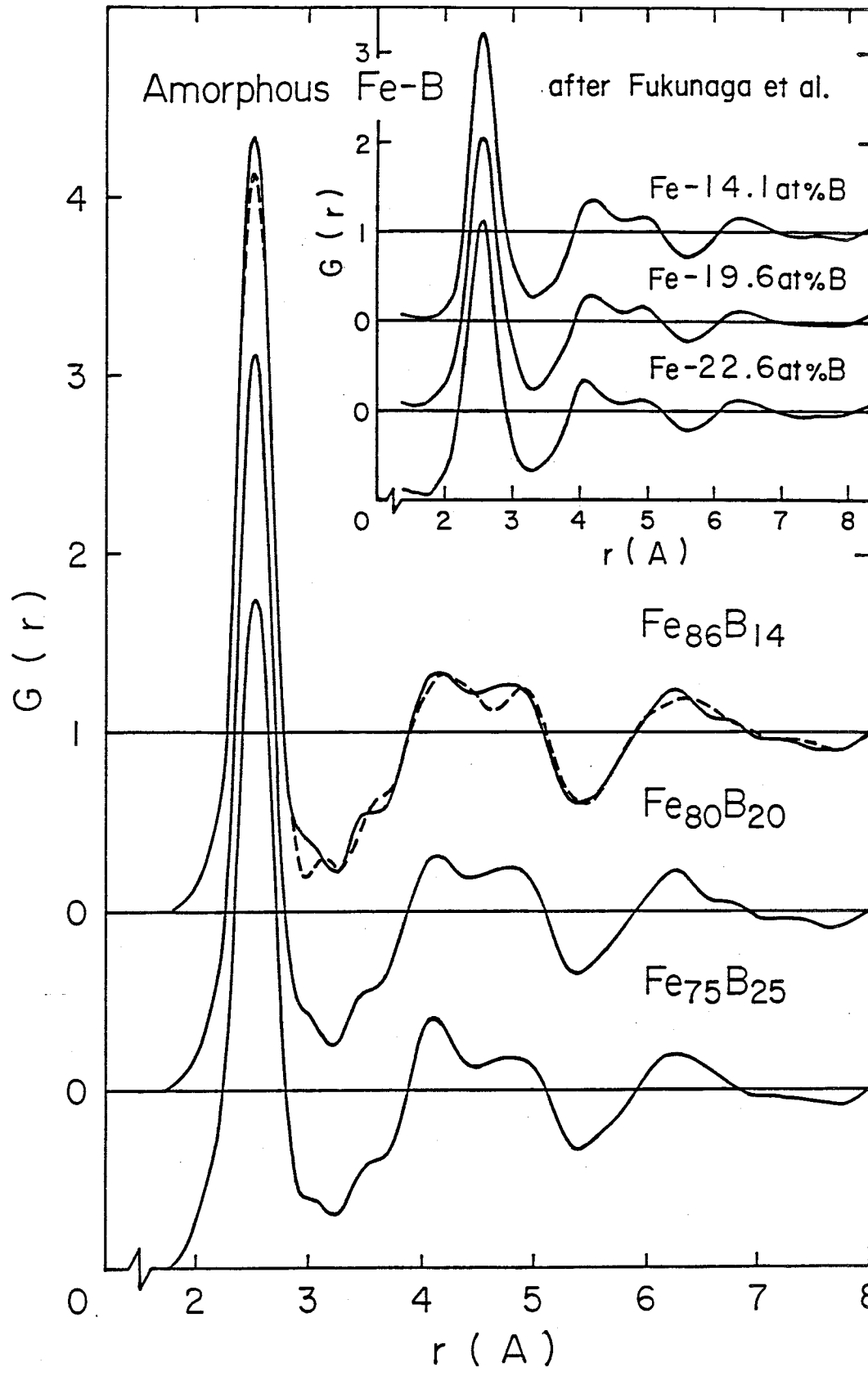

Fig. 26 The total G(r)'s for the amorphous $Fe_{100-x}B_x$ (x=14, 20 and 25) alloys. The embryo core is of 15 atoms and $r_{0_{Fe-B}}$ is 2.14 A. The G(r) (broken curve) for the $Fe_{86}B_{14}$ alloy is calculated from the DRP model. The inset is the total G(r)'s obtained by Fukunaga et al.

densities and the number of atoms belonging to each embryo are the same as in the before mentioned case. As a result of the calculation, a small hump around 2.05 A, which is seen in every total pair correlation function in Fig.24, disappears and no splitting is observed in the first peak. The contribution from Fe-B correlations lies around 2.14 A, which will be shown later. Furthermore, it is clearly seen from the figure that the second peak splitting is changed from "reversed" to "normal" for three kinds of amorphous Fe-B alloys. Except for the first peak height, the peak profiles, ratios and positions in the correlation functions are in good agreements with the experiments by Fukunaga et al.[11] which are given in the upper right hand side in the figure and in Fig.3(b). The total pair correlation function of the DRP model for the $Fe_{86}B_{14}$ alloy is also calculated and represented by a broken line in the same figure. In the DRP model, atoms are distributed at random in the overall volume according to the computer-generated random coordinates, until the system has the same concentration and density as the embryo model. Then, the atoms are relaxed by using the same interatomic potentials as in the embryo model. The total pair correlation function of the DRP model is similar to that of the embryo model. It is worthy of note that the heights of the first peak of the two functions are equally too high as compared with those experimentally obtained. This arises probably form the assumed interatomic potentials employed in the relaxation process. Similar disagreement with experiment existed in Boudreaux's calculation.[65]

The total interference functions corresponding to the total

pair correlation functions in Fig.26 are shown in Fig.27. The interference functions exhibit the characteristic features of diffraction intensity distribution of the amorphous Fe-B alloys, especially the splitting of the second halo peak. As the boron concentration is increased, the intensity of the first halo peak and of the shoulder of the second one is decreased. These results well agree with the experiments by Fukunaga et al., although the first peak height for the anorphous $Fe_{75}B_{25}$ alloy is low enough to be compared with them. The total interference function of the DRP model for the amorphous $Fe_{86}B_{14}$ alloy is given by a broken line. Small differences between two models are seen in relative positions and intensities of halo peaks. The interference function of the embryo model gives the better agreement with the experimental one by Fukunaga et al., which is shown in the upper right hand side in the figure and in Fig.3(a), than that of the DRP model, especially as regards the intensity of the first halo peak and of the shoulder in the second halo one.

The effect of the average distance of Fe-B pairs on the correlation function in the present model is readily seen in Fig.28, in which total and partial pair correlation functions for the amorphous $Fe_{86}B_{14}$ alloy are shown. In the partial correlation function for Fe-B pairs, the first maximum appears around 2.14 A, which contributes the intensity distribution at the forward edge of the first peak in the total one. It must be noted that the peak height ratio of the second peak doublet in the partial correlation function for Fe-Fe pairs is of the normal type, which differs in both cases of the previous calculation of the b.c.c. embryo model for

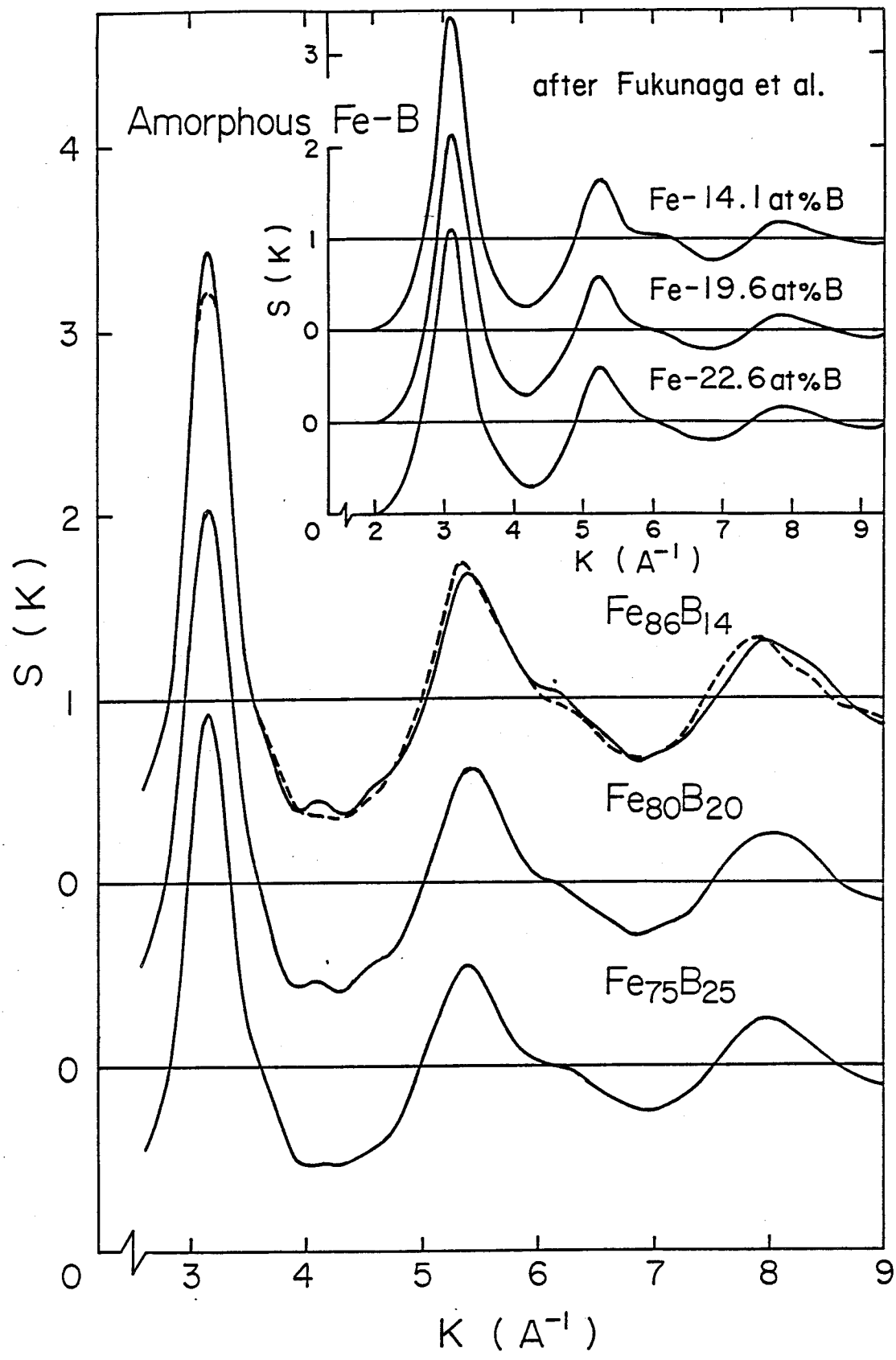

Fig. 27 The total S(K)'s corresponding respectively to the total G(r)'s in Fig.26.

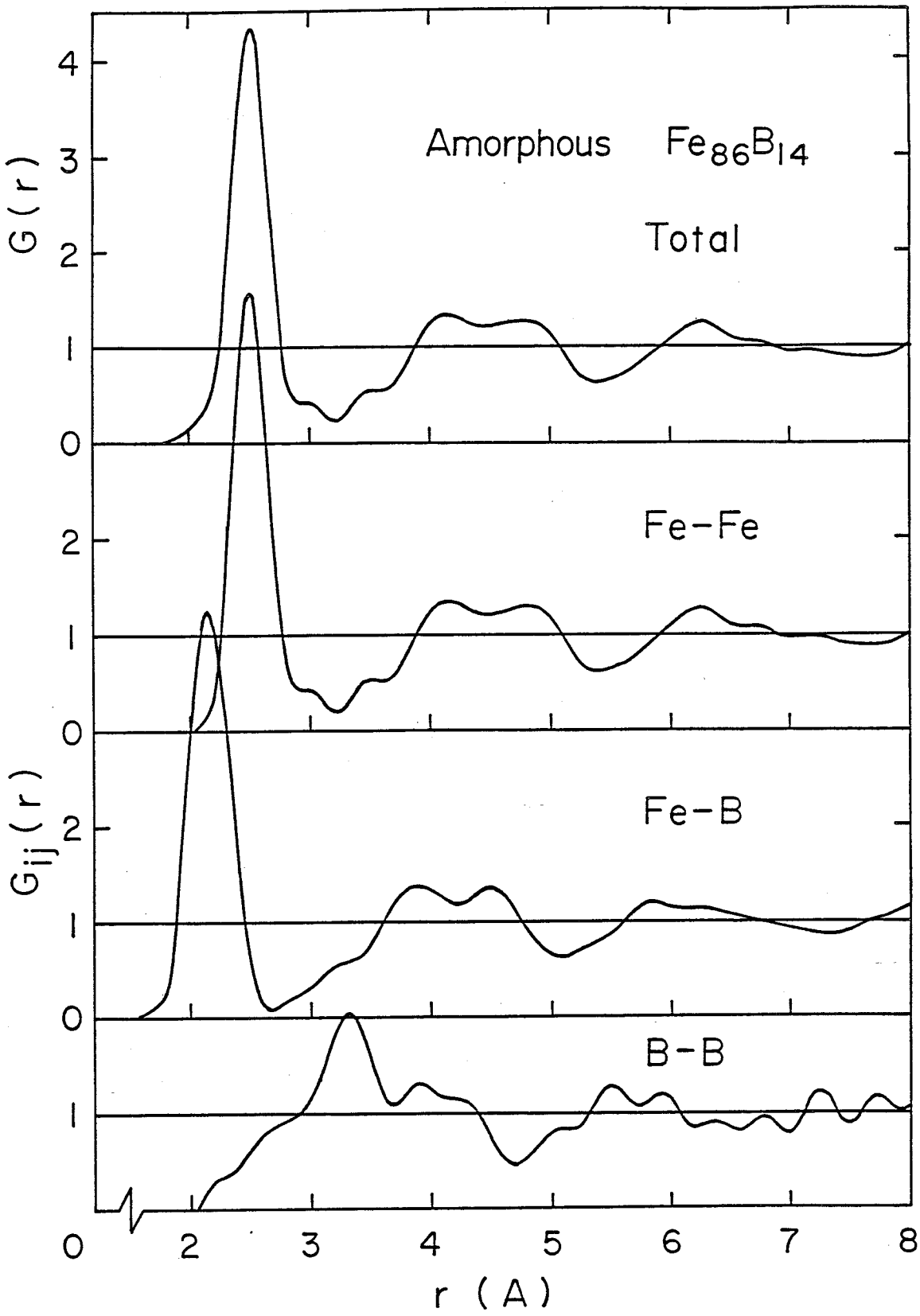

Fig. 28 The total and partial G(r)'s for the amorphous $Fe_{86}B_{14}$ alloy. The total G(r) is the same as that given in Fig.26.

the amorphous iron and the present one as in Fig.23. Therefore, it is concluded that the shape of the second peak in the total correlation function depends critically on the size of boron atoms in the model alloy.

4. CALCULATION OF HIGH RESOLUTION ELECTRON IMAGE FROM CRYSTALLINE EMBRYO

Recently, the structure of very thin films of amorphous materials has been intensively studied through the HREM with the axial illumination, and the lattice like images spreading over the ranges of the order of 10 A are often observed in the bright-field images even in the as quenched samples.[31-33] These lattice like images could arise from the crystalline embryo surrounded by the disordered region, as described by our model. As mentioned in the last chapter, the calculated diffraction functions are in good agreement with the experiments, when the embryo size is taken to be as small as 10 A in diameter corresponding to some twenty atoms cluster, which includes a part of transition region, and it is concluded that the quasi-crystalline clusters of this size most probably exist in the real amorphous structure.

The interpretation of high resolution electron micrographs of amorphous materials is a substantial problem. In fact, it is very difficult to conclude the presence or absence of ordered regions in the amorphous materials, unless the experimentally obtained images are exactly compared with the calculated ones from various structural models. Therefore, in order to compare with the above experimental results and confirm the existence of the medium range order in the amorphous structure, the computer calculation of the contrast of high resolution electron micrographs from the very thin film of iron based amorphous alloy is carried out by using the embryo model and the kinematical theory of electron diffraction. When an appropriate value of the spherical aberration constant and

the amount of defocus are chosen, the lattice-like fringes or dots contrast with the spacings of about 2 A and the diameter of the order of 10 A are well reproduced by the calculation. Variations, overlapping, and appearance frequency of the images are also calculated and compared with the experimental results.

4.1 Kinematical Theory of Electron Diffraction

The kinematical approximation is valid for the calculation of electron images of very thin amorphous films.[81,101] The computations are carried out according to the procedure already described by Howie et al.[80] and Howie.[101]

When the incident electron wave $\exp(i\mathbf{k}\cdot\mathbf{r})$ falls on a thin specimen containing N-atoms at the positions $\mathbf{r}_j$ and produces the scattered wave with the wave vector $\mathbf{k}'$, the two wave vectors are related with the scattering vector $\mathbf{K}$ as

$$\mathbf{k}' = \mathbf{k} + \mathbf{K}. \tag{15}$$

The total scattered wave amplitude $\Psi_s(\mathbf{r})$ at a point $\mathbf{r}$ is, in the single scattering, given by

$$\Psi_s(\mathbf{r}) = \frac{i\lambda A_{\mathbf{K}}}{4\pi^2} \sum_j \sum_K f_j(K)\cdot\exp(i\mathbf{K}\cdot(\mathbf{r} - \mathbf{r}_j) - i\gamma(\theta_{k'})), \tag{16}$$

with

$$\gamma(\theta_{k'}) = \frac{\pi\Delta f\theta_{k'}^2}{\lambda} + \frac{\pi C_s\theta_{k'}^4}{2\lambda}, \tag{17}$$

where λ is the wavelength of electrons and $f_j(K)$ is the atomic scattering amplitude. The summation over j is on the N-atoms at the positions $\mathbf{r}_j$ in the model structure. The summation over K is on a two-dimensional grid of points within the objective aperture and A_K is the unit cell area of this grid. The effects of the defocus value Δf and the spherical aberration constant of the objective lens C_s are described by the phase shift γ which depends on the scattering angle $\theta_{k'}$, which the scattered wave vector $\mathbf{k}'$ makes with the optical axis. For the bright-field images, the scattered

waves interfere with the transmitted waves, the amplitude of which is taken to be unity, and the phase shift between the directly transmitted waves and the scattered waves modulated by defocusing and aberrations lead to the phase contrast. Under the condition of axial illumination, the bright-field image intensity $I_B(\mathbf{r})$ from a thin specimen is given in the form,

$$I_B(\mathbf{r}) = |1 + \Psi_s(\mathbf{r})|^2. \tag{18}$$

As $\mathbf{k}'$ in Eq.(15) lies nearly parallel to $\mathbf{k}$ or the optical axis, K_z is almost zero and $\Psi_s(\mathbf{r})$ in Eq.(16) is relatively insensitive to the z-coordinates of all the atoms within the specimen. Therefore, the images obtained are essentially two-dimensional projections of the structure.

The calculated interference function, S(K), of the embryo model for the amorphous $Fe_{86}B_{14}$ alloy showed the high first maximum at $K = 3.1\ A^{-1}$ and the full width at half maximum (FWHM) value of $0.5\ A^{-1}$ (where $K = 4\pi\sin(\theta_k,/2)/\lambda$), which are in good agreement with the experiment.[11] The round aperture with a radius in the reciprocal-space equal to $3.9\ A^{-1}$ and concentric with the optical axis(axial illumination) is chosen, and, therefore, the entire first halo intensity distribution contributes the interference image contrast. The wavelength λ is taken to be 0.0251 A (for 200kV electrons). The dimensions, k_x and k_y, of the unit cell of the grid within the object aperture are taken to be $0.06\ A^{-1}$. Then, A_k and $\lambda A_K/4\pi^2$ in Eq.(16) are $3.6 \times 10^{-3}\ (A^{-1})^2$ and $2.29 \times 10^{-6}\ A^{-1}$ respectively. Since the coefficient of the scattered wave amplitude is very small, the bright-field intensity becomes

$$I_B(\mathbf{r}) \simeq 1 + \Psi_s^*(\mathbf{r}) + \Psi_s(\mathbf{r}). \tag{19}$$

In the present calculation, the values of parameters, C_s and Δf, in Eq.(17) are chosen as follows in accordance with the actual experimental conditions: $C_s = 1\text{mm}$ and $\Delta f = -500 \sim -1500$ A. In fact, the appearance of axial interference images of amorphous materials is very sensitive to the defocus distance, as the transfer function $\exp(-i\gamma(\theta_{k'}))$ in Eq.(16) shows.[102] Especially, the dominant term in Eq.(19) is the $\sin\gamma$ function, of which oscillations can result in the reversal or suppression of particular ranges of spatial frequency in the image. It is obvious that the strongest contrast in the image is obtained with $\sin\gamma = \pm 1$, as will be more precisely discussed later.

The diffracted intensity $I(\mathbf{K})$ at any point in the reciprocal-space is given by the equation (8), which is already shown in section 3.1. The equation (8) can be rewritten in the form,

$$\frac{I(\mathbf{K})}{N|f(K)|^2} = 1 + \frac{1}{N} \sum_j \sum_{1 \neq j} \exp(-i\mathbf{K}\cdot(\mathbf{r}_1 - \mathbf{r}_j)). \tag{20}$$

In the analysis of amorphous structure in the diffraction experiments, it is usually assumed that the specimen structure is sufficiently homogeneous and isotropic and described by the pair correlation function $G(r)$ which depends only on $r = |\mathbf{r}_1 - \mathbf{r}_j|$. If the diffracted intensity is isotropic as well, $I(\mathbf{K})/N|f(K)|^2$ in Eq.(20) becomes the interference function $S(K)$ as shown in Eq.(10) and the electron image contrast of the amorphous structure will be flattened giving rise to a structureless white micrograph image even in

the high resolution electron microscopy. However, the model assembly used in this study is composed of a small number of atoms, corresponding to a thin film case, and, in addition, contains a very small diffracting b.c.c. cluster surrounded by the DRP structure region, as is mentioned in the section 2.4. Therefore, the anisotropic scattering will take place and the diffracted intensity distribution calculated from $I(\mathbf{K})/N|f(K)|^2$ in Eq.(20) is expected to be inhomogeneous, exhibiting the fine structure of the amorphous thin specimen.

At the center of atomic assemblies of 20 A in diameter extracted from the embryo model structure, a b.c.c. like cluster exists surrounded by the DRP structure. In the present calculations under the axial illumination, a round aperture is placed symmetrically on the optical axis, covering the direct beam spot and the whole first halo diffraction ring. When the incident beam is taken to be along the [001] axis of the b.c.c. embryo, four {110} diffraction spots symmetrically lie in the first halo ring. Therefore, the embryo could contribute to the interference image and produce a lattice image. In the next section, the calculated high resolution image contrasts with the beam incidence along the z-axis of the b.c.c. embryo will be shown in the first place. Then, the changes of the image are examined by rotating the assembly about the [010] and the [110] axis of the embryo. The interference image in the case of the total thickness of 40A is also calculated by using the two overlapping embryos where the crystal axes of them is not coincident with each other.

4.2 Image with Beam Incidence along Z-axis of B.C.C. Embryo

When the incident beam is along the z-axis of the b.c.c. embryo, the diffraction from the {110} lattice planes with a spacing of 2.03 A will take place and contribute to the image contrast. The appearance of the axial bright-field image is a sensitive function of the defocus distance, Δf, as mentioned before, since the oscillations of the transfer function result in the suppression of particular ranges of spatial frequency in the image. The defocus value is first taken as -500 A which is derived from the equation $(C_s\lambda)^{1/2}$ corresponding to the Scherzer defocus. The bright-field image contrasts thus calculated for two different assemblies with different embryo core sizes, one with 15 atoms and the other 51 atoms, are shown in Fig.29 and Fig.30 respectively. The b.c.c. structure of the latter extends to the fourth neighbour shell from the central atom. The isointensity contours are represented by full lines and dotted lines, the former representing the intensities above the unity, $I_B = 1$, and the latter below that. The $I_B = 1$ contours are left out. The dimensions in the x- and y-range of the image are 20×20 A. Two-dimensional projection of the model assembly consisting of an embryo and disordered region is within the circle of 20 A in diameter. Near the centres of the both contour maps, the projected positions of the embryo core atoms are shown by 9 and 21 circles, respectively, with broken lines. No lattice like image contrast appears in the central part of both figures, but two sets of high-intensity fringe contrasts perpendicular with each other are clearly seen outside of the projection of the model assembly. Their directions are nearly parallel to {110} planes of

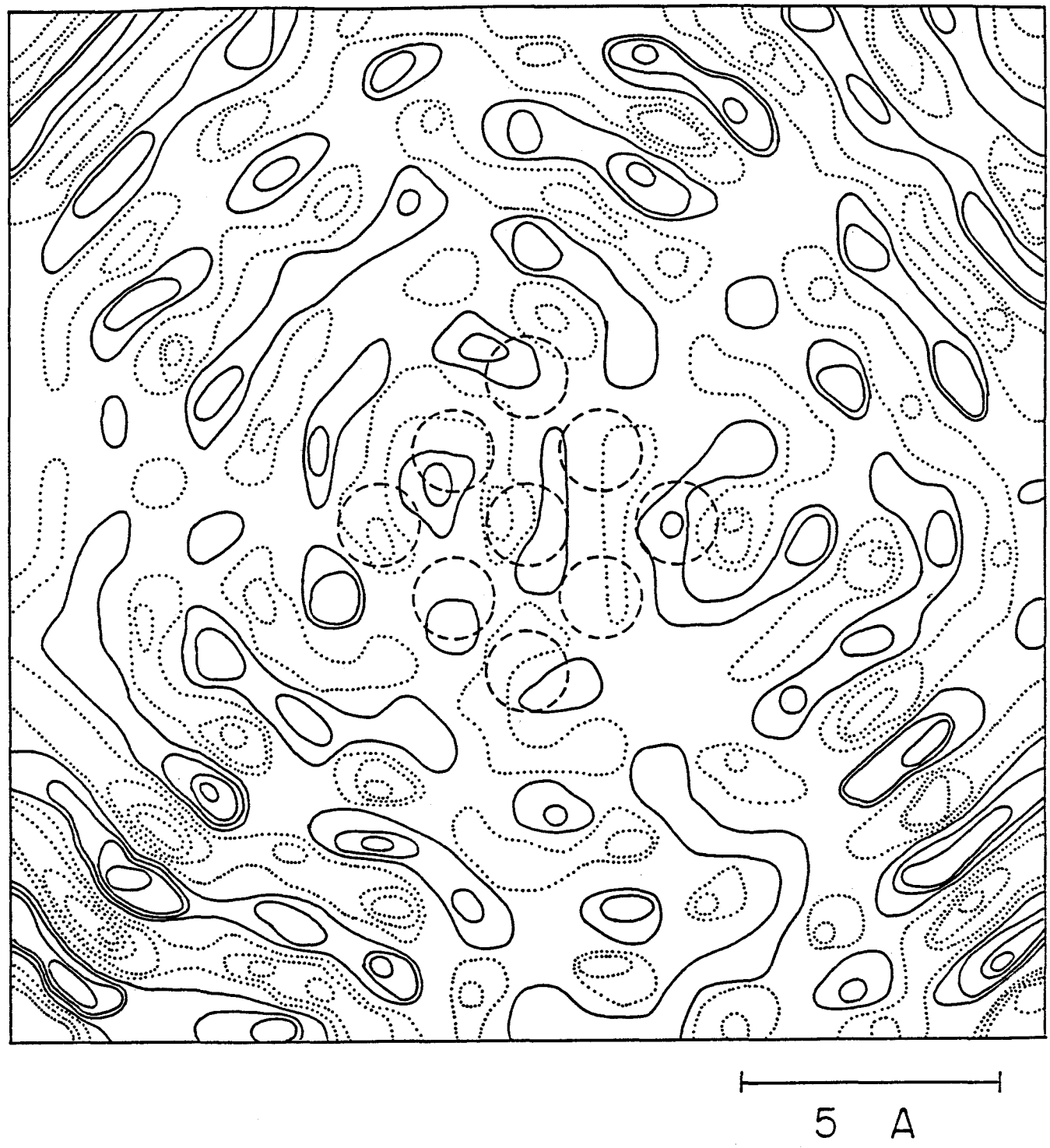

Fig. 29 The axial bright-field image calculated from the model assembly, which contains an embryo with 15 atoms b.c.c. core, with the beam incidence along z-axis of embryo and with $\Delta f = -500$ A. Iso-intensity contours are represented by full lines, $I_B > 1$, and dotted lines, $I_B < 1$, and dimensions of the image are 20x20 A. Two-dimensional projection of the model aggregate is within the circle of 20 A in diameter and projected positions of core atoms are shown by 9 circles with broken lines.

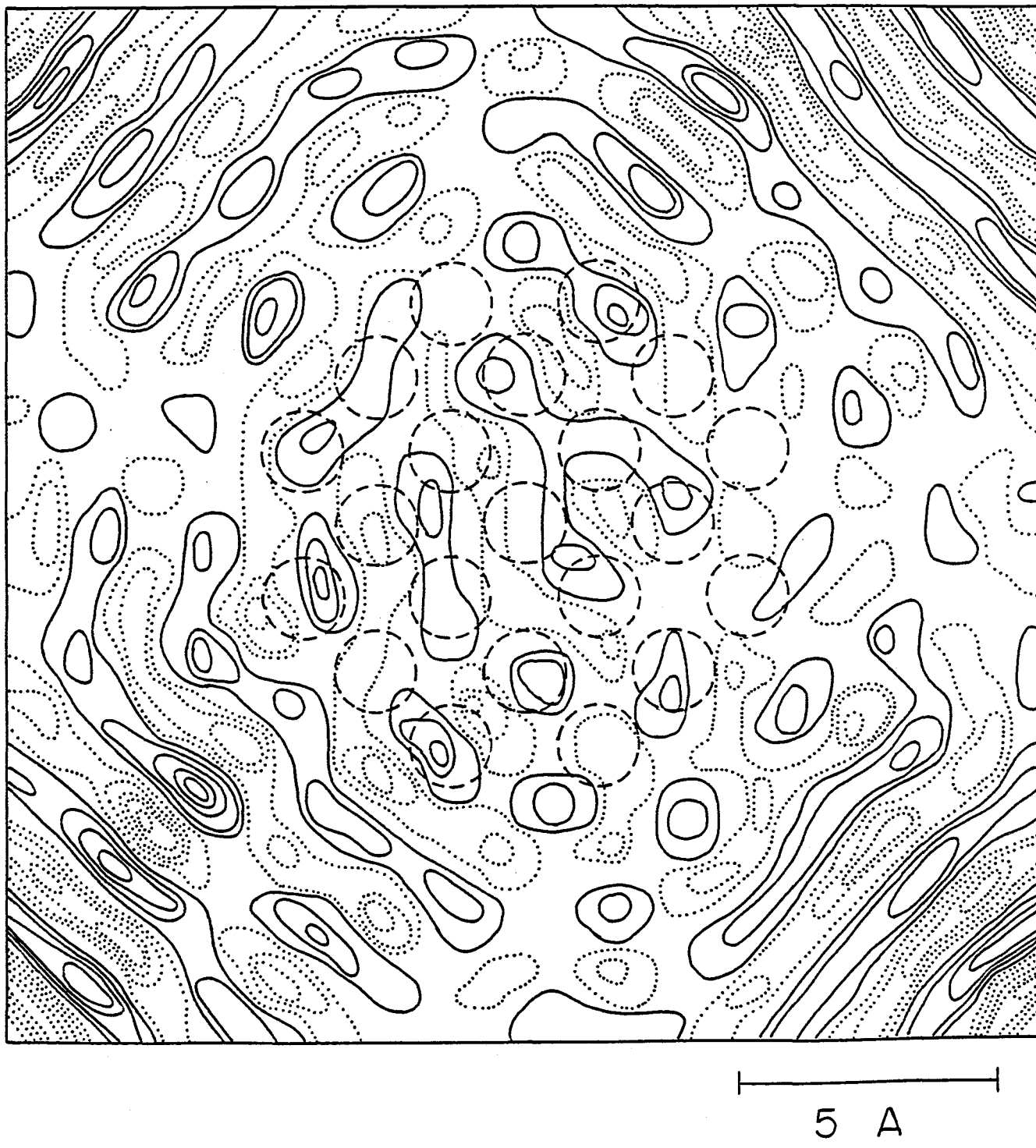

Fig. 30 The axial bright-field image calculated from the model assembly containing an embryo with 51 atoms core, projected positions of which are shown by 21 circles with broken lines. Isointensity contours and conditions in the calculation are just the same as those in Fig.29.

the embryos and their spatial periodicity is about 2 A, which is very close to the {110} lattice spacing of the b.c.c. embryo. The regularity and the contrast of the fringes are more pronounced in the case of the 51 atoms core.

In the above illumination condition, it is easily imagined that the {110} diffraction effect will occur at the embryo core, and the interference between the diffracted and transmitted waves will bring about the two sets of the lattice fringes parallel to {110} in the image contrast. Further calculations are carried out to see the appearance of fringy contrasts far outside of these micrographs, and it is found that the fringe spacings range from $\sim$2.1 A to $\sim$1.7 A, which are around the value, 2.03 A, of the {110} spacing of b.c.c. The reciprocal values multiplied by 2π of them almost correspond to the K values within the aperture, where the contrast transfer function, $\sin\gamma$, becomes $\sim\pm1$ as will be shown later. Superposition of the phase contrasts formed by these different K values and the {110} lattice periodicity in the b.c.c. embryo gives the fringe contrasts just corresponding to those in the calculated image contrast maps. It is, therefore, concluded that the fringe contrasts are the modulated and displaced {110} lattice fringes from the embryo and that the value, -500 A, of Δf is not the optimum defocus distance to cancel out the phase shift rising from the spherical aberration, $C_s = 1$ mm, in the given aperture configuration. It is noteworthy that the appearance of the fringe contrasts is essentially the same between the 15 and 51 atoms embryo cases, although the fringes of the latter case is clearer. In order to see the effect of the very smallest embryos on the high resolution

image contrast, we employ the 15 atoms embryo in the calculation hereafter. The 51 atoms embryo seems to be too large to be a general one, since it has been found in the previous chapter that the 15 atoms embryo model well reproduces the experimentally obtained S(K) and G(r) functions while the 51 atoms model reproduces some traces of crystalline nature in S(K) and G(r).

In order to identify the effect of the crystalline embryo on the image contrast formation, the axial bright-field image from the DRP model structure constructed according to computer-generated random coordinates is calculated with the same aperture configuration and the same values of C_s and Δf as in the before. The DRP assembly is a sphere containing about 330 iron atoms. The calculated isointensity image contours are shown in Fig.31 with the same manner and the same magnification as in Fig.29 and Fig.30. The image contrasts are observed all over the picture as well as in the embryo model, but the lattice-like fringe contrasts are not seen in accordance with the lack of the crystalline periodicity in the DRP structure.

As already shown in the above figures and mentioned, when the value of the defocus distance, Δf, is chosen as -500 A, the calculated bright-field image contrasts appear beyond the area of the xy projection of the model structure. Under the optimum defocus condition, however, the calculated interference image contrasts should essentially coincide with the projection of the model structure. Therefore, in order to determine the optimum defocus value, the contrast transfer function $\sin\gamma$, which dominantly affects the calculated image contrasts as mentioned in the section 4.1, is exam-

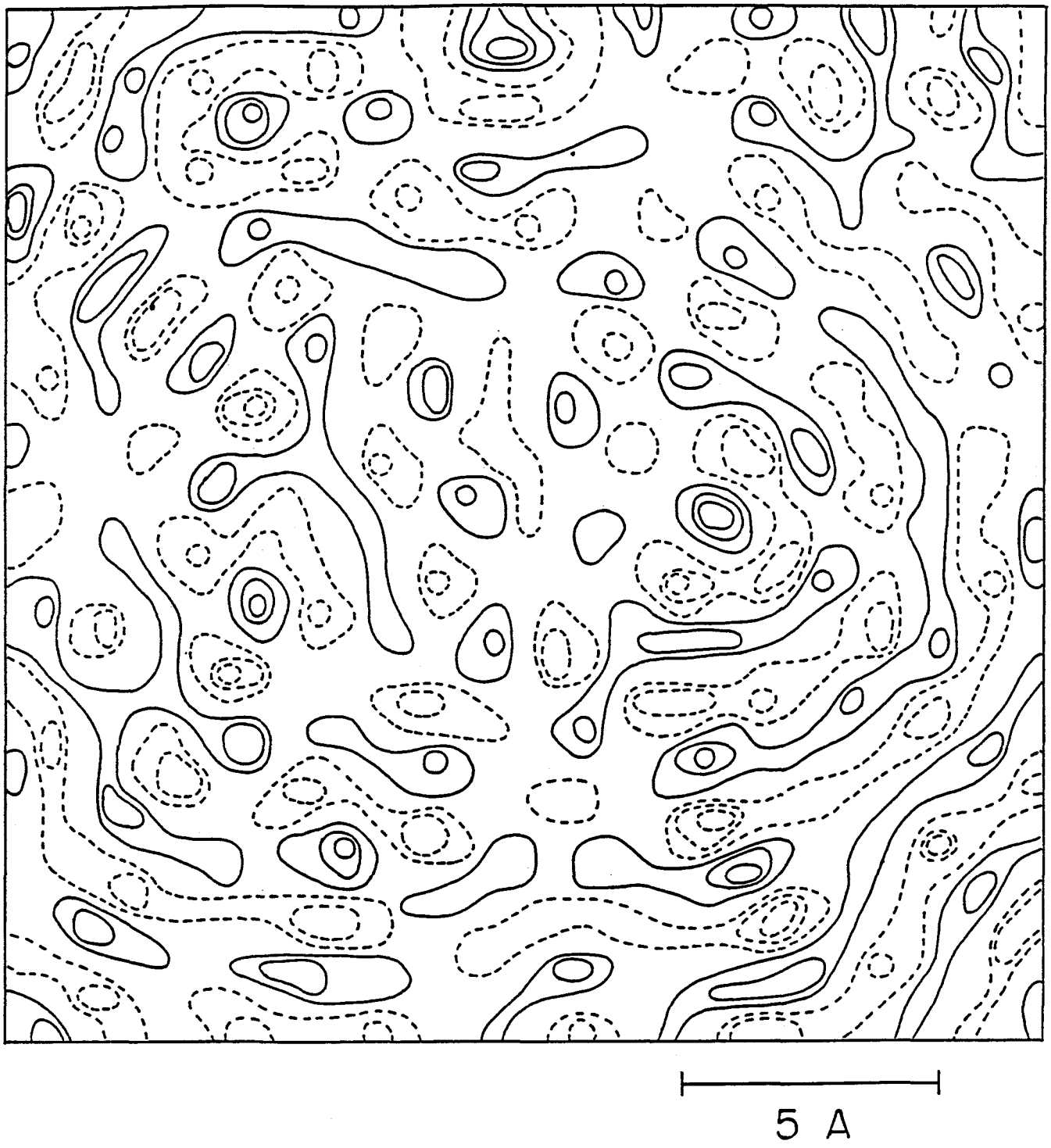

Fig. 31 The axial bright-field image calculated from the DRP model structure with Δf=-500 A. The isointensity contours are shown with the same manner and the same magnification as in Fig.29 and Fig.30.

ined by varying the value of Δf. In general, when the $\sin\gamma$ function is made nearly ± 1 at the K value of a spatial periodicity by choosing a particular value of Δf, this periodicity in the object structure will be strongly imaged. In Fig.32 are given the $\sin\gamma$ functions for two different defocus values, -500 A and -1500 A. In the case of the Scherzer defocus, $\Delta f = -500$ A, the $\sin\gamma$ function has the value of ~ -1 in a wide range of K from ~ 1.1 A^{-1} to ~ 2.3 A^{-1} as the broken line shows. But, in the range between $K \approx 2.8$ A^{-1} and $K \approx 3.5$ A^{-1}, in which the first halo peak in the S(K) function occurs, the $\sin\gamma$ function is oscillatory and only with seven K values, 2.75, 3.07, 3.28, 3.47, 3.61, 3.74 and 3.86 A^{-1}, it becomes ± 1. The fringy contrasts observed in Fig.29 and Fig.30 are produced by the superposition of the phase contrasts formed by the reciprocal values near these K's and the {110} lattice periodicity, as mentioned before. On the other hand, in the case of $\Delta f = -1500$ A, the $\sin\gamma$ function is nearly -1 in a relatively narrow range of K values from ~ 2.7 A^{-1} to ~ 3.4 A^{-1}, as the full line shows, which covers almost the essential part of the first halo peak. The K values within this range together with the {110} lattice periodicity will produce the {110} lattice fringe contrast, the spacing of which is just the same as the {110} lattice one, in the centre part of the contour map. Furthermore, the intersection of them is expected to give the image contrasts corresponding to individual atoms belonging to the embryo core.

In order to obtain the lattice image corresponding to the projections of the embryo core atoms, the axial interference micrograph is calculated for the same embryo model as in Fig.29 with the

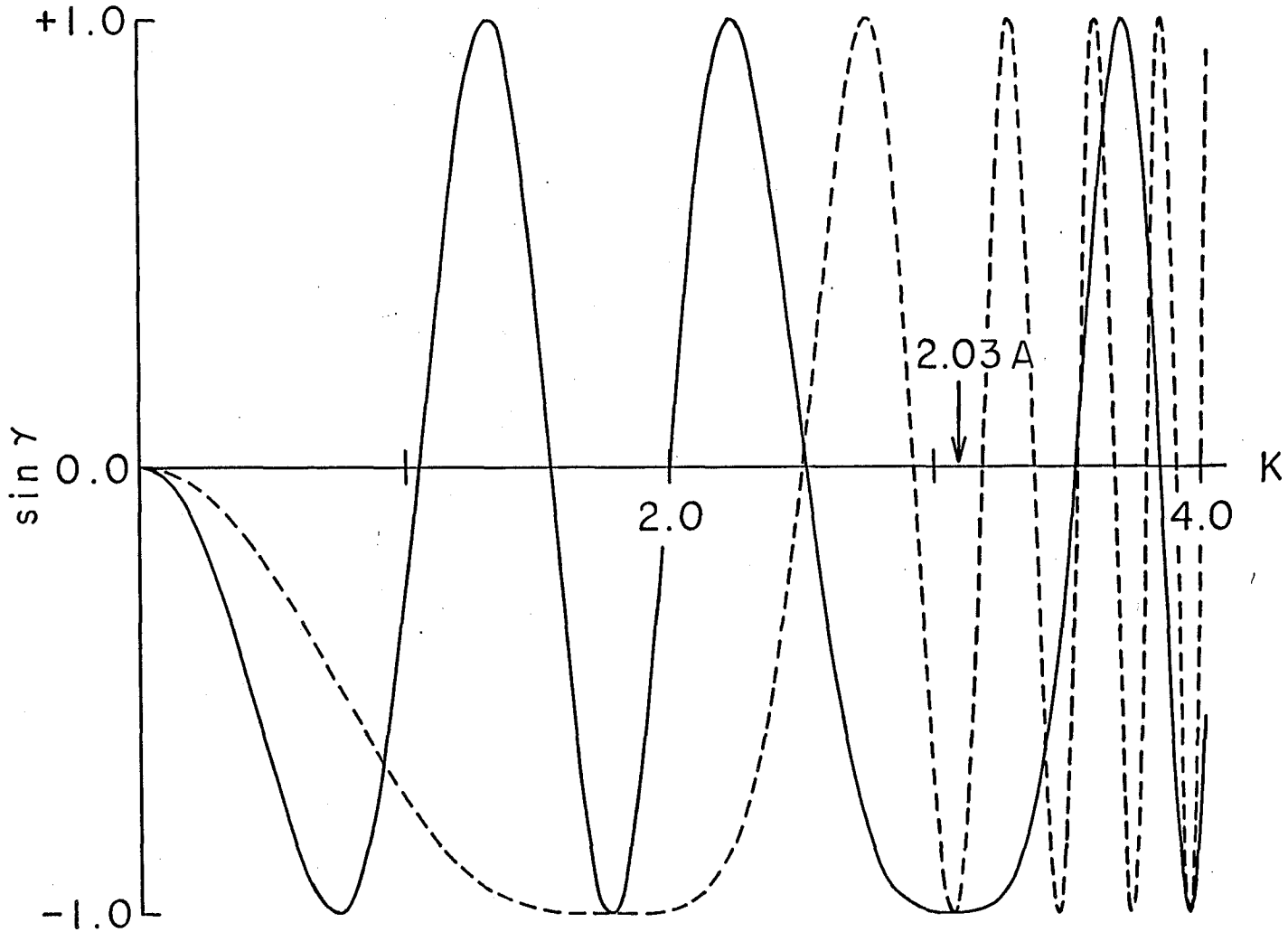

Fig. 32 The contrast transfer function, sinγ, vs the magnitude of scattering vector, K, for Δf=-500 A (broken line) and for Δf=-1500 A (full line).

defocus value, $\Delta f = -1500$ A, and is shown in Fig.33. The aperture configuration, the direction of the beam incidence and the size of the picture are just the same as in the before. On the image, the contours with the intensities higher than $I_B = 1$ are shown in full lines and the lower-value ones than $I_B = 1$ in dashed lines. The increment of the isointensity contour values is the same as in the figures so far presented. It can be seen from the figure that the higher contrasts appear like dots concentrated in the centre part of the contour map and they are gradually reduced with the distance from the centre. The calculated contrasts are observed over nearly the same region as the projection of the assembly, i.e. within a circle of 20 A in diameter, and are quite weak in its outside, which is considerably different from the appearance in Fig.29. It must be noted that the configuration and the geometry of high intensity dots contrast appearing in the centre part of the picture just correspond to those of atoms in the (001) plane of the b.c.c. structure. This fact is easily confirmed by comparing them with the nine circles represented by the broken lines in Fig.29, which are the projections of the embryo core atoms. It is, therefore, concluded that the dots contrasts in the centre correspond to the (001) lattice image of the b.c.c. embryo and that the defocus value, $\Delta f = -1500$ A, is the optimum one for the aperture configuration and the spherical aberration constant, $C_s = 1$ mm, employed in the present calculation. It is also worthy of noting that the lattice image contrasts are seen spreading out of the square region of about 10×10 A, although the projection of the embryo core is restricted to the square one of at most 7×7 A

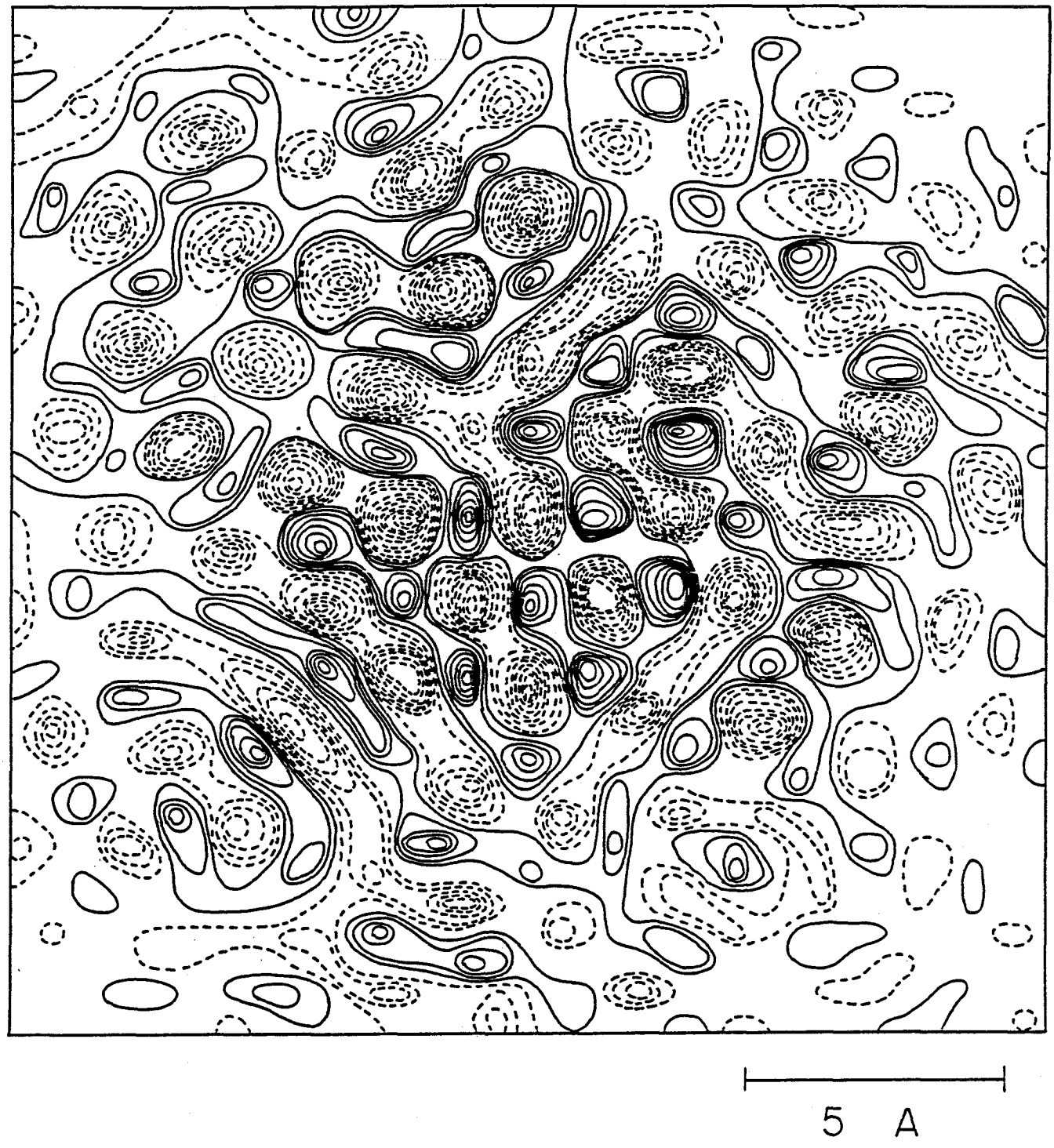

Fig. 33 The axial bright-field image calculated from the same embryo model as in Fig.29 with Δf=-1500 A. The direction of the beam incidence and the size of the picture are just the same as in Figs.29-31. Contours with I_B>1 are represented by full lines and those with I_B<1 dashed lines and their intervals are also the same as in Figs.29-31.

as shown in Fig.29. In the embryo model, the atomic arrangements of the outer part of each embryo (B in Fig.15) follow the b.c.c. structure to some extent, making a smooth connection between the embryo core and the outer disordered region. The size of the embryo (A and B in Fig.15) is about 10 A in diameter. Accordingly, the spreading of the lattice image might be rising from the outer transitional part of the embryo. On the other hand, since the image formation of the b.c.c. embryo core is based on the superposition of the diffracted waves from the atoms, the diffusing out of the lattice image might also be due to the diffraction effect.

In order to distinguish the embryo model from the DRP model in the calculated micrograph and to find the correspondence between the embryo and the lattice image in the experiments, the axial interference image of the DRP model is recalculated with the defocus distance $\Delta f = -1500$ A for the same scattering geometry and the same value of C_s as before. The resultant image is given in Fig.34. The dimensions of the picture are 12×20 A and its centre coincides with that of the figure 33. The isointensity contour values and their intervals are just the same as in Fig.33. It is readily seen in the calculated image that the high intensity dots contrasts, which is scarcely observed in the case of $\Delta f = -500$ A, appear, and the regularity in the configuration of them and fringe contrasts arising from the "crystal-like" alignment of atoms are missing. This feature is also observed in Fig.33 as the background noise in the area corresponding to the disordered region around the embryo. On the other hand, comparison between Fig.31 and Fig.34 shows that the value of the defocus distance essentially controls the image

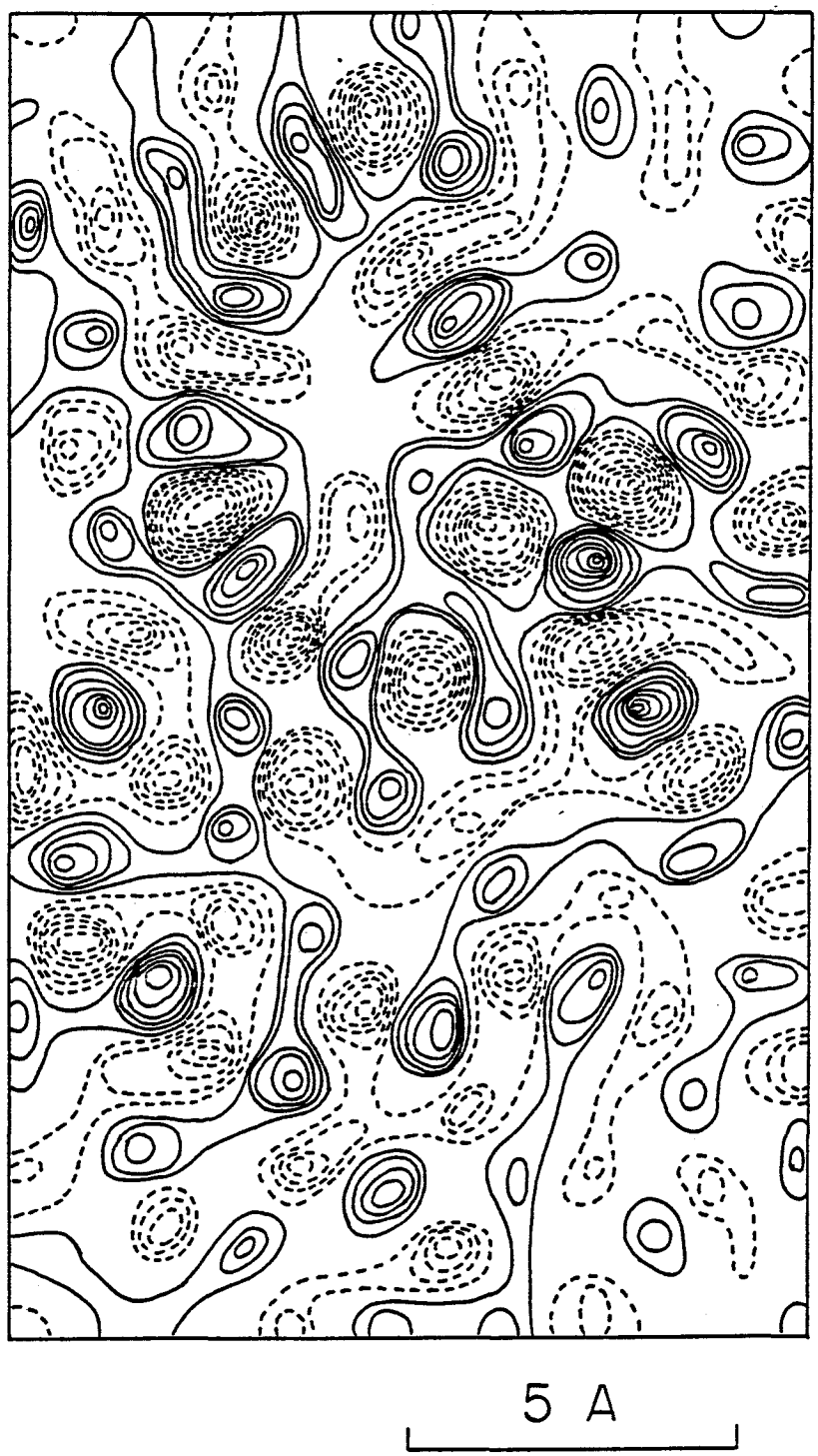

Fig. 34 The axial bright-field image calculated from the same DRP model as in Fig.31 with Δf=-1500 A. Dimensions of the picture are 12x20 A and its centre coincides with that of Fig.33. Isointensity contour values and their intervals are just the same as in Fig.33.

formation for the DRP model as well as for the embryo model, in which the iamge contrasts corresponding to individual atoms of the embryo core are produced. With this respect, it is considered that dots contrast in the figure could intrinsically coincide with the projected atom positions of the DRP structure. Actually, the correspondence between the contour map of Fig.34 and the map of projection of atom positions is fairly good.

4.3 Change of Lattice Image with Rotation of Model Assembly

In the actual experiment, the electron beam falls on the amorphous thin film at various angles against the axes of the ordered regions contained in it. The lattice fringes and/or the lattice image essentially appear only for the beam incidence along the restricted range of orientations of the b.c.c. embryo. The increase of the angle between the optical axis and the z-axis of the embryo will inevitably change the (001) lattice image, and at a particular angle, the calculated image will become so disturbed that it will be similar to that of the DRP model structure. Once the range of finding the lattice fringes and/or the lattice image is determined on the stereographic projection by the above process of rotation of the beam incidence, the content of the embryos, i.e. the medium range order regions, in the actual amorphous thin films could be quantitatively estimated.

In this section, the changes in the axial bright-field image contrasts are examined by rotating the model assembly relative to the incident beam direction in two ways. One is around the [110] axis of the b.c.c. embryo and the other is around the [010] axis. Generally, the rotation of the large crystal gives rise to unavoidable changes in the diffraction patterns. In the former, the intensities of $(\bar{1}10)$ and $(1\bar{1}0)$ diffraction spots decrease rapidly as a function of the rotation angle, $\theta_{[110]}$, while the (110) and $(\bar{1}\bar{1}0)$ spots persistently remain. On the contrary, all these diffraction spots suddenly disappear with the latter rotation, $\theta_{[010]}$. The assembly of the embryo model so far treated consists of a b.c.c. embryo and its surrounding disordered region of the DRP structure.

Therefore, the behaviour of diffraction spots with the rotaion of the model aggregate can be found among the diffracted intensity distribution, i.e. the first halo ring. It is easily conceivable that the (001) lattice image will be altered to the (110) lattice fringes when the assembly is rotated around the [110] axis of the b.c.c. embryo, and it will disappear with the rotation around the [010] axis, leaving only the image contrast characteristic of the DRP structure. Noteworthy is that the number of atoms belonging to the embryo core is as small as 15. This means that the {110} diffraction spots are considerably diffuse due to the reduced interference effect and have the three-dimensionally expanded intensity distribution in the reciprocal space. Therefore, the Ewald sphere will persistently intersect the swollen {110} diffraction spots, even if the z-axis of the b.c.c. embryo deviates from the optical axis to a large extent. This fact not only indicates that the (001) lattice image contrasts are gradually reduced with the rotation, but also suggests that its behaviour will be quantitatively explained in terms of the diffracted intensity from the embryo as a function of $\theta_{[110]}$ or $\theta_{[010]}$.

The changes of the diffracted intensity from the b.c.c. embryo with the rotation of the model aggregate are examined by calculating the $I(\mathbf{K})/N|f(k)|^2$ using Eq.(20). Especially, the maximum values of the $(\bar{1}10)$ reflection intensity changing with the rotations in the above two ways, which are shown in Fig.35, will be a good measure for the reduction of the lattice image contrast. The symbols, [110] and [010], in the figure indicate the axes, around which the model assembly is rotated. The height, $I_{max} \simeq 3.3$, represented by

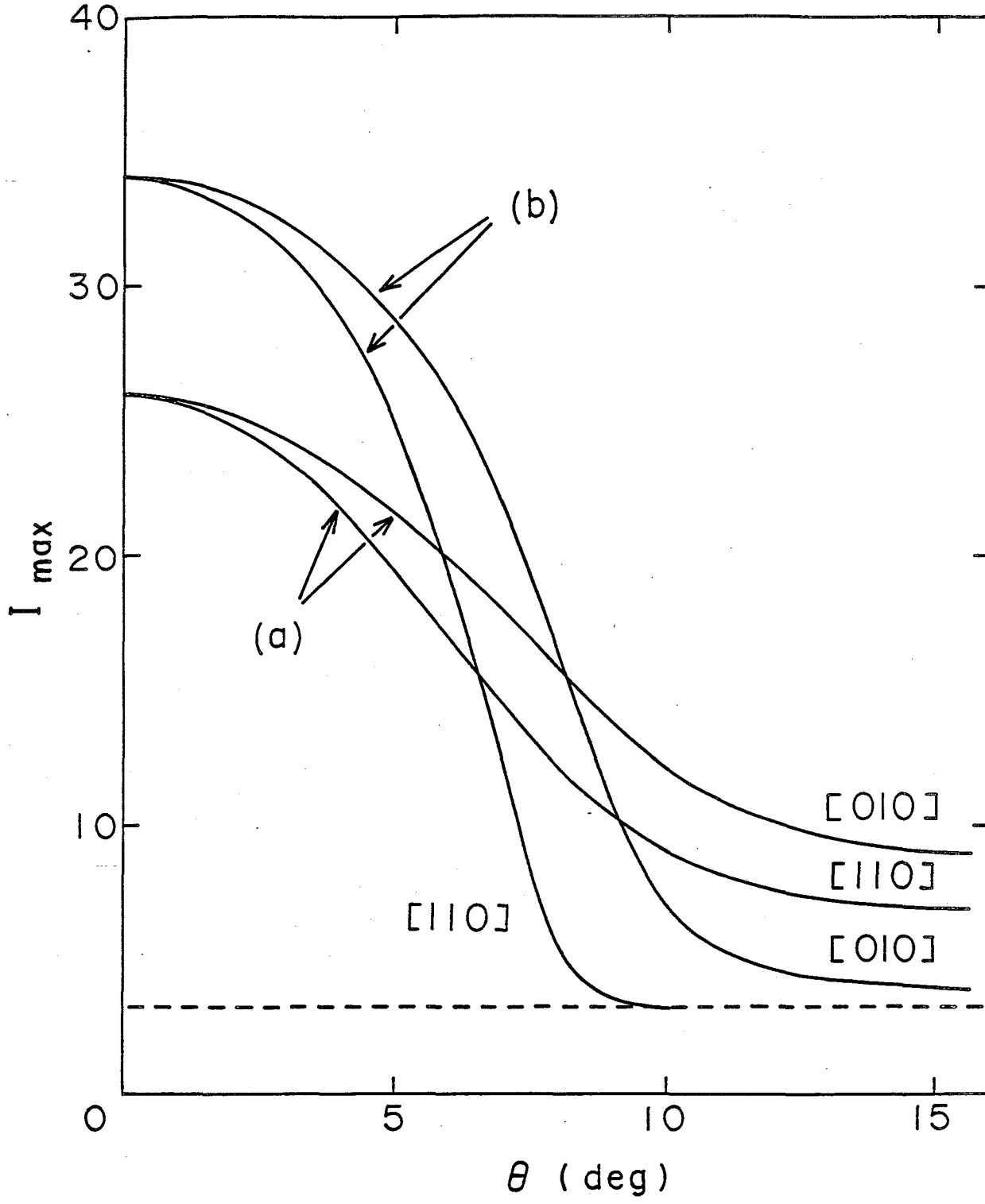

Fig. 35 The change of maximum value of ($\bar{1}10$) reflection intensity from the b.c.c. embryo with the rotation of model aggregate. The I_{max} curves, given by (a), are for the assembly containing a 15 atoms core cluster and those by (b) are for 51 atoms core cluster. The symbols, [110] and [010], indicate the axes of the embryo core, around which the model assembly is rotated by the angle θ.

the broken line corresponds to that of the first maximum of the S(K) function. The calculations are carried out for two kinds of aggregates of the embryo model. The curves of I_{max}, given by (a) in the figure, are for the aggregate containing a 15 atoms b.c.c. cluster and those by (b) are for a 51 atoms cluster, the calculated image of which is shown in Fig.30. The height of I_{max} at $\theta = 0°$ in the former is lower than that of the latter, because of the smaller embryo size. On the other hand, the decay of I_{max} of the former with the rotation angle is slower than that of the latter, not reaching the first maximum value in the S(K) even when the aggregate is rotated by 15°. This must be compared with the latter's values of I_{max}, which become 3.3 at $\theta = 9°$ and 15° in the case of [110] and [010] rotations respectively. This behaviour indicates that the $(\bar{1}10)$ diffraction spot in the former is much more diffuse owing to the reduced interference effect among the smaller number of correlated atoms resulting in the lower value of I_{max} $(\theta = 0°)$ and more persistent intersection of the Ewald sphere with the diffuse $(\bar{1}10)$ reciprocal lattice spot. In fact, the extension along [001] of the $(\bar{1}10)$ diffraction spot is three times larger than that in the latter, provided that its spread in the reciprocal space is proportional to $2\pi/w_{[001]}$, where $w_{[001]}$ is the dimension of the [001] stackings of embryo core atoms and $2\pi/w_{[001]}$ in the former in nearly 2.2 A^{-1}. From the geometrical analysis, the maximum value of the rotation angle, $\theta_{[010]}$, below which the Ewald sphere intersects noticeably with the expanded $(\bar{1}10)$ diffracted intensity distribution, is greater than that of $\theta_{[110]}$. Accordingly, the I_{max} value in the [010] rotation decreases more slowly with θ

than in the [110] rotation, as the figure shows. The above result of analysis strongly suggests that the lattice image as shown in Fig.33 will persistently remain in the calculated image contrast for considerably high values of θ, while its dimensions and correspondence with the projection of core atoms are gradually reduced with the rotation of the assembly. On the other hand, it is not always clear whether or not the lattice image is still visible when the I_{max} is only a few times greater than the spatially averaged value, 3.3. This is because the b.c.c. embryo core of 15 atoms is surrounded by the disordered region and by the rotation structural signals from the embryo of this size on the image will gradually fall into the background noise characteristic of the DRP structure. Accordingly, the axial bright-field images are calculated for various values of θ greater than 8°, and are shown in the following figures.

In Fig.36 are two examples of the axial interference images for the assembly, with a 15 atoms b.c.c. cluster rotated around its [110] axis by $\theta = 10°$ ((a)) and by $\theta = 15°$ ((b)) respectively. The setting values of C_s and Δf are 1 mm and -1500 A respectively, which are the same as in Fig.33 and Fig.34. The dimensions of the figures are just the same as those in Fig.34 and their centres coincide with that of the projection of the b.c.c. embryo. When the rotation angle is taken to be 10°, the dots arrangement corresponding to the embryo core atoms projections is slightly distorted and observed in a smaller area than that in Fig.33. Nevertheless, the area of finding the lattice image is still a little larger than that of the projection of core atoms. The [110] rotation up to

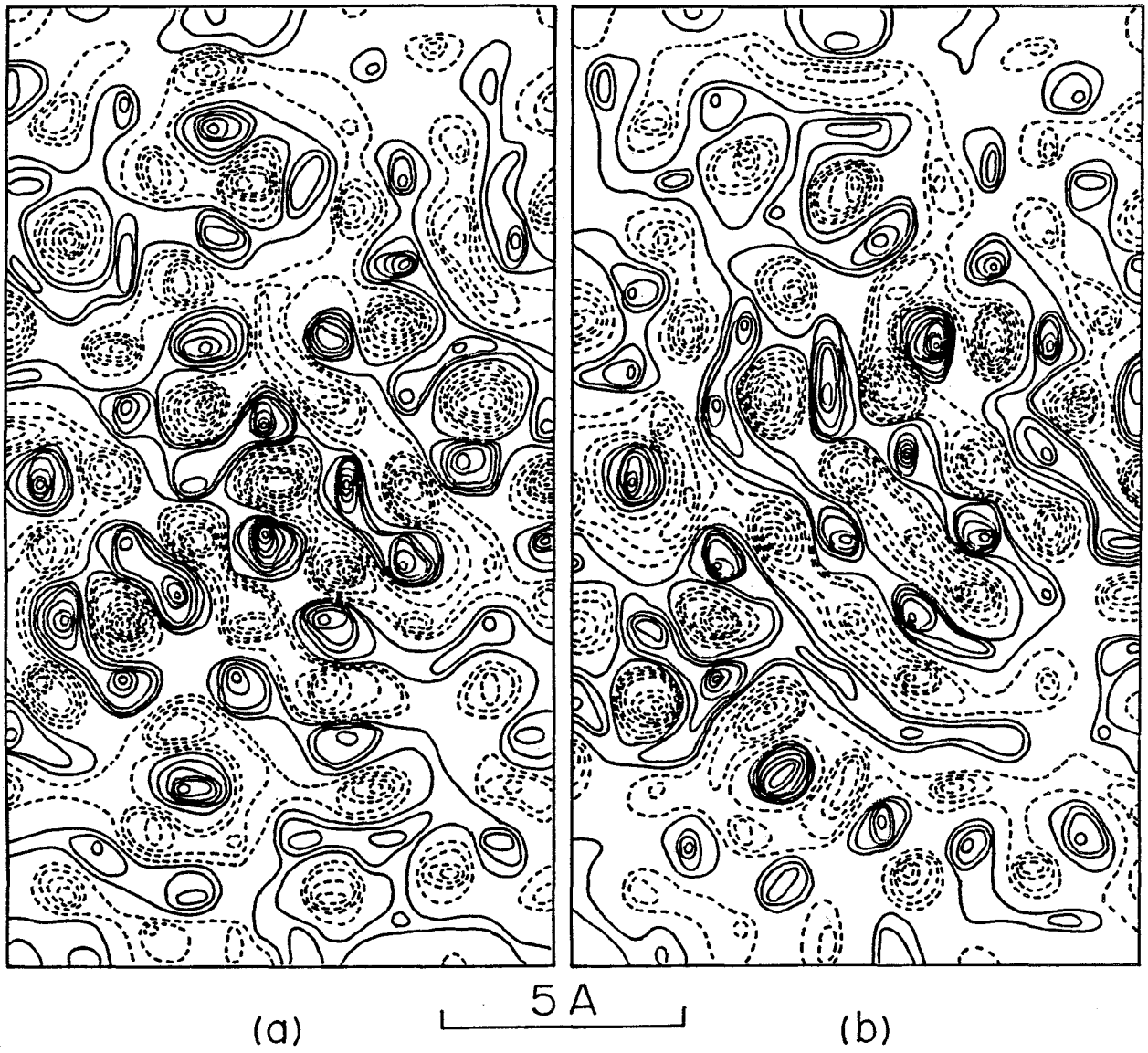

Fig. 36 Two examples of the axial bright-field images calculated with Δf=-1500 A for the assembly, with a 15 atoms b.c.c. cluster rotated around its [110] axis by θ=10° ((a)) and by θ=15° ((b)).

15° leads to a drastic change in the calculated image, as is given in the figure (b) where only three fringy spacings parallel to [$\bar{1}$10] of the b.c.c. embryo are seen in the centre part. The periodicity of the fringes is kept to be about 2 A, as in Fig.33, which is very close to the {110} lattice spacing. Since the direction of the fringes is perpendicular to the rotation axis and their spacings are not changed, it is concluded that the fringy contrast is no other than the lattice fringe arising from the b.c.c. embryo. Compared with the image in the figure (a), the dots in the lattice fringes are weaker and their correspondence to the atom positions in the embryo core is poorer.

The effect of the rotation around the [010] axis of the embryo core on the calculated image of the same model as in Fig.36 is readily seen in Fig.37, in which (a) and (b) correspond to $\theta = 9°$ and $\theta = 12°$ respectively. In this case, the (110), ($\bar{1}$10), (1$\bar{1}$0) and ($\bar{1}\bar{1}$0) reflections from the b.c.c. embryo deviate from the Bragg condition at the same time with rotation. Therefore, the disintegration of the lattice image will be faster than in the case of [110] rotation and {110} fringes are not expected. Actually, the dots arrangement is partially visible even in the figure (a) with $\theta = 9°$ but more irregular than that in Fig.36(a), and in the figure (b), which has the rotation, $\theta = 12°$, the lattice image is not recognized and the appearance of the dots contrast is very similar to that of the DRP model structure in Fig.34. No fringy contrasts are seen in Fig.37.

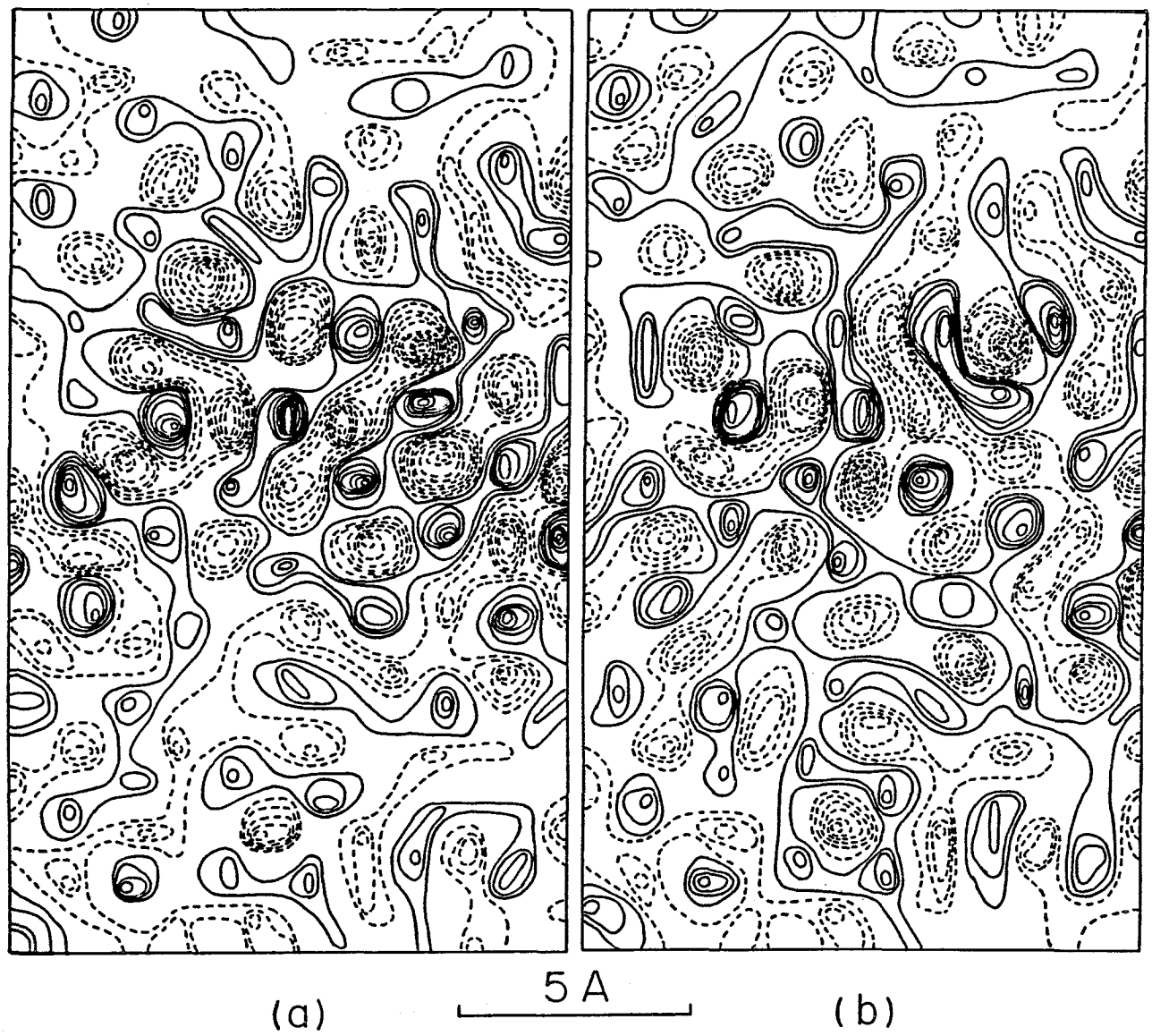

Fig. 37 The effect of the rotation around the [010] axis of the embryo core on the calculated images of the same model as in Fig.36: (a) with θ=9°, and (b) with θ=12°.

4.4 Image Contrast from a Thick Specimen Containing Two Embryos

Since the model assemblies so far studied have the thickness of 20 A, the calculation ie extended to the case of thicker specimens which would be more similar to the actual experimental conditions. Therefore, the interference image from the model assembly of the total thickness of 40 A is examined by stacking up two different spherical aggregates one over the other. The direction of the beam incidence is chosen to be along [001] of the b.c.c. embryo contained in one of these two aggregates. Since the kinematical approximation gives the image contrast by single scattering from individual atoms, the calculated lattice image will persistently remain against the increase of the thickness of the model assembly. When a DRP aggregate is stacked on that of the embryo model, it is easily imagined that the lattice image will be not largely perturbed by the background noise from the DRP structure. In the case of stacking of two different embryo model aggregates, more complicated changes are expected: When the z-axes and the atomic projection of the two embryos almost coincide, the lattice image will not be altered, and, when the z-axis of the second embryo deviates from the Bragg condition to a large extent, the resultant lattice image will be quite the same as in the above case of the DRP aggregate, since the second embryo does not contribute to the lattice image formation. The latter case is shown in Fig.37(b). The most striking effect arises from the stacked two embryos with unoverlapping atomic projections and yet producing the lattice image contrasts simultaneously. This is easily achieved by introducing a lateral displacement between the two aggregates by keeping

their z-axes parallel with each other. In this case, the positions and the intensities of dots contrast will be gradually changed with increasing the displacement. For instance, the lattice image will disappear, when the displacement is taken to be a/2·[100], where a is the lattice parameter. The rotation around the z-axis between the two model aggregates will bring about a similar effects. As an example, the image contrast of two stacking model assemblies each containing an embryo is calculated by inclining the (010) plane of one embryo by 9° and rotating it around its z-axis by 40°. The effect of inclination by 9° to the lattice image contrast formation is already shown in Fig.37 (a), and the resultant interference image exhibits a slightly deformed (001) lattice image rising from the uninclined embryo. From the above consideration of the effect of the film thickness, the inclination of [001] axis of the embryo, and the image overlapping of the embryos, the ultimate visibility and probability of the lattice and fringe contrasts of the medium range order regions in the actual amorphous alloys will be discussed in the following chapter.

5. DISCUSSION AND CONCLUSIONS

5.1 General Discussion on Crystalline Embryo Model

Since Bernal's[2] first static model of the dense random structure, a number of structural models for amorphous metals and alloys based on the concept of the DRP have been proposed and the results of many x-ray diffraction experiments seem to have been satisfactorily explained. However, some newer experimental results strongly suggest that the chemical short range order or even farther range atomic order extending beyond the first neighbour distance may exist in the actual amorphous structure, which is hardly expected from the DRP models. Similar short range or even farther range ordering has been found in the liquid structure of Pd-Si and Fe-B alloys by the neutron diffraction[10,11,94] and also in the supercooled liquid structure, for instance, in supercooled Bi by electron diffraction.[90]

From the thermodynamical consideration and calculation, Fujita[28,29] concluded that the short range and medium range order may exist already in the liquid structure as the quasi-crystalline clusters with sub-critical size and dynamically fluctuating, of which the number, the average size and lifetime will increase as the liquid is supercooled. By the rapid quenching from the melt, they will be frozen as the static crystalline embryos together with the disordered region and ultimately compose the amorphous structure. It was suggested that a great number of the intermediate size clusters including atoms from 10 to 40 in number would appear, giving rise to the medium range order in the amorphous structure.

Taking such high degree of atomic ordering into consideration, the present author and Fujita[3] have proposed a simple and possible structural model of amorphous metals and alloys, which is named the crystalline embryo model, consisting of the crystalline embryos and the disordered boundary region which coexist and continuously and smoothly connect to each other. They also constructed the model assemblies for amorphous Fe-B alloys, assuming that the b.c.c. embryos and the chemical clusters of Fe_3B type coexist in the dense disordered structure in accordance with the Mössbauer experiment by Oshima and Fujita.[26] Thus obtained crystalline embryo model satisfactorily reproduces the diffraction functions and the high resolution electron images from the medium range order clusters in the disordered structure, when the embryo size is taken to be as small as 10 A in diameter, which corresponds to some twenty atoms cluster including a part of the transition region. Therefore, it is concluded that the quasi-crystalline clusters of this size most probably exist in the real amorphous structure.

The DRP model has succeeded in the reproduction of the S(K) and G(r) functions of the amorphous metals of single element. However, many investigators showed that amorphous pure metals films obtained by the vapour condensation always contain gaseous atoms or metalloid atoms to a large extent, which seems to be indispensable to hold the amorphous structure. This fact implies that the dense random packing of identical spheres does not always lead to a realistic amorphous structure. Moreover, throughout the investigations concerning such diffraction functions, mostly done by computer calculations, it has been realized that the dense random packing of

spheres does not necessarily give a desirable intensity distribution in S(K) function in the case of binary amorphous alloys, especially as regards the height of the first halo peak. This reflects that the actual amorphous alloys have a degree of order in the atomic arrangements higher than that in the DRP model. Graczyk and Chaudhari[70] calculated the axial interference images of the DRP model structure by using the kinematical approximation and introducing the contrast transfer function. The calculated image showed a vague fringy contrast in a certain case, the spacings of which are much greater than the crystalline interplaner ones. They ascribed the fringy contrast to the structural anisotropy in the DRP model structure. Since the dots contrast in the image from the DRP model structure appears as in the figure 34, corresponding to the density fluctuations on the projected plane of atoms, their result must be a rare case and it can scarcely be expected to obtain the lattice like fringe contrast from the DRP structure. It is worthy of note that in the HREM the image contrast from the perfectly random structure will be flattened with the increasing film thickness, giving rise to a structureless "whiteout" micrograph. Therefore, the DRP model, which does not take the medium range order into consideration, can not satisfactorily describe the observed lattice and fringy images from the amorphous structure.

Taking account of only the chemical short range order, the chemical cluster model has been proposed for the amorphous alloys containing metalloid atoms close to the crystalline chemical compound compositions. Gaskell[72] constructed a model for the amor-

phous $Pd_{80}Si_{20}$ alloy based on the random packing of trigonal prismatic units. The structure was relaxed using a Lennard-Jones 6-12 potential, with some additional constraints included to preserve trigonal prismatic coordination. The computed G(r) was, then, convoluted with Gaussian broadening functions which simulate the effects of thermal vibrations and transformation of reciprocal-space data, S(K), over a limited spectral range. The calculated G(r) and S(K) were found to give a good representation of the experimental neutron scattering data measured up to high K value, 30 A^{-1}. However, the fine structure in the second peak in the G(r) was not fully reproduced. Moreover, it is still questionable whether the density of thus obtained chemical cluster model fits to the experimental one. Kobayashi et al.[73] also constructed a model structure of the amorphous $Fe_{75}P_{25}$ alloy. The building algorithm consisted of a random packing procedure ensuring the agreement of its packing fraction with the experiment and a relaxation using a non-spherically symmetric interatomic potential for Fe-P pairs, which was assumed to stabilize a trigonal prismatic unit similar to that found in the crystalline Fe_3P. However, it has not been clarified to what extent chemical ordering in these model aggregates after the relaxation remains or develops.

One approach for reproducing the absence of long range order in the amorphous structure can be described in terms of microcrystalline model, in which the S(K) function is fully represented by that of a microcrystallite and no correlations with its surroundings exist. Although the calculated S(K) function by using Eq.(1) exhibits the diffuse peaks because of the small crystal size, the

peak profiles, ratios and positions in it does not fit the experimental ones. In order to improve the model S(K) function, effects of thermal and static displacements of atoms from their equilibrium positions are incorporated into its each peak by multiplying the Gaussian broadening function. However, since no isolated microcrystallites exist in the amorphous structure but they are always jointed together through the grain boundary, the S(K) function of a microcrystallite will be modified by the intercrystalline interference effect. In this respect, it is shown and fully discussed in the subsection 2.1.2 that the microcrystalline diffraction theory is not applicable to the amorphous materials.

A fairly different approach to understand the amorphous structure was made by Koizumi and Ninomiya,[86] who constructed a dislocation model of the amorphous structure, in which many screw dislocations were introduced in a f.c.c. lattice in order to produce local disordered structure and destroy its long range order. The final atomic positions were obtained by the relaxation of the dislocated structure using the Morse-type interatomic potential. For the dislocation density of 1.1×10^{15} cm^{-2} or 4.3×10^{14} cm^{-2}, the calculated pair correlation function was found to be in good agreement with the experiments as well as in other models. The correspondence between their and the present models could be given by an interpretation such that the embryo regions, where the lattice structure is relatively well kept, may correspond to the lattice domains separated by dislocations in their model and their disordered dislocation cores may correspond to the boundary regions between neighbouring embryos in the present model. This interpretation

gives us more or less the same size of the embryos or medium range ordered regions in the both models.

Ninomiya[85] has pointed out that many of the Bernal's polyhedra can be reproduced by putting dislocations in the closest packing crystal structure. In this respect, the DRP polyhedra and the crystalline polyhedra, which have been proposed by Fujita[88] and are found in the core of the crystalline embryos, must be closely connected specially by perfect dislocation core structure and half dislocation structure associated with the stacking fault. Ashby et al.[103] have shown that the crystal boundaries of simple metals can be described completely and uniquely as nesting stacks of eight kinds of the basic polyhedral holes or "canonical holes". Since the positions of atoms in the transition regions are strongly affected by the atoms of neighbouring crystalline embryos in the present model structure, the connectivity and the conjugate structure of the transition regions and disordered boundary regions could be analysed in terms of the defective crystalline polyhedra.

In order to see the packing of atoms in the transition regions, the types of Voronoi polyhedra are studied by using the b.c.c. embryo model of single element. These polyhedra provide a means not only for defining the average number of geometrical neighbours but also for determining the nearest neighbour configuration of each atom. For example, in Fig.38(a) are shown the Voronoi polyhedra of the crystalline f.c.c. lattice and non-crystalline icosahedral arrangement of 13 atoms. Although both polyhedra have the same number of faces, N = 12, the former is facetted by twelve quadrangles, which is expressed as (0, 12, 0, 0),

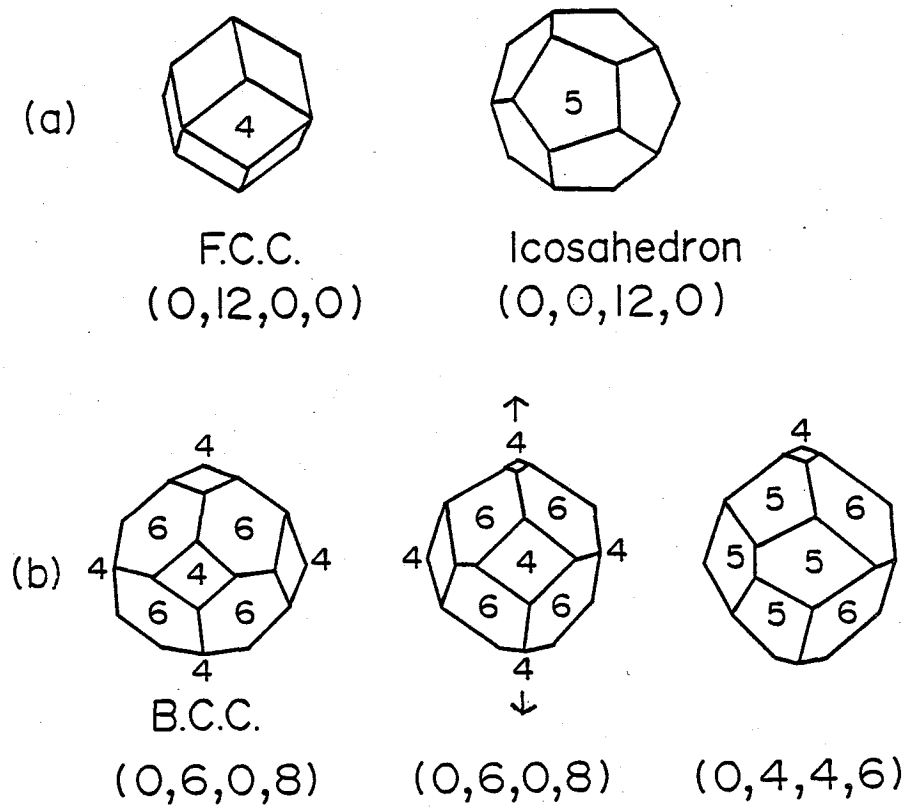

Fig. 38 The Voronoi polyhedra: (a) Voronoi polyhedra of the f.c.c. lattice and non-crystalline icosahedral arrangements of 13 atoms, and (b) the changes of Voronoi polyhedra produced by the distortion of the b.c.c. lattice.

Table I The types of Voronoi polyhedra appearing for each atom in the transition regions, which are classified according to the number of facets from N=12 to N=14.

N	Voronoi polyhedra
12	(0,4,4,4) (0,4,6,2) (0,6,4,2)
13	(0,5,2,6) (0,5,4,4) (0,6,4,3)
14	(0,6,2,6) (0,5,4,5) (0,6,4,4) (0,7,2,5)

and the latter by twelve pentagons, which is also expressed as (0, 0, 12, 0)*. In Fig.38(b) are shown the changes of Voronoi polyhedra produced by the distortion of the b.c.c. lattice. The Voronoi polyhedron of the b.c.c. lattice is facetted by six quadrangles and eight hexagons, i.e. (0, 6, 0, 8) and N = 14, as shown in the left hand side of the figure. As the b.c.c. lattice is stretched along its z-axis, the shape of the polyhedron is gradually transformed from (0, 6, 0, 8) to (0, 4, 4, 6), which is shown in the middle and the right respectively in the same figure. Baker et al.[49] investigated local atomic arrangements in their DRP model structure in terms of Voronoi polyhedra and found an increase of the 13 atom icosahedral arrangement with the relaxation process. Yamamoto and Doyama[61] also showed that the populations of non-crystalline polyhedra with the five-edged facets such as the (0, 0, 12) type were largely increased with the relaxation, while the frequencies of crystalline ones of the (0, 4, 4) type were reduced. In the embryo model, many types of Voronoi polyhedra reflecting the b.c.c. structure such as the above (0, 4, 4, 6) polyhedron appear for each atom in the transition regions and they are classified according to the number of facets from N = 12 to N = 14, which is shown in the Table I. The above fact indicates that the positions of atoms in the transition regions are strongly affect-

---

* The notation, (p, q, r, s), means that the polyhedron has p triangular facets, q quadrangular facets, r pentagonal facets and s hexagonal facets. The possibility of appearance of septangular facets is omitted from the expression.

ed by the inner neighbour atoms belonging to the b.c.c. core in accordance with the results given in Fig.11. It must be noted that the partial S(K) function obtained from the transition regions shows the characteristic splitting of the second halo peak, as given in Fig.18(b) and (c). In the case of the embryo model for the amorphous Fe-B alloys, boron atoms are expected to occupy either the interstitial-like or substitutional-like sites and more or less disturb the crystalline nature in the outer part of the embryo.

The DRP models of the amorphous Pd-Si, Fe-P and Fe-B alloys were examined in relation to the short range order of their atomic structure by Boudreaux and Frost.[69] The types and numbers of near-neighbour atoms were calculated in detail, from which it was argued that a specific coordination was preferred and satisfied by a local unit structure around each metalloid atom. Furthermore, the local geometry was examined by computer graphic methods and it was discovered that the two local geometries dominated the surroundings of metalloid species; the octahedron and the trigonal prism. In the crystalline embryo model for the amorphous Fe-B alloys, these structural features are taken into account in the disordered boundary and the transition regions: In the case of the $Fe_{75}B_{25}$ amorphous alloy, the Fe_3B type chemical order clusters, each consisting of some trigonal prism units, are put in the boundary regions by about 10 % in total fraction in accordance with the result of the experimental analysis of the Mössbauer spectroscopy.[26] Their effect on the diffraction functions will be discussed in the next section, but the high resolution image contrast from them is not calculated in this thesis.

5.2 X-ray Diffraction of Amorphous Metals and Alloys Containing the Medium Range Order

In the sebsection 2.1.2, it is shown that the S(K) function of a b.c.c. microcrystallite is considerably changed when a twin boundary is introduced. The S(K) function becomes more diffuse owing to the break down of the normal crystalline periodicity at the twin interface and the interference intensity rises up at around $K = 6.2\ A^{-1}$, where a high angle side shoulder of the second halo peak is usually observed in the diffraction pattern of amorphous metals and alloys. Atoms in one side of the twin interface have a special configurational relation with those in other side different from the crystalline periodicity, which makes particular phase differences and inevitably changes the S(K) function around $K = 6.2\ A^{-1}$. This not only emphasizes that the microcrystalline diffraction theory, in which the S(K) function is assumed to be fully represented by that of an isolated microcrystallite, is not applicable to the amorphous materials, but also strongly suggests that an assembly of atoms consisting of the crystalline embryos and the disordered boundary regions connecting them could give a reproduction of the characteristic diffraction intensity distribution. Actually, the S(K) functions calculated from the b.c.c. embryo model is in good agreement with so far obtained experimental ones. When the atoms in the transition regions and the disordered regions in the vicinity of embryos are taken as centres, and the radial distribution around them and the partial G(r)'s are examined, the partial S(K) functions obtained by the Fourier transformation of the parial G(r)'s show the splitting of the second halo

peak. Therefore, it is concluded that tolerably sharp intensity distribution of the first halo peak is due to the effect of the intracrystalline interference in each embryos and the splitting of the second halo peak results mainly from that of the interference between atoms in the embryos and those in the disordered boundary regions.

In the case of the f.c.c. embryo model, although the G(r) function is in fairly good agreement with that calculated from the experimental data, the considerably high first peak suggests that the f.c.c. crystalline periodicity persistently remains in the transition part around the f.c.c. embryo core consisting of 19 atoms after the relaxation. Doi[104] made a careful Fourier analysis of the first halo peak of the S(K) function to obtain the variation of the direct neighbour distance in linear atomic arrangement in the amorphous structures. He concluded that there are regularly spaced atomic rows of two atomic distances in the amorphous $Pt_{20}C_{80}$ structure and suggested the existence of microcrystals constituted of 13 atoms arranged in regular f.c.c. or h.c.p. lattices. Accordingly, the f.c.c. embryo core size in the present model might be still slightly large. Suzuki et al.[10] showed that the appearance of the G(r) function strongly depends on the magnitude of maximum scattering vector, K_{max}, which is given in Fig.2. In the case of K_{max} = 25 A^{-1}, total radial distribution functions with high real-space resolution of the amorphous Pd-Si alloys displayed definitely a second peak splitting into three subpeaks,[10,11] as mentioned in the subsection 1.2.1. In this respect, the calculated S(K) function of the f.c.c. embryo model reproduces the similar profile in

the second maximum. This fact suggests that the medium range order with the f.c.c.-like atomic arrangement may exist in the Pd-Si alloys in addition to the chemical short range order of Pd_3Si type. Actually, Hirotsu and Akada[33] have observed regular arrangements of dotty contrasts, which could be explained by the f.c.c.-like medium range order.

In the embryo model of single element, the embryo size suitable for the reproduction of experimentally obtained diffraction functions can not be fully determined, since the model structure is not necessarily realistic in the sense that it does not contain metalloid atoms indispensable to hold the amorphous structure, as discussed later. However, it is considered from model calculations that the core part of the embryo of optimum size contains atoms from 10 to 20 in number in accordance with the prediction based on the thermodynamical consideration and calculation by Fujita.[88,89] It should be noted that Koizumi and Ninomiya[86] put a large ammount of dislocations into a model crystal so as to produce a disordered structure like amorphous materials. It is supposed that such a model structure, where dislocations are separated by only about three atomic distances, retains the crystalline ordering to a large extent around every dislocation core. In this respect, the dislocation structure would not be quite different from the embryos cemented by the disordered boundary region. This interpretation gives us more or less the same size of the embryos or medium range ordered regions in both models.

Early efforts to form amorphous metallic solids involved evaporation of metals in vacuum and condensation of their vapours on

a substrate maintained at low temperature. Problems of contamination by condensation of residual gaseous atoms together with the metal atoms on the cold substrate are severe. Some nominally pure metals have been prepared by this technique in the amorphous form, although definitive scattering experiments were often not carried out and the amorphous nature of the deposited films was sometimes deduced only from high residual resistances which decreased abruptly and irreversibly with increasing temperature, the decrease being attributed to the crystallization. The crystallization temperatures of nominally pure amorphous films of nickel and cobalt were reported to increase with increases of the residual gas pressure during evaporation.[105] According to a low temperature electron diffraction experiment by Yoshida and Fujita,[106] it was shown that the structure of amorphous iron films vacuum-deposited on the cold substrate was stabilized by the occluded gaseous atoms, mainly oxygen atoms. Irrespective of the methods of production, amorphous iron films always contain gaseous atoms or metalloid atoms to a large extent, which are indispensable to compose the amorphous structure. In the b.c.c. embryo model, the S(K) function is in agreement with so far obtained experimental curves of various amorphous metals and alloys, but relative positions and intensities of halo peaks still slightly differ from experimental ones. It is also reflected in the G(r) function, which does not always fit the curves obtained from the diffraction data. Without the metalloid atoms, the packing structure of the disordered regions and the transition regions will not necessarily be realistic and the crystalline periodicity in the embryos will be stronger than that

expected from the real structure, which will give rise to disagreements with experiments in the peak profiles, ratios and positions in the G(r) function. Actually, when the metalloid atoms are missing, the connectivity and the conjugate structure of the transition regions can be analysed in terms of the defective crystalline polyhedra and the positions of atoms surrounding each embryo are strongly affected by atoms of the crystalline embryo. Therefore, in order to construct the more realistic boundary layer and embryo structures, it is quite necessary to introduce in the structure the foreign atoms. They will occupy either the interstitial-like or substitutional-like sites and more or less disturb the crystalline nature of the amorphous structure. This disturbance is further enhanced by the chemical bonding between metallic and metalloid atoms. As mentioned in the section 3.4, the modelling and calculation for amorphous Fe-B alloys are extensively improved by taking account of the boron atoms and the G(r) and S(K) functions are successfully compared with those experimentally obtained as follows.

In the composite type embryo models for the amorphous Fe-B alloy the b.c.c. embryos and chemical clusters of Fe_3B type coexist surrounded by the disordered regions in accordance with the experimental result by Oshima and Fujita.[26] In the calculation of the diffraction functions, a new process of Fourier transformations, which takes account of the truncation effect, is successfully applied as described in the section 3.3, and a meaningful comparison and good agreement are obtained between the calculated interference and pair correlation function and so far obtained ex-

perimental ones. Therefore, it is concluded that the crystalline embryo model, which takes the medium range order into account, satisfactorily describes the amorphous structure. It must be pointed out that the effect of the b.c.c. crystalline periodicity on the profile of the two functions disappear, when the embryo size is taken to be as small as 10 A in diameter corresponding to some twenty atoms cluster including a part of the transition region and the Fourier transformation is truncated at $K_{max} = 15\ A^{-1}$ in accordance with the x-ray scattering measurements,[11.21] as Figs. 21 and 22 show. It is also noteworthy that the Fe-B distance plays an essential role in reproducing the profile of the split second peak in the G(r) function, as is described in the section 3.4. Further consideration in relation with the chemical state of boron stoms in the amorphous structure will be given later.

Suzuki et al.[10] showed that the appearance of the radial distribution function strongly depended on the maginitude of maximum wave vector K_{max} where the Fourier transformation from the S(K) to the G(r) was truncated. They concluded that the value of $K_{max} = 25\ A^{-1}$ is necessary to obtain a total correlation function with high real-space resolution, which displayed definitely a separation between Pd-Si and Pd-Pd partial pair correlations in the nearest neighbour region and a second peak splitting into three suppeaks, as shown in Fig.2. As mentioned before, in the x-ray diffraction measurements for the amorphous Fe-B alloys, the scattering data are limited to relatively small scattering angles ($K_{max} = 15 \sim 17\ A^{-1}$), which inevitably gives rise to a poor resolution of the pair correlation function. An example is already given by Fig.19, where a

theoretical interference function is Fourier-transformed using Eq. (14) with two values of K_{max}, 15 A^{-1} and 30 A^{-1}, respectively, and it is comfirmed that the truncation of the S(K) severely controls the quality and spatial resolution of the G(r). This indicates that the plausibility of the model is not always guaranteed by the direct comparison between the experimentally obtained G(r) and the model G(r) which is not subjected to the truncation effect, as discussed in the section 3.3. In order to make the more meaningful comparison with the experiments, therefore, a new process of Fourier transformations, which is equivalent to that employed in the analysis of the experimental x-ray diffraction data, is successfully applied in the present thesis to the crystalline embryo model for the amorphous Fe-B alloys. In the G(r) function of the crystalline embryo model for the amorphous $Fe_{86}B_{14}$ alloy, some small peaks arising from the b.c.c. structure of the 27 atom embryos are seen in the second peak in the case of $K_{max} = 30\ A^{-1}$, as shown in Fig.19. This phenomenon resembles to the variation of the shape of the second peak of G(r) depending on the K_{max} value in the experiment by Suzuki et al. Therefore, it is concluded that to discuss satisfactorily the structure of the amorphous Fe-B alloys, especially regarding the medium range order, the high K value measurements of scattering intensity distribution are quite necessary.

Boudreaux[65] and Fujiwara et al.[66] constructed models for the amorphous Fe-B alloys based on the concept of the relaxed DRP of spheres. In their modelling experiments, the ratio of the diameter of boron atoms to that of iron atoms was taken to be 0.52, which is smaller than 0.59 which corresponds to $r_{0Fe-B} = 2.05$ A in the present

study. When these ratios are employed, the peak height ratio of the second peak doublet in the G(r) is of the reversed type both in the embryo model and the relaxed DRP model for the amorphous Fe-B alloys with 14 to 25 at%B. In this respect, the G(r)'s for the amorphous $Fe_{80}B_{20}$ and $Fe_{75}B_{25}$ alloy do not fit the experimentally obtained curves.[11,21] According to the result by Fukunaga et al.,[11] the G(r) showed the "normal" second peak splitting even for boron concentrations of less than 20 at% (Fig.3(b)) contrary to that by Waseda and Chen,[21] as mentioned in the first chapter of the present thesis. A neutron diffraction measurement on the amorphous $Fe_{83}B_{17}$ alloy by Cowlam et al.[22] confirmed the observation in the above. Recently, Lamperter et al.[16] showed that the average Fe-B spacing was 2.14 A in the structure of the amorphous $Fe_{80}B_{20}$ alloy. The average distance, 2.05 A, employed before is taken from the crystal structure data on the Fe_3B and does not necessarily correspond to the realistic one in the amorphous structure of the Fe-B alloy. Therefore, the improvement of the model calculation is carried out by introducing the above measured value into r_{0Fe-B} provided that the average Fe-B spacing has the same value for the $Fe_{100-x}B_x$ (x=14, 20 and 25) alloys. As a result of the calculation, as shown in Figs.26 and 27, the second peak splitting in the pair correlation functions for three alloys is drastically changed from "reversed" to "normal", which is in accordance with the x-ray and neutron data.[11,16,22] In this case of r_{0Fe-B} = 2.14 A, the ratio of the diameter of boron atoms to that of iron atoms is 0.66. The normal type splitting, regarding the shape of the second peak, was also observed in the relaxed DRP model for

the amorphous Fe-P alloy by Boudreaux[65] and Fujiwara and Ishii,[67] in which the ratio of phospher diameter to iron diameter was taken to be 0.72. The above results of the model calculations for the amorphous Fe-P and Fe-B alloys clearly indicate that the shape of the second peak in the G(r) is strongly influenced by the average distance between metal and metalloid atoms. Dini et al.[23] made a comparison between two independent x-ray determinations[11,21] of the structure of the amorphous Fe-B alloy which were in disagreement, specially regarding the shape of the second peak of the G(r). They suggested that some of the disagreements in the S(K) curves could arise through structural differences in the samples, which were related to their state of quench. However, it was not concluded what sort of changes were produced by the enhanced annealing and thereby the structural relaxation in the twin-rolled samples. The present result suggests that two values of the average Fe-B spacing, $r_{0_{Fe-B}}$, would correspond to the structural differences in the amorphous Fe-B alloy with boron content below 20 at%. This might also indicate the difference of the degree of chemical bonding between iron and boron atoms in the actual amorphous structure including the boundary regions and chemical embryos.

5.3 High Resolution Electron Image from the Medium Range Order

In parallel with diffraction experiments, the structure of amorphous materials has been studied by the HREM, which could provide more direct and detailed information of the local atomic structures than the statistically averaged data such as the S(K) and G(r) functions.

Some investigators observed the lattice like fringes or dots of about 10 A in diameter locally even in the as quenched amorphous materials under the condition of axial illumination. This results seem to be in good agreement with the prediction of the crystalline embryos surrounded by the disordered regions in the amorphous structure and with the model calculation of the high resolution electron image contrast from the thin film of an iron based amorphous alloy. When the defocus distance is chosen as -1500 A and the spherical aberration constant as 1 mm in the calculation, the lattice like fringes and dots with the spacings of about 2 A and the diameter of about 10 A are well reproduced, as mentioned and discussed in the chapter 4.

In the kinematical approximation used in the present calculation, the image contrast formation is based on the interference between the directly transmitted waves and the scattered ones, and the phase shift between them is inevitably modulated by the aberration and the defocussing, as Eq.(16) shows. The oscillations of the contrast transfer function, $\sin\gamma$, in Eq.(19) result in the reversal or suppresion of particular ranges of spatial frequency in the image. Generally, the defocus distance, Δf, is chosen so as to make the $\sin\gamma$ function around ± 1 at K values corresponding to

the spatial periodicities to be reproduced in the image and to cancel the phase shift arising from the spherical aberration in the given aperture configuration. In the present calculation, when the value of Δf is taken to be -1500 A with C_s = 1 mm, the $\sin\gamma$ function is nearly -1 in the range of K values covering almost the essential part of the first halo peak as Fig.32 shows. In this case, the calculated axial bright-field image contrast from the model assembly shows the (001) lattice image contrast in the centre part of the contour map, which is given in Fig.33. This is quite different from the appearance of the modulated and displaced {110} lattice fringe contrast in the case of Δf = -500 A, which is shown in Fig.29 and Fig.30. In order to obtain the optimum defocus distance in the actual observation, an example of which is shown in Fig.5(a), Hirotsu and Akada[33] carried out a one dimensional calculation of the image contrast from a b.c.c. microcrystal of 173 iron atoms embeded in some amorphous structure, taking account of the defocus distance, the beam divergence and the chromatic aberration. From one dimensional intensity distribution, they concluded that the best image will be obtained under the defocus values, -1500 A and -1660 A with C_s = 1.2 mm and λ = 0.0251 A. However, according to the consideration on the $\sin\gamma$-K relation, the real optimum defocus distance in this case is -1820 A. This means that for the observation of small ordered regions in the amorphous structure, the optimum condition for the lattice image contrast has a certain allowance because of the divergence of necessary K values enveloped by the first halo peak. In this respect, the selection of Δf = -1500 A with C_s = 1 mm seems to be satisfactory

enough to obtain the best lattice image contrast of the embryo.

The size of the b.c.c. embryo employed in the present model calculation agrees with that used to explain the diffraction data and the calculated lattice image shows a good agreement with the HREM observations. Since the appearance probability of the lattice image depends upon the size of the embryo, as Fig.35 shows, we may again employ the above embryo size, 10 A in diameter, to evaluate the amount of the medium range order clusters from their image appearance frequency. In Fig.39 is given a stereographic triangle of a (001) projection of a cubic crystal. When the beam incidence is along [001] of the b.c.c. embryo, the lattice image with four-fold symmetry appears as in Fig.33, and, when it is along [111], the six-fold image will appear. As discussed in the section 4.3, the (001) lattice image is retained up to $\theta \simeq 10°$ and 13° in the rotations of the aggregate around the [010] and [110] axes of the embryo respectively, as shown in the figure. The visibility of the {111} lattice image around the [111] pole would be more or less the same as above. Thus, the appearance ranges of the these images are enclosed with the dotted lines. Since the lines, [001]-[111] and [111]-[101], correspond to the {110} plane, the {110} fringe image always appears when the incident beam lies on these lines, as shown in Fig.36(b), except the regions around the above two poles, where the lattice image remains. The persistency of appearance of the {110} fringe image may occur also on the both sides of the two {110} lines and their boundary of visibility must be linked with those of the {001} and {111} lattice image. Therefore, the appearance range of the lattice and fringy images is given in the stereographic triangle as the shaded rim bands of the width of about 6°.

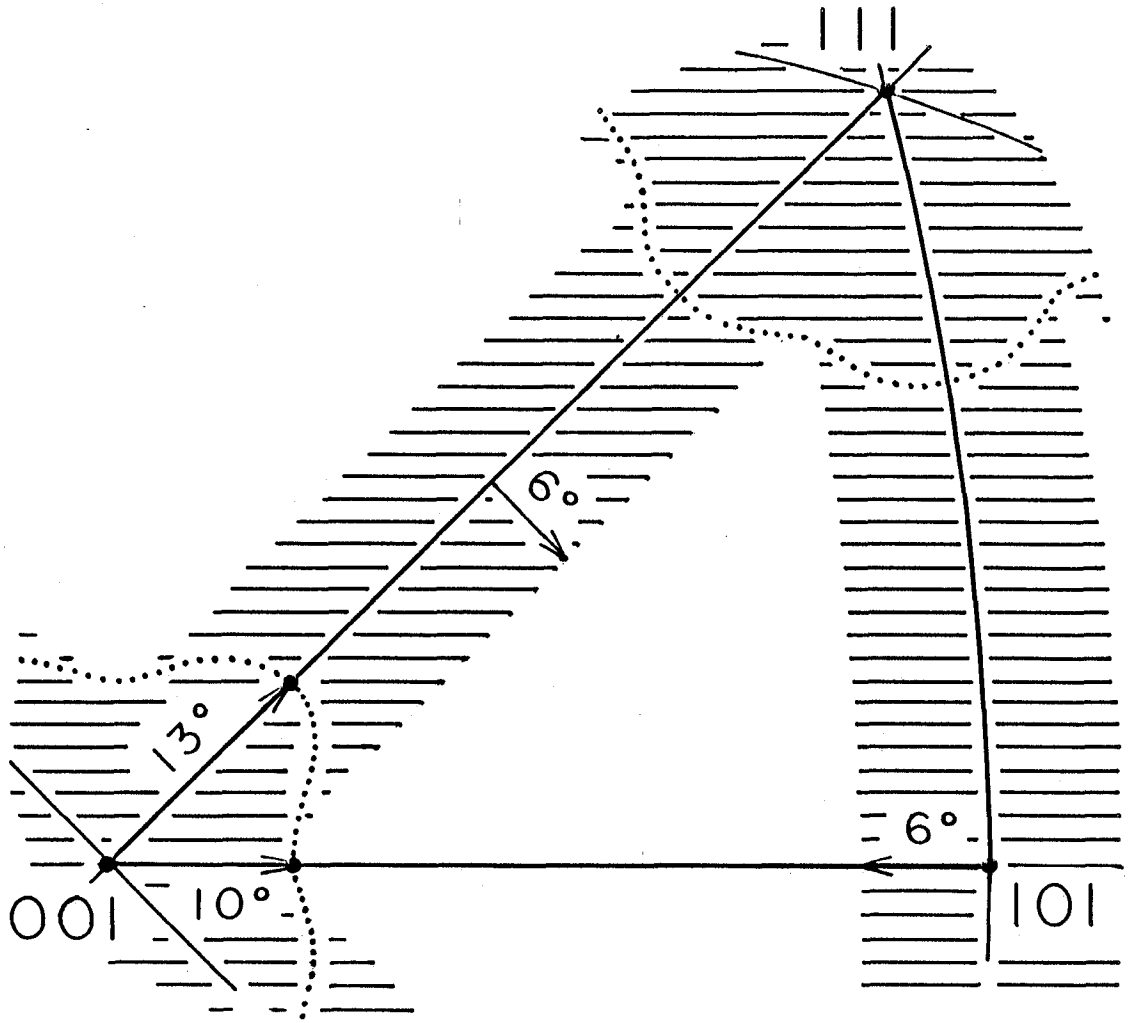

Fig. 39 A stereographic triangle of a (001) projection of a cubic crystal, where shaded rim bands correspond to the appearance range of the lattice images and lattice fringes, the former being enclosed with the dotted lines.

When the beam incidence is in the unshaded part of the triangle, no lattice and fringy images will be observed. From the area ratio of the shaded and unshaded, the probability to observe the ordered regions is estimated to be about 50 % provided that no texture exists in the distribution of the embryo axes. Another necessary consideration for the probability of observation is that the image contrasts from the ordered regions will be distorted and reduced by the overlapping effect and the thickness effect as mentioned before. In the present model calculations to explain the diffraction data and the high resolution electron microscope images, the mean distance between the centres of the embryos and the diameter of their images are about 16 A and 10 A respectively. Therefore, the image overlapping would take place to some extent in actual cases and the probability of observation would be reduced further.

The images from the ordered regions observed in the as quenched amorphous specimens usually have a little larger size than the calculated one from the embryo model and, at the same time, are distorted.[33] Wang et al.[107] showed by the x-ray diffraction that the α-iron particles in the $Fe_{83}B_{17}$ alloy after the crystallization under a pressure of 50 kbar contains boron as interstitial atoms, while Ray and Hasegawa[108] concluded from their experiments the predominant dissolution up to 12 at% of boron atoms on the substitutional sites of the b.c.c. lattice in the metastable α-iron. These results seem to suggest that boron atoms could occupy either interstitial sites or substitutional ones even in the embryos. Introduction of lattice defects such as a twin as well as metalloid atoms inevitably brings about the distortion of the b.c.c. lattice. It must be noted that the S(K) function of a microcrystallite becomes

more diffuse owing to the break down of the normal crystalline periodicity at the twin interface, as mentioned in the subsection 2.1.2. Accordingly, if lattice defects and/or boron atoms are introduced in the embryo cores, the lattice image contrast will be distorted. The image distortion would also arise from the overlap effect from the surrounding disordered atoms. As for the size of the lattice image a little larger than that by the model calculation, the actual size distribution of the ordered clusters, the size changes according to the differences in the cooling rate from the melt, and/or the diffusing out of the periodic image rising from the essential nature of diffraction must be taken into consideration and carefully examined.

The present calculation gives the basis of the interpretation and analysis of the high resolution electron microscope images of medium range order clusters in the amorphous materials. It seems to be necessary to calculate further on the lattice images from other kinds of embryos than the b.c.c. one, including the chemical medium range order clusters, and the effect of multiple scattering of electrons on the image formation. On the other hand, more HREM experiments, for instance, identification of the embryo lattice structure and observation of the variation of the lattice images by changing the quenching speed and by annealing at low temperature to induce structural relaxation or incipient crystallization,[109] seem to be required.

5.4 Conclusions

(1) Some newer experimental results strongly suggest that the chemical short range order or even farther range atomic order extending beyond the first neighbour distance may exist in the actual amorphous structure, which is hardly expected from the DRP models. By taking account of such atomic orderings, a simple and possible structural model of amorphous metals and alloys based on the concept of crystalline embryos is proposed.

(2) The model assembly of atoms containing the crystalline embryos and the disordered regions coexisting and continuously connected each other is constructed, and the G(r) and S(K) functions are calculated. Semiquantitative agreements between the calculation and experimental results are obtained. The atoms in the boundary regions break the crystalline periodicity, so that the combined intracrystalline and exocrystalline interference give the S(K) and G(r) functions essentially different from those of the microcrystalline model.

(3) As a more realistic model, the composite type assemblies for the amorphous Fe-B alloys containing the b.c.c. embryos and chemical clusters of Fe_3B type are constructed. In accordance with the arguments from experimental results, boron atoms are scattered so as not to contact with each other and embeded interstitially or substitutionally in the outer parts of the embryos and disordered regions, and a new process of the Fourier transformation, which takes account of the truncation effect, is employed. The obtained functions are in

excellent agreement with the experiments, when the embryo is taken to be as small as 10 A in diameter containing some twenty atoms in the core and the transition region of the cluster.

(4) The truncation in the Fourier transformation of the S(K) function severely controls the quality and spatial resolution of the G(r) function. Therefore, it is concluded that for more precise and satisfactory discussion on the structure of amorphous metals and alloys, the high K value measurements of the scattering intensity distribution are quite necessary.

(5) Recent high resolution electron microscopy (HREM) of amorphous alloys has revealed that the lattice like fringy and dotty contrasts of about 10 A in diameter frequently appear in the as quenched samples, strongly suggesting the medium range order in accordance with the author's prediction and diffraction calculation. The model calculation of the high resolution electron image contrast from the amorphous thin film is carried out by using the embryo model and the kinematical theory of electron diffraction. When the defocus distance is chosen as -1500 A and the spherical aberration constant as 1 mm, the lattice fringe and dot contrasts are well reproduced. Therefore, it is concluded that the medium range order of this size most probably exist in the actual amorphous structure. The consistency and the validity of the crystalline embryo model are concluded. A precise discussion on the selection of suitable defocus distances, especially concerning the amorphous structure, is also presented.

(6) The range of finding the lattice fringes and/or the lattice images is determined on the stereographic projection by the process

of rotation of the beam incidence, and the probability to observe the ordered regions in the actual amorphous thin films is estimated to be about 50 % provided that no texture exists in the distribution of the embryo axes. From the consideration on the effect of the film thickness and the image overlapping of the embryos, the ultimate frequency of appearance of the lattice fringes and dotty contrasts from the medium range order regions is evaluated too.

(7) At present, the images from the ordered regions observed in the as quenched amorphous specimens are different from experiment to experiment. It is suggested that the actual size distribution of the ordered clusters, the size changes according to the differences in the cooling rate from the melt, and/or the diffusing out of the periodic image rising from the essential nature of diffraction must be carefully examined.

(8) More HREM experiments, for instance, identification of the embryo lattice structure and observation of the variation of the lattice images by changing the quenching speed and by annealing at low temperature to induce structural relaxation or incipient crystallization, are proposed. At the same time, further calculations on the lattice images from other kinds of embryos than b.c.c. one, including the chemical medium range order clusters, and the effect of multiple scattering of electrons on the image formation are encouraged.

ACKNOWLEDGEMENTS

The author would like to express his gratitudes to Prof. F. E. Fujita of Osaka University for continuous guidance and encouragements throughout the course of this study. Hearty thanks are also due to Profs. R. Oshima and S. Nasu of Osaka University and Prof. M. Kiritani of Hokkaido University for their valuable discussions and comments, and to Dr. H. Yamanaka of Osaka Prefectural Industrial Research Institute for giving a chance to study at Osaka University.

A large part of the computer calculations was done by ACOS-700S and -S900 computer of the Crystallographic Research Center, Osaka University by their kind permission. The high resolution electron micrographs in the text are kindly offered by Dr. Y. Hirotsu of The Technological University of Nagaoka and Dr. H. Ichinose of Tokyo University. His thanks are also due to Miss. T. Ukawa, Messrs. K. Nunogaki, K. Niwase, I. Tanaka, K. Makino and T. Nakayasu for their helps in the calculations and in writing this thesis.

REFERENCES

1) P. Duwez, R. H. Williams and W. Klement: J. Appl. Phys. 31 (1960) 36.

2) J. D. Bernal: Nature 183 (1959) 141.
J. D. Bernal: Nature 185 (1960) 68.
J. D. Bernal and J. Mason: Nature 188 (1960) 910.

3) T. Hamada and F. E. Fujita: Jpn. J. Appl. Phys. 21 (1982) 981.
T. Hamada and F. E. Fujita: Proc. 4th Int'l Conf. Rapidly Quenched Metals, eds. T. Masumoto and K. Suzuki (Sendai: The Japan Institute of Metals) vol.I (1982) 319.
T. Hamada and F. E. Fujita: Jpn. J. Appl. Phys. 24 (1985) to be published.
T. Hamada and F. E. Fujita: Jpn. J. Appl. Phys. to be submitted.

4) G. S. Cargill III: Solid State Physics, eds. F. Seitz, D. Turnbull and H. Ehrenreich (New York: Academic Press, 1975) vol.30, 227.

5) P. H. Gaskell: J. Phys. C 12 (1979) 4337.

6) H. S. Chen: Rep. Prog. Phys. 43 (1980) 353.

7) T. Ichikawa: Phys. Stat. Sol. (a) 19 (1973) 707.

8) Y. Waseda and M. Ohtani: Phys. Stat. Sol. (b) 62 (1974) 535.

9) J. Dixmier and P. Duwez: J. Appl. Phys. 44 (1973) 1189.

10) K. Suzuki, T. Fukunaga, M. Misawa and T. Masumoto: Mater. Sci. Eng. 23 (1976) 215.
K. Suzuki, T. Fukunaga, M. Misawa and T. Masumoto: Sci. Rep. RITU A 26 (1976) 1.

11) T. Fukunaga, M. Misawa, K. Fukamichi, T. Masumoto and K. Suzuki: Proc. 3rd Int'l Conf. Rapidly Quenched Metals, ed. B. Cantor (London: The Metals Society) vol.II (1978) 325.

12) J. F. Sadoc and J. Dixmier: Mater. Sci. Eng. 23 (1976) 187.
J. F. Sadoc and J. Dixmier: The Structure of Non-Crystalline Materials, ed. P. H. Gaskell (London: Taylor & Fransis, 1977) 85.

13) Y. Waseda, T. Masumoto and S. Tamaki: Inst. Phys. Conf.. eds.

R. Evans and D. A. Greenwood (Bristol: The Institute of Physics, 1977) Ser.30, 268.

14) Y. Waseda, H. Okazaki and T. Masumoto: The Structure of Non-Crystalline Materials, ed. P. H. Gaskell (London: Taylor & Fransis, 1977) 95.

15) Y. Waseda: Proc. 3rd Int'l Conf. Rapidly Quenched Metals, ed. B. Cantor (London: The Metals Society) vol.II (1978) 352.

16) P. Lamperter, W. Sperl, E. Nold, G. Rainer-Harbach and S. Steeb: Proc. 4th Int'l Conf. Rapidly Quenched Metals, eds. T. Masumoto and K. Suzuki (Sendai: The Japan Institute of Metals) vol.I (1982) 343.

17) G. S. Cargill III: J. Appl. Phys. 41 (1970) 12.

18) G. S. Cargill III and R. W. Cochrane: J. de. Physique 35 (1974) C4-269.

19) J. Logan: Phys. Stat. Sol. (a) 32 (1975) 361.

20) N. Hayashi, T. Fukunaga, M. Ueno and K. Suzuki: Proc. 4th Int'l Conf. Rapidly Quenched Metals, eds. T. Masumoto and K. Suzuki (Sendai: The Japan Institute of Metals) vol.I (1982) 355.

21) Y. Waseda and H. S. Chen: Phys. Stat. Sol. (a) 49 (1978) 387.

22) N. Cowlam, M. Sakata and H. A. Davies: J. Phys. F 9 (1979) L203.

23) K. Dini, N. Cowlam and H. A. Davies: J. Phys. F 12 (1982) 1553.

24) C. C. Tsuei, G. Longworth and S. C. H. Lin: Phys. Rev. 170 (1968) 603.
C. C. Tsuei and H. Lilienthal: Phys. Rev. B 13 (1976) 489.

25) F. E. Fujita, T. Masumoto, M. Kitaguchi and M. Ura: Jpn. J. Appl. Phys. 16 (1977) 1731.
F. E. Fujita: J. de Physique, Colloq. C2 Suppl. N°2 40 (1979) C2-120.

26) R. Oshima and F. E. Fujita: J. de Physique, Colloq. C2 Suppl. N°2 40 (1979) C2-132.
R. Oshima and F. E. Fujita: Jpn. J. Appl. Phys. 20 (1981) 1.

27) I. Vincze, D. S. Boudreaux and M. Tagze: Phys. Rev. B 19 (1979) 4896.
T. Kemény, I. Vincze, B. Fogarassy and S. Arajs: Phys. Rev. B 20 (1979) 476.
I. Vincze and F. van der Woude: J. Non-Cryst. Solids 42 (1980) 499.

28) M. Koshimura, Y. Abe, M. Takahashi, S. Inawashiro and S. Katsura: Proc. 4th Int'l Conf. Rapidly Quenched Metals, eds. T. Masumoto and K. Suzuki (Sendai: The Japan Institute of Metals) vol.II (1982) 1113.

29) M. L. Rudee and A. Howie: Phil. Mag. 25 (1972) 1001.

30) S. R. Herd and P. Chaudhari: Phys. Stat. Sol. (a) 26 (1974) 627.

31) Y. Ishida, H. Ichinose, H. Shimada and H. Kojima: Proc. 4th Int'l Conf. Rapidly Quenched Metals, eds. T. Masumoto and K. Suzuki (Sendai: The Japan Institute of Metals) vol.I (1982) 421.

32) H. Ichinose and Y. Ishida: Trans. JIM 24 (1983) 405.

33) Y. Hirotsu and R. Akada: Jpn. J. Appl. Phys. 23 (1984) L479.
Y. Hirotsu and R. Akada: Abstract of annual meeting of Japan Institute of Metals (1984) 495.

34) M. Takahashi and M. Koshimura: Proc. 4th Int'l Conf. Rapidly Quenched Metals, eds. T. Masumoto and K. Suzuki (Sendai: The Japan Institute of Metals) vol.II (1982) 1061.

35) K. Fukamichi, M. kikuchi, S. Arakawa and T. Masumoto: Solid St. Commun. 23 (1977) 955.
H. Hiroyoshi, K. Fukamichi, M. Kikuchi, A. Hoshi and T. Masumoto: Phys. Lett. 65A (1978) 163.

36) R. Hasegawa and R. Ray: J. Appl. Phys. 49 (1978) 4174.

37) F. E. Luborsky, H. H. Liebermann, J. J. Becker and J. L. Walter: Proc. 3rd Int'l Conf. Rapidly Quenched Metals, ed. B. Cantor (London: The Metals Society) vol.II (1978) 188.

38) P. Panissod, D. Aliaga Guerra, A. Amamou, J. Durand, W. L. Johnson, W. L. Carter and S. J. Poon: Phys. Rev. Lett. 44 (1980) 1465.

T. Mizoguchi, J. I. Budnick, P. Panissod, J. Durand and H. J. GÜntherodt: Proc. 4th Int'l Conf. Rapidly Quenched Metals, eds. T. Masumoto and K. Suzuki (Sendai: The Japan Institute of Metals) vol.II (1982) 1149.

39) T. M. Hayes, J. W. Allen, J. Tauc, B. C. Giessen and J. J. Hauser: Phys. Rev. Lett. 40 (1978) 1282.

40) J. L. Finney: Nature 266 (1977) 309.

41) Y. Waseda: J. Solid St. Phys. 12 (1977) 181.

42) P. Chaudhari and D. Turnbull: Science 199 (1978) 11.

43) J. L. Finney: Proc. Roy. Soc. London A319 (1970) 479, 495.

44) G. D. Scott and D. M. Kilgour: J. Phys. D 2 (1969) 863.

45) C. H. Bennett: J. Appl. Phys. 43 (1972) 2727.

46) D. J. Adams and A. J. Matherson: J. Chem. Phys. 56 (1972) 1989.

47) J. F. Sadoc, J. Dixmier and A. Guinier: J. Non-Cryst. Solids 12 (1973) 46.

48) T. Ichikawa: Phys. Stat. Sol. (a) 29 (1975) 293.

49) J. A. Baker, M. R. Hoare and J. L. Finney: Nature 257 (1975) 120.

50) L. von Heimendahl: J. Phys. F 5 (1975) L141.

51) G. A. N. Connell: Solid St. Commun. 16 (1975) 109.

52) R. Yamamoto, H. Matsuoka and M. Doyama: Phys. Lett. A64 (1978) 457.

53) K. Maeda and S. Takeuchi: J. Phys. F 8 (1978) L283.

54) Y. Hiwatari, H. Matsuda, T. Ogawa, N. Ogita and A. Ueda: Prog. Theor. Phys. 52 (1974) 1105.

55) A. Rahman, M. J. Mandell and J. P. Mctague: J. Chem. Phys. 64 (1976) 1564.

56) W. D. Kristensen: J. Non-Cryst. Solids 21 (1976) 303.

57) L. V. Woodcock, C. A. Angell and P. Cheeseman: J. Chem. Phys. 65 (1976) 1565.

58) M. Tanemura, Y. Hiwatari, H. Matsuda, T. Ogawa, N. Ogita and

A. Ueda: Prog. Theor. Phys. 58 (1977) 1079.

59) J. D. Bernal: Proc. Roy. Soc. London A280 (1964) 299.

60) E. J. W. Whittaker: J. Non-Cryst. Solids 28 (1978) 293.

61) R. Yamamoto and M. Doyama: J. Phys. F 9 (1979) 617.

62) G. S. Cargill III: J. Appl. Phys. 41 (1970) 2249.

63) D. E. Polk: Scr. Met. 4 (1970) 117.
D. E. Polk: Acta Met. 20 (1972) 485.

64) D. S. Boudreaux and J. M. Gregor: J. Appl. Phys. 48 (1977) 152, 5057.

65) D. S. Boudreaux: Phys. Rev. B 18 (1978) 4039.

66) T. Fujiwara, H. S. Chen and Y. Waseda: J. Phys. F 11 (1981) 1327.

67) T. Fujiwara and Y. Ishii: J. Phys. F 10 (1980) 1901.

68) K. Suzuki: Proc. Sympo. Amoph. Met., Suppl. Sci. Rep. RITU A (1978) 1.

69) D. S. Boudreaux and H. J. Frost: Phys. Rev. B 23 (1981) 1506.

70) J. F. Graczyk and P. Chaudhari: Phys. Stat. Sol. (b) 75 (1976) 593.

71) P. L. Maitrepierre: J. Appl. Phys. 40 (1963) 4826.

72) P. H. Gaskell: Proc. 3rd Int'l Conf. Rapidly Quenched Metals, ed. B. Cantor (London: The Metals Society) vol.II (1978) 277.
P. H. Gaskell: J. Non-Cryst. Solids 32 (1979) 207.

73) S. Kobayashi, K. Maeda and S. Takeuchi: Jpn. J. Appl. Phys. 19 (1980) 1033.

74) S. Aur, T. Egami and I. Vincze: Proc. 4th Int'l Conf. Rapidly Quenched Metals, eds. T. Masumoto and K. Suzuki (Sendai: The Japan Institute of Metals) vol.I (1982) 351.

75) L. H. Germer and A. H. White: Phys. Rev. 60 (1941) 447.

76) J. Dixmier, K. Doi and A. Guinier: Physics of Non-Crystalline Solids, ed. J. A. Prins (Amsterdam: North-Holland Publ., 1965) 67.

77) C. N. J. Wagner, T. B. Light, N. C. Halder and W. E. Lukens: J. Appl. Phys. 39 (1968) 3690.

78) F. Betts and A. Bienenstock: J. Appl. Phys. 43 (1972) 4591.

79) F. L. Galeener and M. M. Rodoni: Amorphous and Liquid Semiconductors, eds. J. Stuke and W. Brenig (London: Taylor & Francis, 1974) 101.

80) A. Howie, O. L. Krivanek and M. L. Rudee: Phil. Mag. 27 (1973) 235.

81) W. Cochran: Phys. Rev. B 8 (1973) 623.

82) O. L. Krivanek and A. Howie: J. Appl. Cryst. 8 (1975) 213.

83) E. J. Jensen, W. D. Kristensen and R. M. J. Cotterill: Phil. Mag. 27 (1973) 623.
W. D. Kristensen, E. H. Jensen and R. M. J. Cotterill: Phil. Mag. 30 (1974) 229, 245.

84) H. Suzuki: Proc. 4th Int'l Conf. Rapidly Quenched Metals, eds. T. Masumoto and K. Suzuki (Sendai: The Japan Institute of Metals) vol.I (1982) 225.

85) T. Ninomiya: The Structure of Non-Crystalline Materials, ed. P. H. Gaskell (London: Taylor & Francis, 1977) 45.

86) H. Koizumi and T. Ninomiya: J. Phys. Soc. Jpn. 49 (1980) 1022.

87) J. Frenkel: Kinetic Theory of Liquids (New York: Dover, 1946) 96, 303.

88) F. E. Fujita: Proc. Sympo. Amorph. ,et., Suppl. Sci. Rep. RITU A 28 (1980) 1.
F. E. Fujita: Proc. 4th Int'l Conf. Rapidly Quenched Metals, eds. T. Masumoto and K. Suzuki (Sendai: The Japan Institute of Metals) vol.I (1982) 301.

89) F. E. Fujita: Proc. 5th Int'l Conf. Rapidly Quenched Metals (Würzburg, 1984) in press.

90) M. Takagi: J. Phys. Soc. Jpn. 11 (1956) 396.

91) Y. Waseda, F. Takahashi and K. Suzuki: Sci. Rep. RITU A 23 (1972) 127.

92) T. Hamada, K. Yamakawa and F. E. Fujita: J. Phys. F 11 (1981) 657.

93) G. W. Stewart: Phys. Rev. 35 (1930) 726.
G. W. Stewart: Phys. Rev. 37 (1931) 9.

94) E. Nold, G. Rainer-Harbach, P. Lamperter and S. Steeb: Z. Naturforsch. 38a (1983) 325.

95) C. S. Hsu and A. Rahman: J. Chem. Phys. 70 (1979) 5234.

96) Y. Fukano: Jpn. J. Appl. Phys. 13 (1974) 1001.

97) H. M. Pak and M. Doyama: J. Fac. Eng. Univ. Tokyo B 30 (1969) 111.

98) H. B. Huntington: Solid State Physics, eds. F. Seitz and D. Turnbull (New York: Academic Press, 1958) vol.7, 274.

99) M. Kiritani and T. Hamada: Proc. 4th Int'l Conf. Rapidly Quenched Metals, eds. T. Masumoto and K. Suzuki (Sendai: The Japan Institute of Metals) vol.I (1982) 583.

100) F. Zernike and J. A. Prins: Z. Phys. 41 (1927) 184.

101) A. Howie: J. Non-Cryst. Solids 31 (1978) 41.

102) K. J. Hanssen: Adv. in Optical and Electron Micr., eds. Cosslett and Barer, 4 (1974) 1.

103) M. F. Ashby, F. Spaepen and S. Williams: Acta Met. 26 (1978) 1647.

104) K. Doi: J. Appl. Cryst. 9 (1976) 382.

105) M. R. Bennett and J. G. Wright: Phys. Stat. Sol. (a) 13 (1972) 135.

106) N. Yoshida and F. E. Fujita: J. Phys. F 2 (1972) 1009.

107) W.-K. Wang, H. Iwasaki and K. Fukamichi: J. Mater. Sci. 15 (1980) 2701.

108) R. Ray and R. Hasegawa: Solid St. Commun. 27 (1978) 471.

109) Y. Katao, M. Kiritani and F. E. Fujita: J. Mater. Sci. 19 (1984) 3375.